Methods for Evaluating the Performance and Human Stress-Factors of Percussive Riveting

Jonathan Y. Ahn

A thesis submitted
in partial fulfillment of the
requirements for the degree of

Master of Science in Engineering

University of Washington

2017

Committee:

Per Reinhall

Joseph Garbini

Riley HansonSmith

Program Authorized to Offer Degree:
Mechanical Engineering

ProQuest Number: 10599021

ProQuest 10599021

University of Washington

Abstract

Methods for Evaluating the Performance
and Human Stress-Factors of Percussive Riveting

Jonathan Y. Ahn

The aerospace industry automates portions of their manufacturing and assembly processes. However, mechanics still remain vital to production, especially in areas where automated machines cannot fit, or have yet to match the quality of human craftsmanship. One such task is percussive riveting. Because percussive riveting is associated with a high risk of injury, these tool must be certified prior to release. The major contribution of this thesis is to develop a test bench capable of percussive riveting for ergonomic evaluation purposes. The major issues investigated are: (i) automate the tool evaluation method to be repeatable; (ii) demonstrate use of displacement and force sensors; and (iii) correlate performance and risk exposure of percussive tools. A test bench equipped with servomotors and pneumatic cylinders to control xyz-position of a rivet gun and bucking bar simultaneously, is used to explore this evaluation approach.

TABLE OF CONTENTS

LIST OF FIGURES

vi

LIST OF TABLES

ACKNOWLEDGMENTS

DEDICATION

I dedicate this work to my parents, Hyesook and Jee Ahn, my brother, Jacob, and fiance, Leah, for their steadfast support of my academic goals, and pursuit of a second career. It is with great privilege that I present this work to them.

Chapter 1

INTRODUCTION

This thesis documents the development of an automated test bench for evaluating hand-held percussive tools used in commercial aircraft manufacturing. While the aerospace industry has successfully automated many of the high-injury related tasks, the industry still relies on mechanics (humans) to complete assembly stages where these large machines are unable to fit, or where the quality of work has yet to match a mechanic [10]. These stages include but are not limited to, installing fuselage panels to the barrel structure, joining fuselage segments, and lap joints. One such task is percussive riveting, which is still performed by mechanics. Unfortunately, percussive riveting is known to cause vibration-related injuries [4]. To minimize the risk of injury to mechanics, percussive tools are tested and certified prior to release.

1.1 Percussive Riveting

Percussive riveting is a permanent fastener installation process, requiring two distinct tools: a pneumatic hammer and bucking bar. The fastener, known as a rivet, is made of a malleable metal alloy designed to deform under heavy repeated strikes. This process also causes the rivet to work harden in its finished state. The pneumatic hammer (commonly referred to as a rivet gun) is set at the head of the rivet, while the bucking bar is held at the tail end, which forms the button. This deformation process also causes the rivet to expand within the hole, creating a seal, which improves the mechanical loading properties [18]. Fig. 1.1 illustrates the orientation of the tools with respect to the rivet and the structure that is to be fastened together.
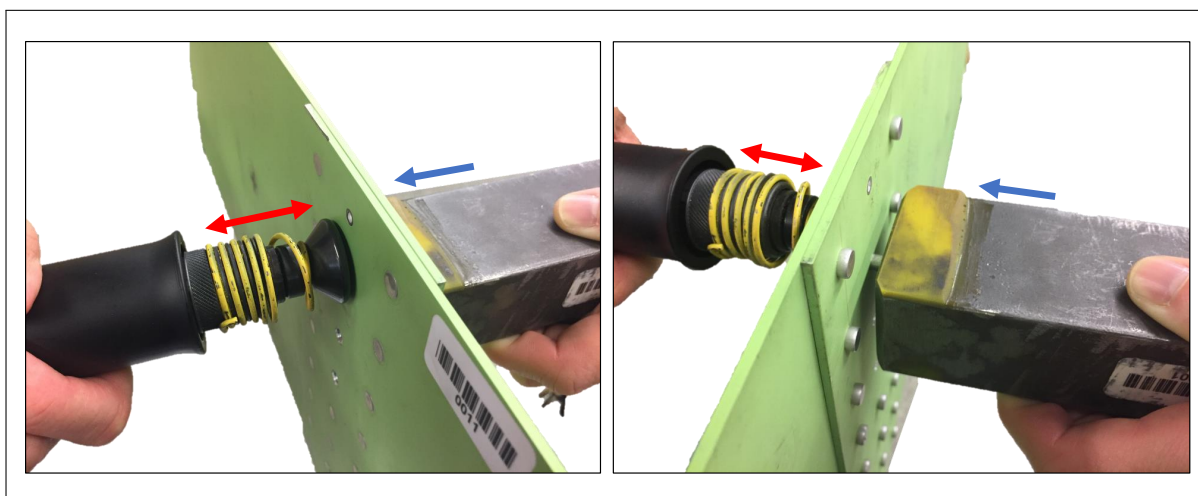
Figure 1.1: Depicts the pneumatic hammer operator, commonly referred to as a riveter (left) applying force to the rivet and coupon. The bucking bar operator, also known as a bucker (right) provides the hardstop in which the rivet tail forms a button.

1.2   Risk Discrepancy

To minimize the risk of injury, the International Standard Organization ISO 5349-1, pertaining to mechanical vibration and shock, provides guidelines to predict the adverse effects of vibrations. This standard defines the most dangerous frequencies to be $\leq 16\ Hz$, and least likely to cause injury when $\geq 100\ Hz$. Total vibration exposure is determined by Eq. 1.1, which is based on time and acceleration values. However, epidemiological and animal model experiments indicate frequencies $\geq 100\ Hz$ also induce injuries, noting this regulation may be under representing the risks [17]. For instance, chainsaw operators represent the third largest population affected by hand-transmitted vibration injuries, but are primarily exposed to $100 - 1,000\ Hz$ [13], [20].

$$A(8) = \sqrt{\frac{1}{T_0} \sum_{i=1}^{n} a_{hvi}^2 \times T_i}$$

$$where \begin{cases} T_0 = 28,800 \ s \ representing \ 8 \ hr \ shift \\ \\ T_i = total \ daily \ exposure \ in \ seconds \\ \\ n = number \ of \ vibration \ events \\ \\ a_{hvi} = vibration \ total \ based \ on \ acceleration \end{cases} \tag{1.1}$$

1.3 Defined Injuries

While defining the safe frequency boundary requires further investigation, the injuries associated with vibrations are more apparent, and include but are not limited to carpal tunnel and, lower-back, shoulder, and neck pains. However, the most notable injury is Vibration White Finger (VWF) syndrome, which also is referred to as Hand-Arm Vibration (HAV) syndrome and Raynaud's syndrome. As the name implies, the most visible indication of VWF is the permanent whitening, or blanching, of the fingertips. This is cause by the narrowing of the arteries in the hand and fingers, reducing blood flow, which leads to neuropathy and loss of dexterity [16].

The effects of vibration, at given accelerations, are detectable on both a human kinematic and cellular level. Vibration frequencies entering the hand are capable of reaching the head when $\leq 40 \ Hz$, at $\leq 100 \ Hz$ the vibrations are isolated to the hand and forearm, and $\geq 250 \ Hz$ are found to be limited to the hand and wrist [6]. Long-term exposure to vibrations are known to disrupt cell distribution and cause breakdown of the endothelial cells of the arterial lumen.

A study conducted on live animal models indicated vessel damage and/or deformation occurred at $30 \ Hz$, $60 \ Hz$, $120 \ Hz$, and $800 \ Hz$ at a constant acceleration of $49 \ m/s^2$ [5], [17]. The disturbance was found to cause an influx of platelets to repair the distressed vessel, the repair however decreases blood flow. These findings contradict the specified frequency ranges

stated in ISO 5349.

1.4   Evaluation Method

A common method to evaluate vibration is to fire the percussive tool, in this case a pneumatic hammer, against a rigid metal plate and to record the frequency and magnitude at the handle with an accelerometer. To evaluate bucking bars, a pneumatic hammer is fixed in place and fired against a non-deforming (rigid) material, which strikes the bucking bar from the opposing side. While these methods determine the general range of acceleration and vibration frequencies, the National Institute for Occupation Safety and Health (NIOSH) found discrepancies between lab measured data and actual levels [14].

The NIOSH determined the acceleration levels measured from the field were up to 25% higher than lab results. This was due to the use of simulated materials and test fixtures not reflective of the mechanic or task [14]. Additionally, the results of these methods favor tools with lower force outputs, potentially leading to further injuries due to a mechanic overcompensating for a weaker tool - not capable of accomplishing the task. In turn, these methods do not provide information on work performance, which is defined as the capability of the tool to complete a given task.

1.5   Thesis Proposal

This thesis proposes the development of an automated test bench to correlate work performance, to the risk-of-injury exposure on mechanics also referred to as human stress-factors. This includes the forces, displacement, and duration a mechanic is exposed to while installing fasteners. This is an expansion on the previously described evaluation method while addressing two needs: determining the capability of a tool to complete the installation task, and a test bench model representative of a mechanic.

Redefining the frequencies associated with injuries extends beyond the scope of this thesis. In this thesis, risk of injury is correlated with the reaction force a percussive tool produces, and amount of time required by the tool to complete a task. Likewise, a higher force mag-

nitude and longer duration indicates more stress is placed on a mechanic, which leads to fatigue and poses the risk of injury. Hand-held tools that generate a higher magnitude of force cause the mechanic to increase grip strength, increasing the transmission of forces and vibration [9].

The immediate solution to determine tool performance may be to conduct the evaluation directly on mechanics in the field. However human involvement makes it difficult to standardize and compare results. If a mechanic is not familiar with a new tool, the tool may not receive a fair evaluation and be noted as performing poorly. Likewise, if a mechanic is exceptionally experienced then the flaws in a sub-par tool may go unnoticed. The use of an automated system designed to conduct percussive tests in a similar fashion as a mechanic, while using actual fasteners and coupons in the field, can provide repeatibility and standardization.

There are three objectives to this thesis, each with design specializations for the proposed solution.

1. Develop an automated test bench capable of riveting

   - Control over *(xz-plane)* to repeatedly align percussive tool within $\pm 0.25\ mm$.
   - Apply constant force values between $0 - 530\ N$ to clamp tools to coupon.
   - Trigger push/pull response time is $< 0.04\ s$ to maintain number of percussive strikes within ± 1, based on a $\leq 25\ Hz$ firing pneumatic hammer.
   - Accept standard test coupons manufactured in the field with dimensions of 6" $\times$ 15" $\times$ 0.7" (*specified in English Units*)

2. Demonstrate value of expanding data collection parameters.

   - Track change in tool position *(y-plane)* with respect to time.
   - Profile the peak magnitudes generated by the percussion within 1.0% error
   - Monitor pressure levels to confirm each test is properly executed.

3. Correlate work performance to human stress-factors.

- Devise a dynamic system model that represents a human arm applying constant force.

- Sensor data formatted for numerical analysis tool.

- Create program capable of objectively evaluating test data for exposure duration, peak heights, and frequencies.

Chapter 2

EVALUATION APPROACH

The test bench is operated using National Institute LabVIEW$^{\text{TM}}$, which controls the motor position and valve manifold settings over EtherNet/IP$^{\text{TM}}$. The data-acquisition sensors are also interfaced with this system through multi-channel I/O modules calibrated using NI-DAQmx. The test bench is supported on a steel frame with dimensions 1.83 m × 1.57 m × 1.40 m on vibration-damping leveling mounts. Fig. 2.1 displays the structure of the test bench.

2.1   Coordinate Positioning

Two pairs of MOOG Animatics$^{\text{TM}}$ servo motors are used to navigate both ends of the *(xz-plane)* of the coupon window. For the *y-axes*, in place of servo position control, air cylinders with piston diameters of 64 mm and stroke length of 170 mm are used to actuate (clamp) the tool forward with a desired force, and retract when moving the tool to another location. These air cylinders are used to clamp the tool platform against the test coupon. The location of the three actuators on each side of the coupon are mirrored, and operate on the same Cartesian coordinates with the exception of the air cylinders recognizing positive *y-axes* being towards the center for both. Fig. 2.2 illustrates the references with respect to the proposed test bench.

2.2   Pneumatic Control

The air cylinders to clamp the tools to each side of the coupon; one for the pneumatic hammer, and the other for the bucking bar, are shown in Fig. 2.3 and 2.4. A second air cylinder with a diameter of 6.4 mm, is attached to the pneumatic hammer to push

the trigger, as shown in Fig. 2.6. This air cylinder applies 25 N and is capable of pushing/retracting the pneumatic hammer trigger in $< 0.03\ s$. These air cylinders are controlled by a FESTO$^{\text{TM}}$ valve manifold, as shown in Fig. 2.5. The desired pressure and duration is programmed in LabVIEW, which controls the valve manifold.
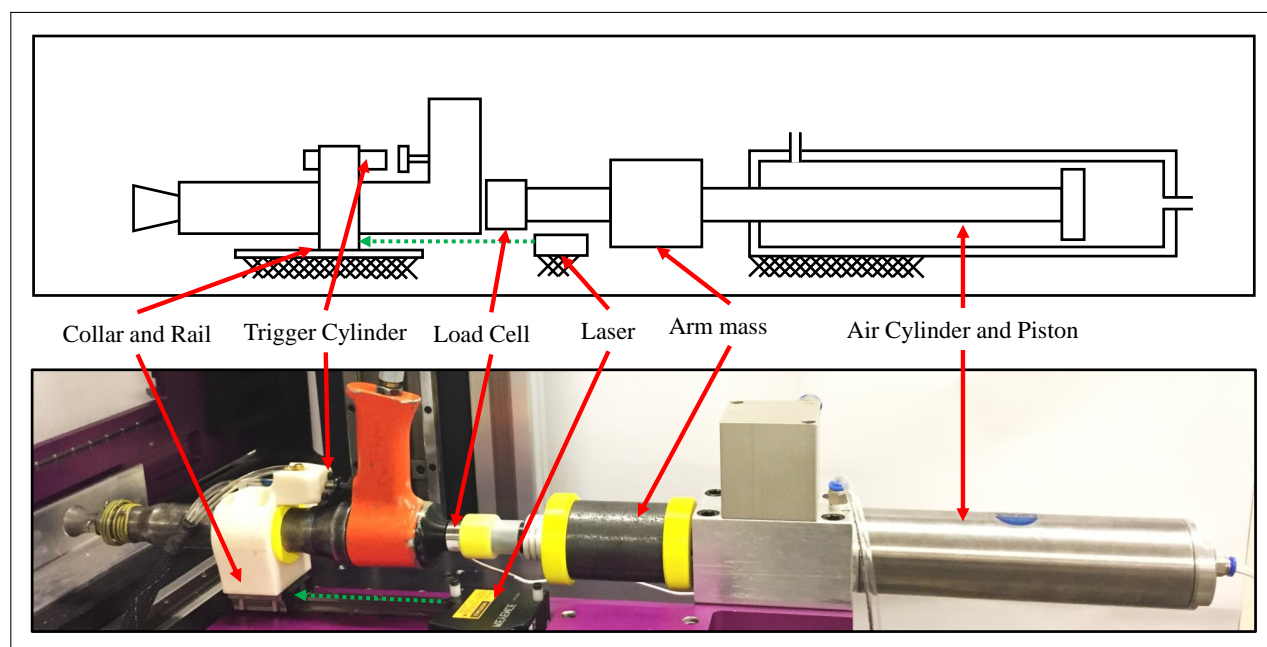
Figure 2.3: Depicts the final carriage design for the pneumatic hammer that is installed to the right-hand side of the *(xz-plane)* platform. The load cell is fastened between the arm mass and the back of the pneumatic hammer. The laser is aligned to the linear rail block (green) and captures the displacement as the hammer moves forward and backwards. The arm mass is further described in Ch.4.
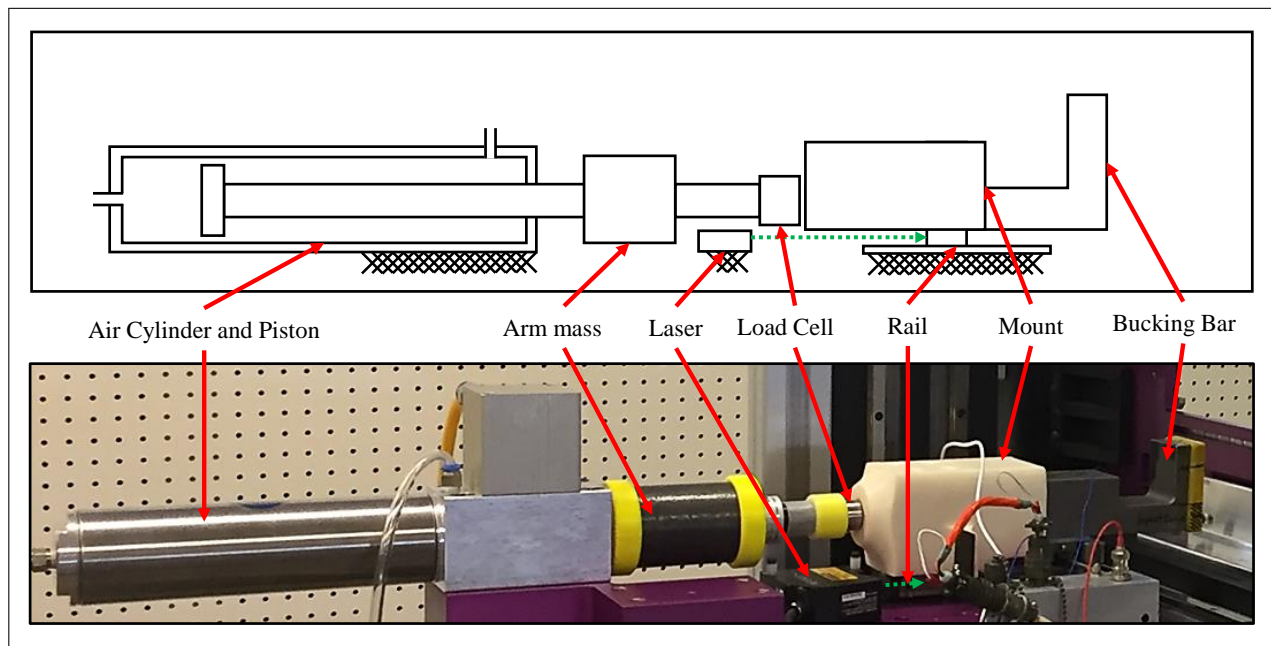
Figure 2.4: Depicts the final carriage design for the bucking bar that is installed to the left-hand side of the *(xz-plane)* platform. The load cell is fastened between the arm mass and the back of the bucking bar. The laser is aligned to the linear rail block (green) and captures the displacement as the bucking bar moves forward and backwards. The arm mass is further described in Ch.4.

2.3   Design Versatility

The mount securing the percussive tool is 3D-printed with 100% infill using high density acrylonitrile butadiene styrene (ABS) plastic. This provides a solution to testing percussive tools of various shapes and dimensions, with relatively short turn around times. These ABS parts mount the tools to THK$^{\text{TM}}$ SHS15 pillow blocks, which slide along the linear rails. Fig. 2.6 shows the printed part used to maintain alignment of the percussive tools.

2.4 Data-Acquisition (DAQ)

The test bench is equipped with four types of data-acquisition sensors to record and validate the performance of the tools. The minimum sampling rate is set to be $22\times$ that of the peak wavelength frequency each sensor encounters, to obtain peak heights with 1.0% error.

2.4.1 Laser Displacement

Keyence^{TM} Head-spot type LK-G152 lasers are installed to track along the y-axis. These lasers record the forward progress of the tool as it installs the fasteners, and the reverse displacement (recoil) generated by each strike. The minimum sampling rate required is $0.8\ kHz$ for a percussive tool firing up to $25\ Hz$, the actual sampling rate used in this thesis is $5.0\ kHz$.

2.4.2 Acoustic Profile

The G.R.A.S.^{TM} 26CB preamplifier microphone is installed near the rivet dye at a distance of $\approx 0.07\ m$, and is oriented towards the fastener. The purpose of this sensor is to record the peak sound pressure produced by each percussive impact. In low-noise environments, these peak signals are used to confirm the number of hits. The signal peaks within the first $\approx 10\%$ of each strike, demanding a faster minimum sampling rate, of $22.0\ kHz$. The actual rate used is $25.0\ kHz$.

2.4.3 Force Sensors

Interface^{TM} WMC Button load cells are placed in series behind the pneumatic hammer and bucking bar, recording the axial compression forces exerted on the back of the handle. The proposed test bench is configured with the load cell between the tool and the arm mass. The pneumatic hammer transfers a large force over a short duration, in which the signal peaks within the first $\approx 20\%$ of the wave in each impact. The force profile is a critical component,

correlating both the performance and stress-factors to the other sensors. The minimum rate is 1.6 kHz and the actual rate is set to 10.0 kHz.

2.4.4   Air Pressure Monitor

A FlowMaxx^{TM} Venturi Flowmeter is installed in series with the air supply energizing the pneumatic hammer, monitoring the static and differential pressures. This sensor is used to determine the pneumatic hammer is firing properly based on the expected air consumption rate. This value is expected to remain constant with respect to each pneumatic hammer. Unusual results may be traceable back to the pressure changes to determine whether a tool is malfunctioning, and in turn not representative of all equivalent models. The minimum rate is 1.6 kHz and the actual rate collected is 10.0 kHz.

Figure 2.1: Displays the black steel box tube frame with large footprint used to support the test bench, showing mainly the right-hand side. The valve manifold is located beneath the (purple) coupon holder, and two pressure filtration-lubrication regulators are attached to the far lower side of the steel frame.
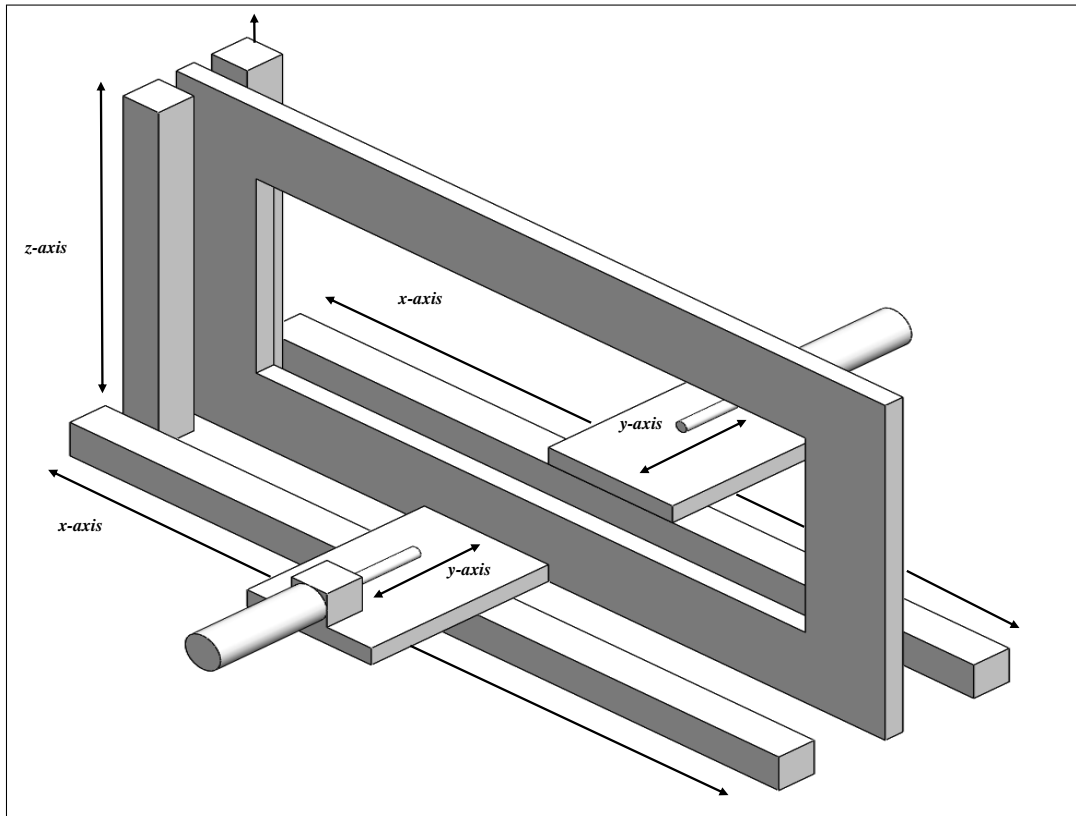
Figure 2.2: Depicts the *xyz*-coordinate range of the test bench. The working envelope of the servomotors *(xz-plane)* is approximately $0.60\ m$ width by $.45\ m$ height, and the inward stroke length for y-axis pneumatic air cylinders are $0.17\ m$. The test bench is fixed at a standing height of $1.52\ m$ to also allow for comparison studies with mechanics. The servomotors can be jogged to either end of the test bench to provide space for mechanics to rivet on the test bench.

Figure 2.5: Displays the Festo valve manifold utilized to control the pressure outputs to the pneumatic components.
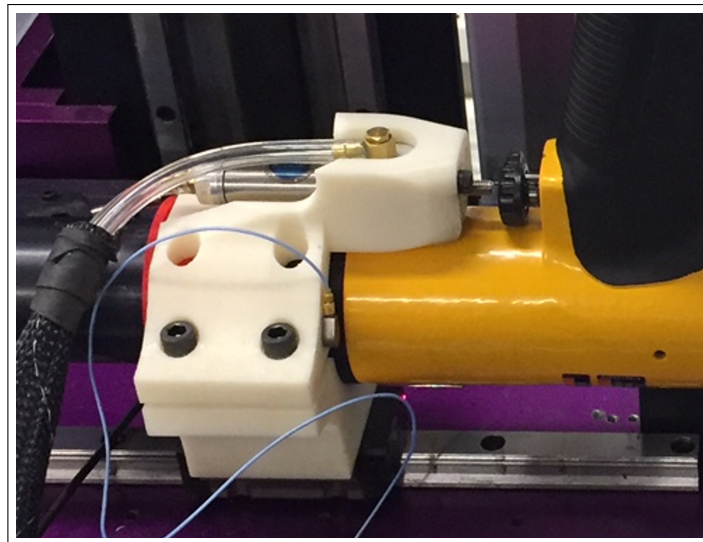
Figure 2.6: Displays the white ABS printed mount, which houses the trigger air cylinder and secures the percussive tool to the linear rail.

Chapter 3

PERCUSSIVE INDEX

This thesis explores the use of a percussive index, borrowed from the Articulated Total Body (ATB) and Head Injury Criterion (HIC) [8], [12]. While head injuries differ from upper extremity injuries, this is to propose that other previously established indices be investigated and considered for use to grade percussive tools. Additionally, developing an entirely new index would require subjecting a significant number of animals to various arm injuries, when instead head injuries have already been, and continue to be extensively studied using in vivo models [21], [22]. The percussive index equation is equivalent to the Head Injury Criterion (HIC) equation [15] (not to be mistaken for the Head Severity Index equation).

The original HIC equation uses acceleration, a, within the integral. For the applications of this thesis, acceleration is derived from the force over total mass, as shown in Eq. 3.1.

$$
Percussive\ Index\ (PI) = \tau_c \left[\frac{1}{\tau_c} \int_t^{t+\tau_c} \frac{F_R}{m_T}\ dt \right]^{2.5}
$$

$$
where \begin{cases} \tau_c = Time\ Constant \\[2mm] t = Start\ Time\ (s) \\[2mm] F_R = Reaction\ Force\ (N) \\[2mm] m_T = Mass\ of\ Tool\ \&\ Arm\ Model\ (kg) \end{cases} \tag{3.1}
$$

In Eq. 3.1, τ_c is defined as the width of the time window, which span the limits of the integral. The τ_c is moved forward along the time-axis in increments equal to $\frac{\tau_c}{10}$, while returning the index value as shown in Fig. 3.1.
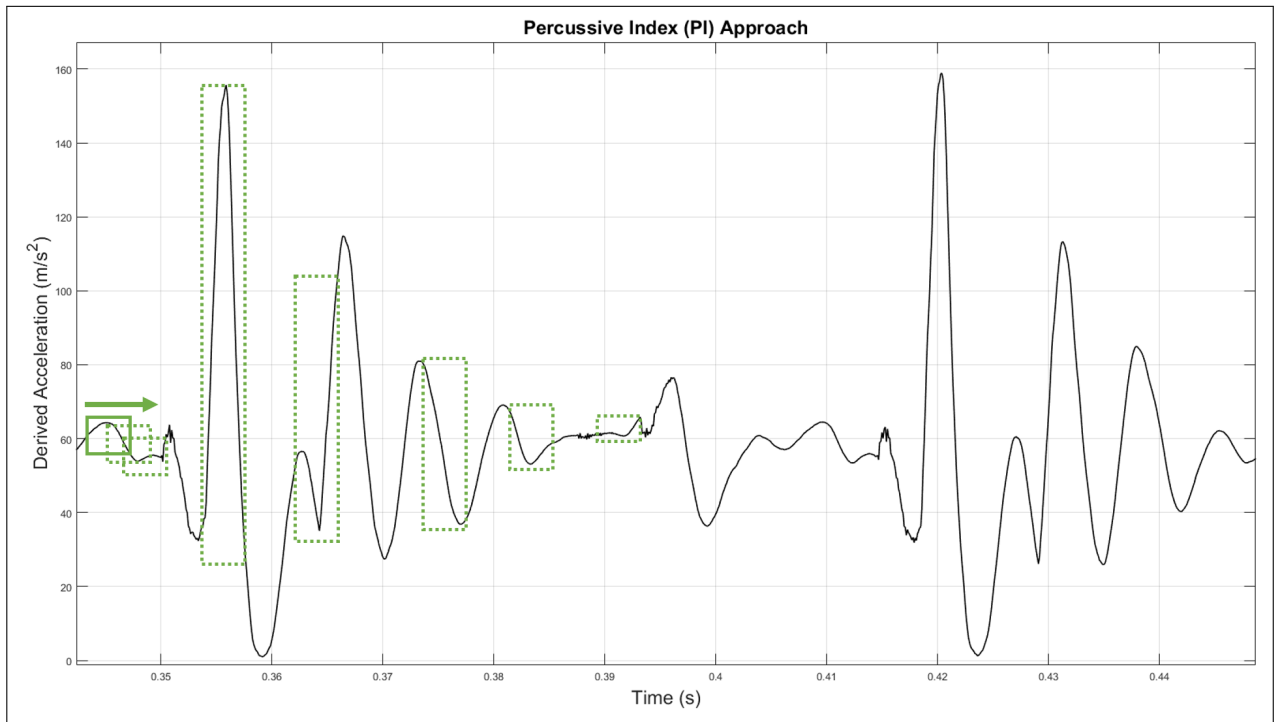
Figure 3.1: Illustrates the time constant, τ_c, represented as the width of the green box and as it progresses along the time-axis. Note the data points within the box are not exclusive to one returned index value; a portion of the data points in the box will overlap as the box moves forward in $\frac{\tau_c}{10}$ steps.

The index value calculated from Eq. 3.1 for each increment of τ_c is represented as a point with respect to time; the plot is complete once the entire derived acceleration data set has been indexed. The value of τ_c is determined by the highest peak value of an index plot, as shown in Fig. 3.2. For the applications of this thesis, the final PI-score for a given data set is calculated by summing all the index values.
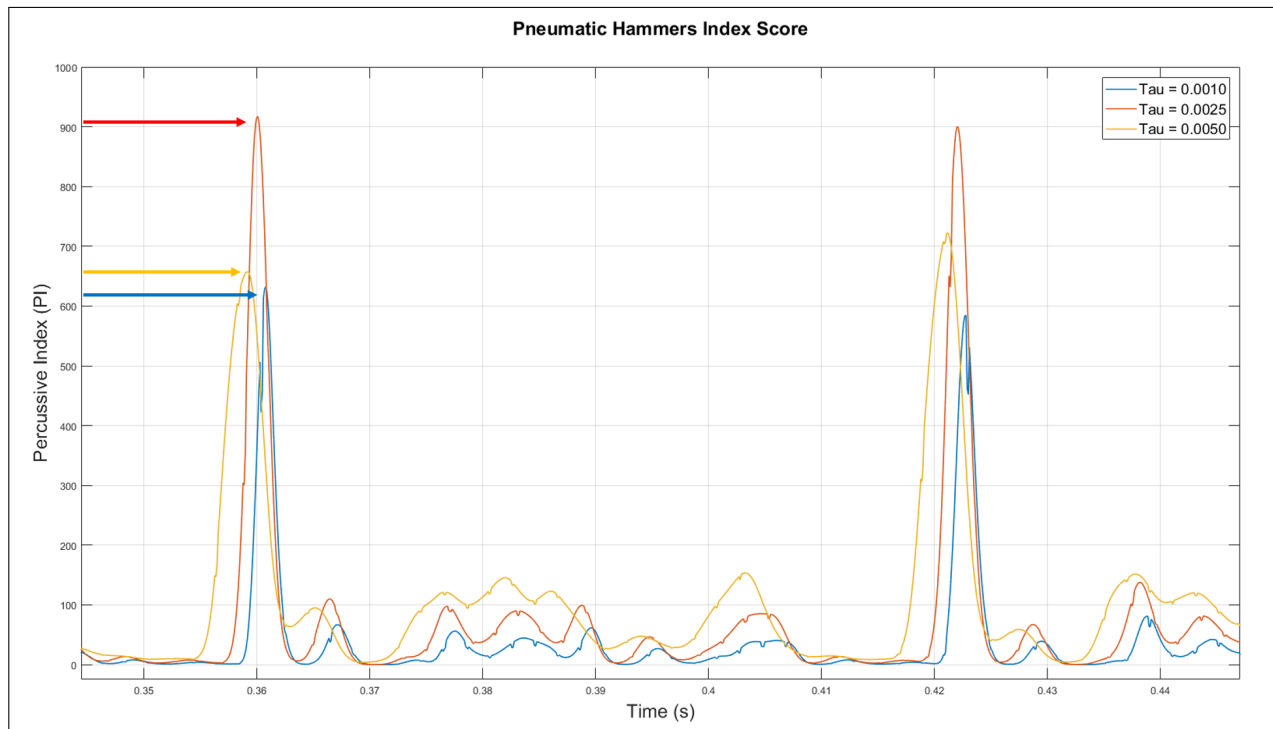
Figure 3.2: Illustrates the index plot generated from Fig. 3.1, and the method for determining τ_c through iteration. Note the ideal value for τ_c is the middle value (red-line), which produces the highest peak value in accordance with the method for implementing the HIC system.

Chapter 4

DYNAMIC SYSTEM MODEL

For the purpose of this thesis, the human arm is represented by a first-order system modeling a constant force being applied to a mass. Spring forces are not included in this model, since the spring constant of the muscles, ligaments, and tendons are unique to the individual and change based on the location of the fastener. For e.g., the body posture changes when riveting overhead as opposed to downward. Fig. 4.1 illustrates the arm position and corresponding linear graph for this first-order system [7]. The arm mass is calculated by summing the mass of one hand, one forearm, and half the value of one upper arm of a human with average build, totaling 2.9 kg [3], [11]

4.1   Forearm Stiffness

The stiffness of the forearm bone was considered when designing the dynamic system model. This was calculated with a Young's Modulus (E) of 18.6 GPa for the cortical bone shell, with a length of 262.2 mm, and an average cross-sectional area of 462 mm^2 for the hard outer bone shell of the radius [1], [19]. The stiffness (k) of the forearm bone was 32.7×10^6 N/m. The natural frequency was 534 Hz, which was calculated using the forearm mass determined in the previous section. With the stiffness of the forearm bone being so high, the mass of the tool and mass of the forearm were assumed to be rigidly coupled together, and considered a single mass for the model in this thesis. The calculations for determining the stiffness is found in Appendix C.

4.2 Ideal Model

In this model, the constant force of the arm, f, is produced by a constant pressure, P_c, over a fixed cross-sectional area, A, as shown:

$$f = -AP_c \ . \tag{4.1}$$

The second equation for this model has the velocity of air mass, V_m, defined by the flow rate, Q, over the fixed area, A, as shown:

$$V_m = \frac{Q}{A} \ . \tag{4.2}$$

The matrix form for equations 4.1 and 4.2 is as follows:

$$\begin{bmatrix} V_m \\ f \end{bmatrix} = \begin{bmatrix} 0 & \frac{1}{A} \\ -A & 0 \end{bmatrix} \begin{bmatrix} P_c \\ Q \end{bmatrix} \ .$$

The transfer function for the first-order system indicates the velocity as the output, with the force as the input, and is a $f(m)$ as follows:

$$T_1(s) = \frac{V_m(s)}{f(s)} = \frac{1}{ms} \tag{4.3}$$

4.3 Implementation Model

The ideal model does not take into account the response time of the valve manifold. This is the time required to adjust the pressure, to maintain a constant force on the mass as the pneumatic hammer and/or bucking bar are displaced. The displacement changes the volume of air within the large cylinders, which changes the pressure and in turn the clamping force. The implementation model proposed for this thesis consist of a mechanical and fluid component, related through a gyration transformation. The implementation model must also take into account a time constant, τ_c, to determine the response. Fig. 4.2 illustrates the linear graph model used to define five equations and two state variables: $\dot{V}_m$ and $\dot{P}_c$. These
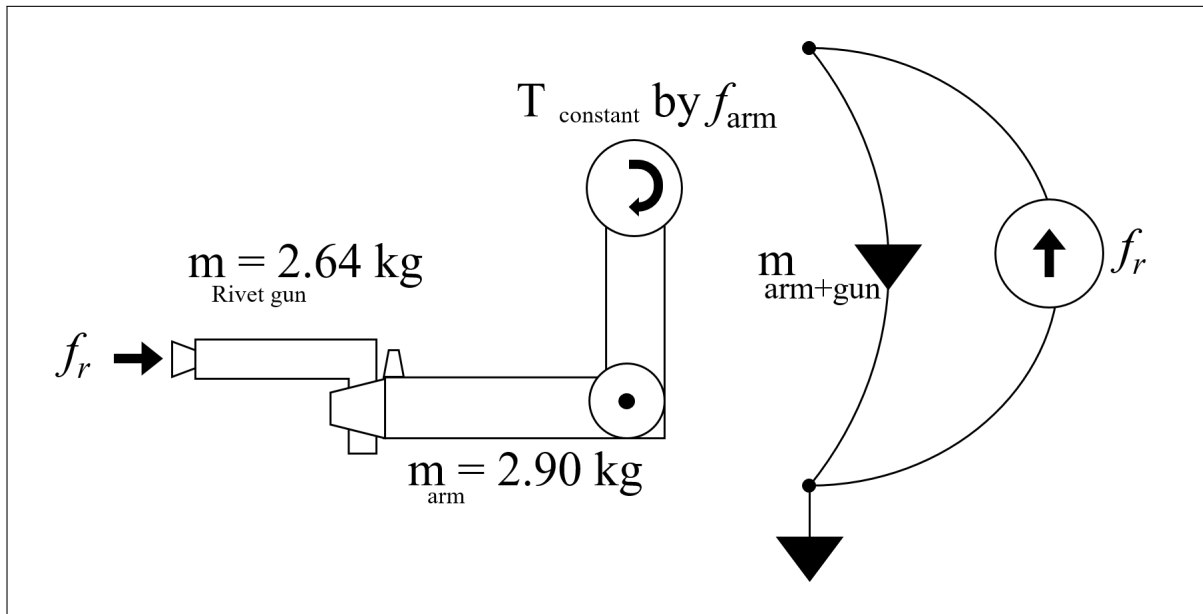
Figure 4.1: Depicts the orientation of the human arm and the constant force being applied from by a mechanic (left), and the linear graph representing the arm model (right). Additionally, the force from the pneumatic hammer, f_r, is presented here as reference for the test bench air cylinder model.

are defined by the mass, m, force of the mass, f_m, the capacitance, C, the capacitance flow rate, Q_c, the resistor, R, the pressure of the resistor, P_R, the flow rate of the resistor, Q_R, and the force of the pneumatic hammer, f_r. The five equations are as follows:

$$\dot{V}_m = \frac{1}{m} f_m \tag{4.4}$$

$$\dot{P}_c = \frac{1}{C} Q_c \tag{4.5}$$

$$P_R = R Q_R \tag{4.6}$$

$$Q_c = Q_R - Q \tag{4.7}$$

$$f_m = f_r - f \tag{4.8}$$
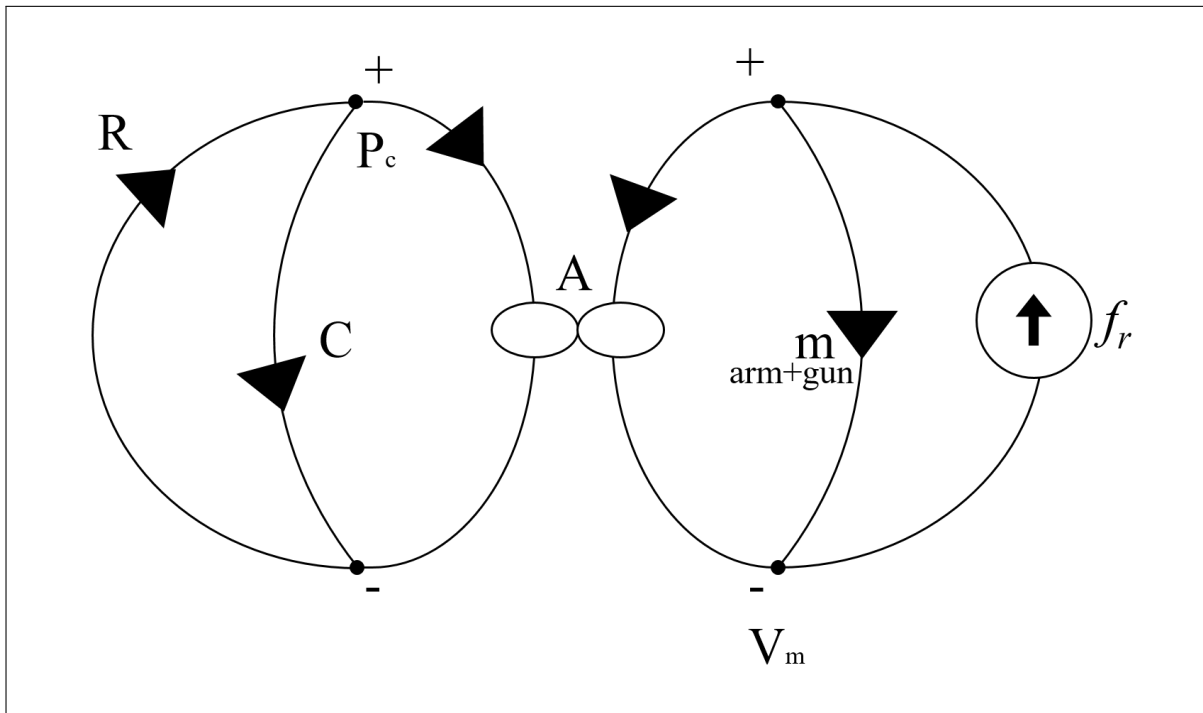
Figure 4.2: Depicts the linear graph model of the fluid to mechanical components through a gyrating transducer. This model relates the force of the air cylinder to the valve defined by capacitance and time constant, to the first-order human arm model. The time constant is determined by both the solenoid actuation and change in pressure response times.

The first state equation is by solved by substituting Eq. 4.1 and Eq. 4.8 into Eq. 4.4, giving the following:

$$\dot{V_m} = \frac{1}{m}f_m = \frac{1}{m}(f_r - f) = \frac{1}{m}(f_r + AP_c) \tag{4.9}$$

The second state equation is by solved by substituting Eq. 4.2, Eq. 4.6 and Eq. 4.7 into Eq. 4.5, giving the following:

$$\dot{P_c} = \frac{1}{C}Q_c = \frac{1}{C}(Q_R - Q) = \frac{1}{C}(-\frac{P_c}{R} - V_m A) \tag{4.10}$$

The corresponding $\dot{x} = Ax + Bu$ & $y = Cx$ form for Eq. 4.9 and Eq. 4.10 is as follows:

$$\dot{x} = \frac{d}{dt} \begin{bmatrix} V_m \\ P_c \end{bmatrix} = \begin{bmatrix} 0 & \frac{A}{m} \\ -\frac{A}{C} & -\frac{1}{RC} \end{bmatrix} \begin{bmatrix} V_m \\ P_c \end{bmatrix} + \begin{bmatrix} \frac{1}{m} \\ 0 \end{bmatrix} f_r$$

$$y = \begin{bmatrix} 1 & 0 \end{bmatrix} \begin{bmatrix} V_m \\ P_c \end{bmatrix}$$

The transfer function for the implementation model is again defined by velocity as the output and force as the input, and is a $f(A, \beta, \tau_c, m, Volume)$ as follows:

$$T_2(s) = \frac{V_m(s)}{f(s)} = \frac{\frac{1}{m}s + \frac{1}{mRC}}{s^2 + \frac{1}{RC}s + \frac{A^2}{mC}} \tag{4.11}$$

$$\omega_n = A\sqrt{\frac{1}{mC}} \tag{4.12}$$

$$\zeta = \frac{1}{2RA}\sqrt{\frac{m}{C}} \tag{4.13}$$

$$R = \frac{\tau_c}{C} \tag{4.14}$$

$$C = \frac{Volume}{\beta} \tag{4.15}$$

4.4 Model Responses

The desired $T_1(s)$ and actual $T_2(s)$ responses are plotted in Fig. 4.3 and show $T_2(s)$ is asymptotic to the magnitude of the desired first-order (mass-force) system near the driving frequency. The driving frequency of pneumatic hammers is $\approx 20 Hz$ in which case the higher the driving frequency, the closer $T_2(s)$ approaches the ideal model. For the given $T_2(s)$ model, the given time constant, $2.3\tau_c$, is $0.150\ s$, which represents the $0-90\%$ step response as defined by the manufacturer of the pressure regulator system. By applying the $\approx 63.2\%$ cutoff, the appropriate τ_c to model the response is $0.065\ s$.

A limitation of this model is the absence of total body weight. For this test bench, a higher clamping force from the air cylinder is used to ensure the pneumatic hammer recoupled to the fastener in time before the next strike is delivered, as the tool should never be fired

without the dye in contact to the rivet. To ensure proper contact, mechanics utilize their body weight to react to the forces generated by the pneumatic hammer, minimizing the distance of the recoil.
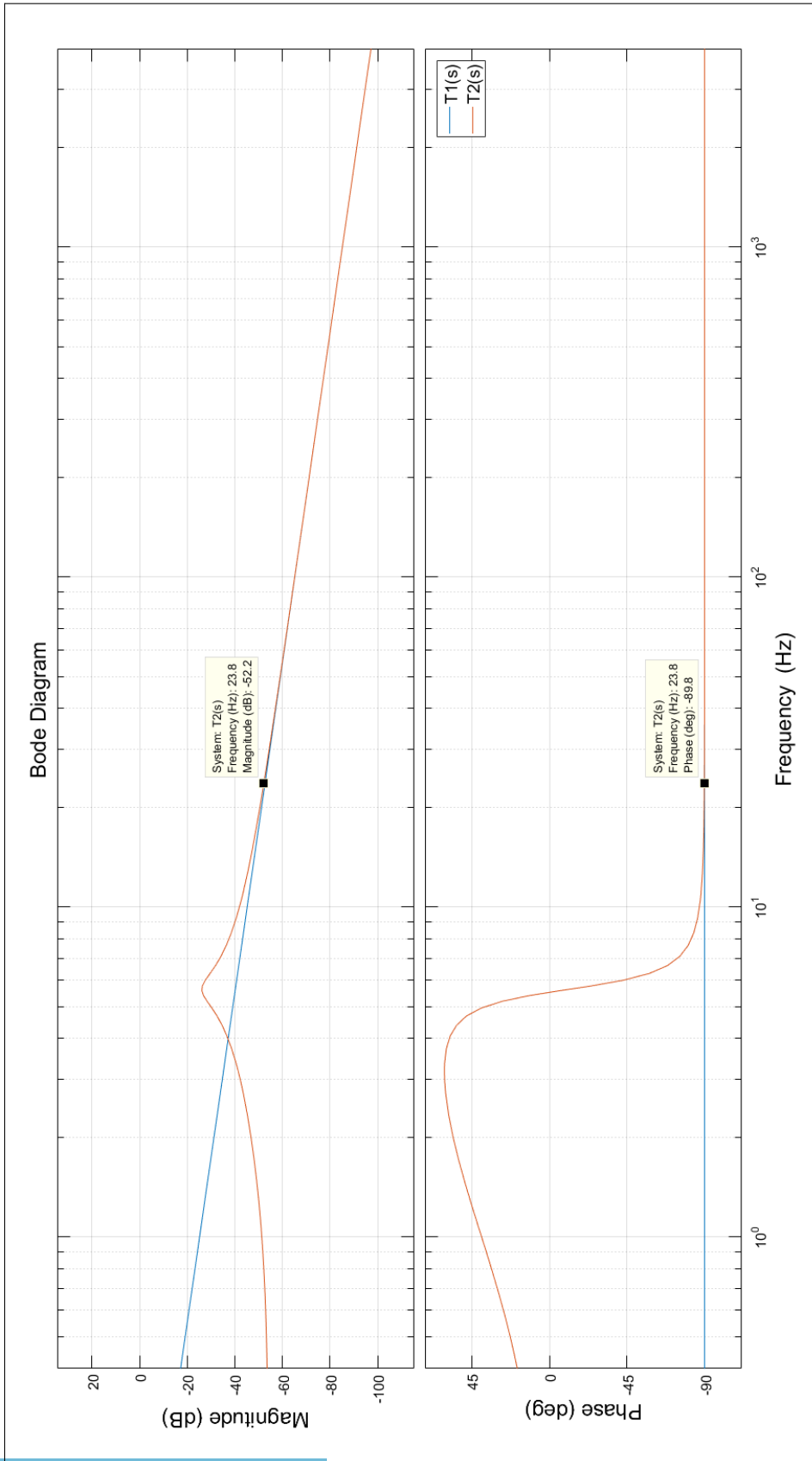
Figure 4.3: Illustrates the response of the system and the approximate driving frequency of 20 Hz. The ideal model is plotted in blue as $T_1(s)$ defined by Eq. 4.3, and produces a first-order linear response. The gyration transformation model is seen in red as $T_2(s)$ and modeled from Eq. 4.11. The MatLab script for this plot is found in Appendix C.

Chapter 5

TEST PROPOSAL

The constructed test bench is evaluated through two types of tests: (i) interference-fit bolt installations and (ii) percussive riveting for wing manufacturing.

5.1 Interference-Fit Bolt Installation

In addition to forming riveting, pneumatic hammers are also used to install interference-fit bolts, which is performed by a single mechanic. The process of installing bolts is commonly referenced to in aircraft manufacturing as driving in bolts rather than riveting. This test is ideal for evaluating pneumatic hammer independent of bucking bars. For this experiment, the nominal fastener/bolt diameter is 12.675 mm and nominal coupon hole diameter is 12.600 mm, as illustrated in Fig. 5.1. The coupon dimensions are 152 mm $\times$ 381 mm $\times$ 18 mm. The nominal bolt insertion distance from start to finish is 24.5 mm, and has an average installation time of 500 ms.

This test compares the Atlas Copco 12P to the Ingersoll Rand AVC27, as shown in Fig. 5.2. The 12P is designed with a built-in air damper between the rivet dye and barrel, reducing the forces experienced by the mechanic. This experiment is executed with the following two hardware settings:

- A trigger pull and hold duration of 800 ms.

- Constant clamping force of 235 N.

For this test, the trigger duration is set to be longer than the actual time required to fully seat the bolt into the coupon. Unlike rivets, there is little concern for over forming, also known as popping, the fastener. The benefit of hammering slightly longer ensures the bolt
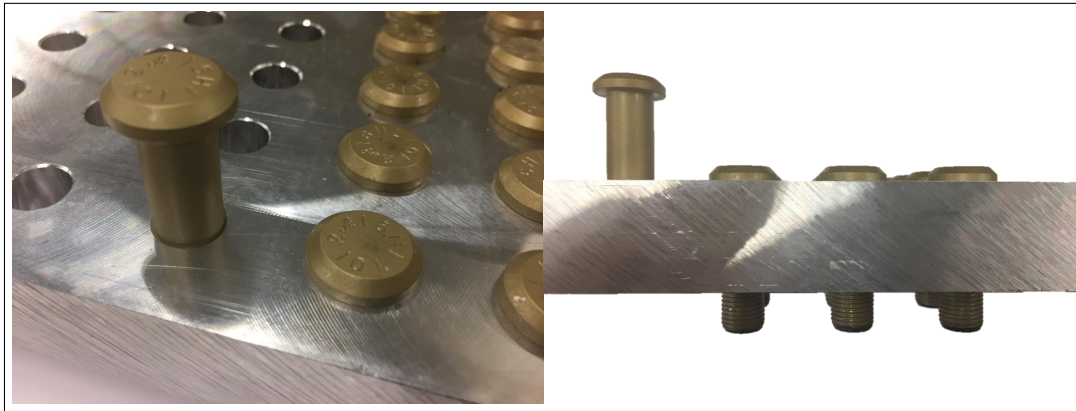
Figure 5.1: Displays the 12.675 mm bolts in a coupon with 12.600 mm interference fit holes, with a top view (left) illustrating the starting position for a bolt, and the fully seated position (right) with the threads present on the back side of the coupon.

is driven to completion, and both the start and finish positions are captured by the DAQ sensors. The actual end time is determined by when the bolt has been fully seated, in which case the laser does not detect anymore forward progress.

The second criteria for this experiment is to select a clamping force that is representative of a mechanic. While 235 N of force is not trivial to generate with a single arm, it is an approximation of the immediate force provided by the large inertial mass of a mechanic's body, in response to an impulse. This force simulates a mechanic leaning forward to minimize the tool from decoupling from the fastener.

The interference-fit bolt experiment investigates five parameters:

x_R Displacement per Strike (along the *z-axis*)

F_R Reaction Force

P_m Acoustic Pressure

t_f Exposure Duration

n_R Total Number of Strikes by Riveter

Figure 5.2: Displays the Altas Copco 12P (top) and the Ingersoll Rand AVC27 (bottom), both of which are tested in the interference-fit bolt experiment. The 12P has a mass of 2.23 kg and the AVC27 has a mass of 2.35 kg. The weight of the additional moving components, which include the linear rail block and collar is 0.50 kg. The total tested weight for the 12P is 2.73 kg, and 2.85 kg for the AVC27.

5.2 Percussive Rivet Installation

The proposed percussive riveting experiment uses 8 mm diameter rivets, which are installed in 8.010 mm holes. These rivets require ≈ 4 s to form a button diameter of ≥ 11.125 mm, and a button height of $3.175 - 5.080$ mm, as specified by the aerospace industry. This experiment is designed to compare the performance of two bucking bars of different weights, both of which are tested with the same Ingersoll Rand AVC27 from the previous experiment. The head shape of the bars are identical but vary in material and handle shape, and therefore overall tool weight. This experiment tests a 6.07 kg steel bucking bar, and a 8.75 kg tungsten bucking bar as illustrated in Fig. 5.3.

For this experiment, the force of the bucking bar is set to be $\approx 88\%$ of the rivet gun.

The hardware settings for testing the 8 mm rivets are as follows:

- A trigger pull and hold duration of 3000 ms.

- Constant pneumatic hammer clamping force of 356 N.

- Constant bucking bar clamping force of 312 N.

Unlike the previous interference-bolt experiment, the trigger duration is set to be less than the actual time required to fully form this type of rivet. This is because the change in deformation is more apparent earlier on, and can be used to determine how much progress each bar can achieve within the given time. If the trigger duration were to be set to allow both bucking bars to reach completion, their respective progress would become indistinguishable since the rivet may work harden and stop both bars within the specification - although one bar could have achieved specifications earlier.

For this experiment, the air cylinder clamping the bucking bar is set to be 44 N less than the air cylinder clamping the pneumatic hammer. During percussive riveting, the riveter applies more force than the bucker to ensure the rivet head is fully seated to fill in the counter sink. Fig. 5.4 illustrates this technique. Likewise, this approach provides the maximum amount of material to be available on the tail end to produce the button as shown in Fig. 5.5.

The percussive riveting experiment investigates six parameters:

x_B Bucking Bar Displacement

x_D Bucking Bar Recoil

F_B Bucker Reaction Force

P_m Acoustic Pressure

$\o_B$ Button Diameter

h_B Button Height
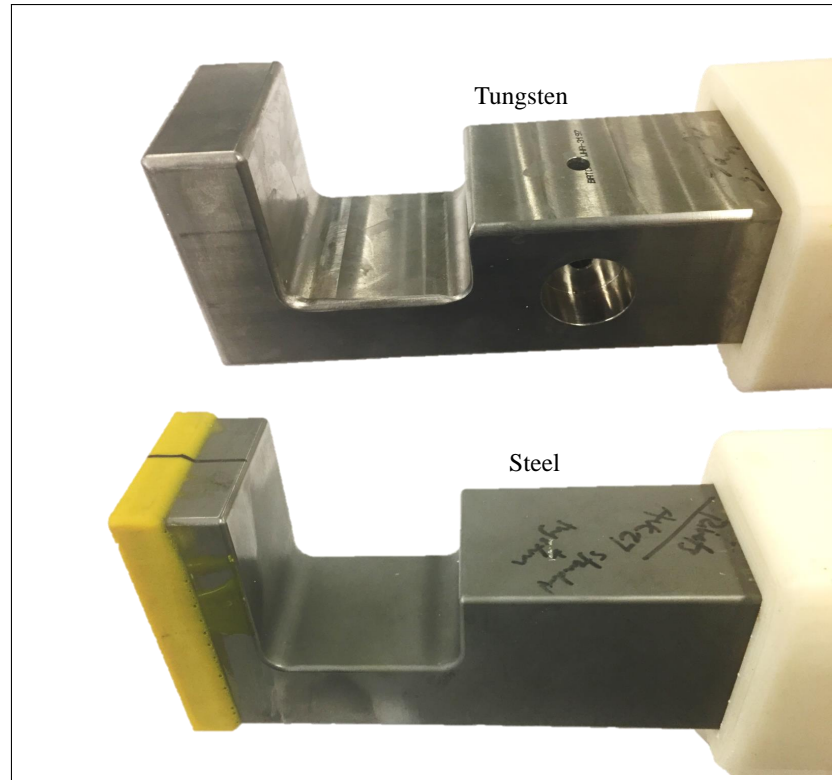
Figure 5.3: Displays the tungsten bucking bar (top) and steel bucking bar (bottom). Note, the yellow face on the steel bucking bar is a rubber scratch guard that only borders the edges, preventing the bar from scratching the panels during misuse; there is no advantage or disadvantage under the circumstances of this experiment. While the head shapes are identical, the mass of the steel bucking bar is 69.3% of its tungsten counterpart.
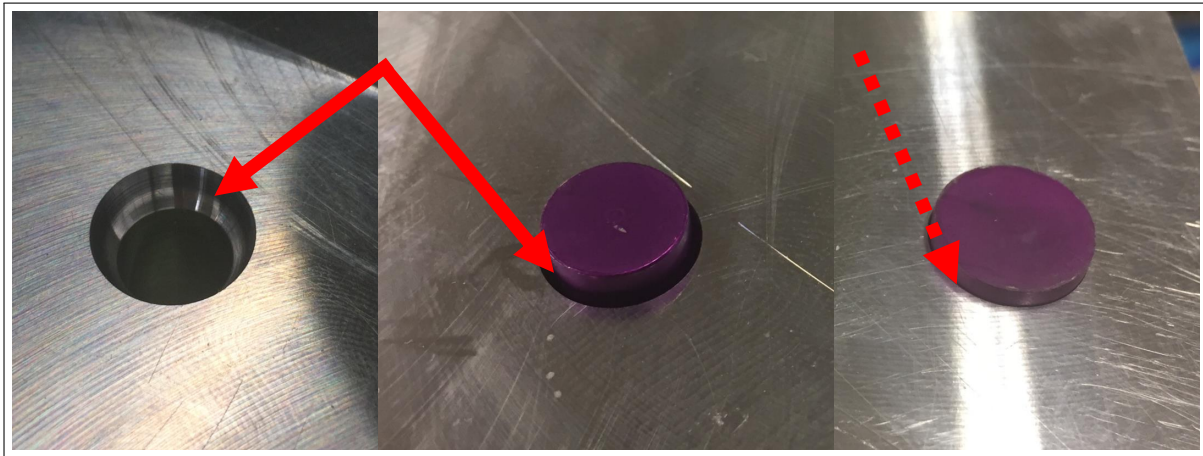
Figure 5.4: Illustrates the head formation of the rivet in three stages. The countersink is visible and ready to receive the appropriate sized rivet (left). The rivet is placed into the hole, and the countersink remains partially visible (center). The rivet is formed, causing the head of the rivet to fill in the countersink (right). The countersink is flagged by solid red arrows, and the filled countersink is indicated by the dashed red arrow.
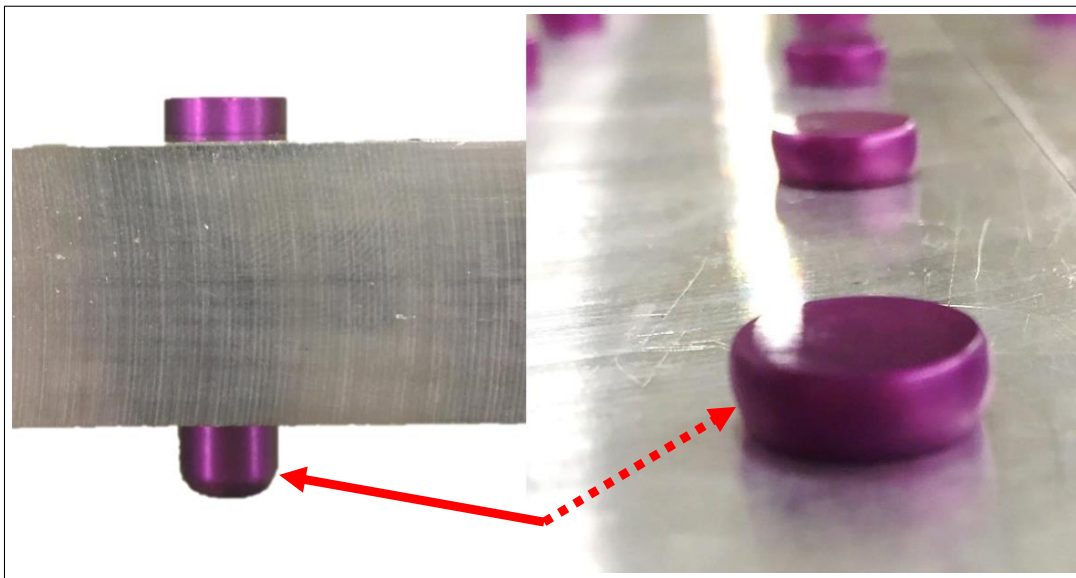
Figure 5.5: Displays the side view of a rivet prior to being formed (left), and a bottom view of the riveted tail end (right). The solid red arrow indicates the tail end, and the dashed red arrow examples how the tail end is flattened and formed into a button shape.

Chapter 6

EXPERIMENTAL RESULTS

6.1 Bolt Installation Results

For this experiment the Ingersoll Rand AVC27 and Atlas Copco 12P each drove four bolts ($n = 4$). The results indicated the 12P completed the bolt installation task in 0.31 s and with 7 strikes over the average of four runs, whereas the AVC27 required 0.43 s and 8 strikes. These values indicate the 12P fired at $\approx 22\ Hz$, and the AVC27 at $\approx 19\ Hz$. The start time was determined by the first displacement value above 3e$-3\ mm$ from the zeroed starting position, which was 150% of the oscillating amplitude for steady-state noise. The end time was determined by taking the final displacement value of the pneumatic hammer at rest $\approx 24.5\ mm$, and indexing the time in which this value first appeared. The laser displacement is illustrated in the top plot of Fig. 6.1.

The peak reaction forces registered on the pneumatic hammer load cell, F_R, of the AVC27 was substantially higher than the 12P, with an average of 1048 N, compared to 307 N, respectively. A summary of the mean peak forces for each strike, and total force, F_T, measured from the load cells, are found in Table 6.1. The average total impulse, area under the force-time plot, for the 12P was 64.50 Ns, and 131.30 Ns for the AVC27. This plot is exampled in the bottom of Fig. 6.1. This was calculated by Eq. 6.1. The significant reduction in impulse for the 12P was due to the absence of the excitation peak, and the 12P achieving completion in < 75% of the time for the AVC27.
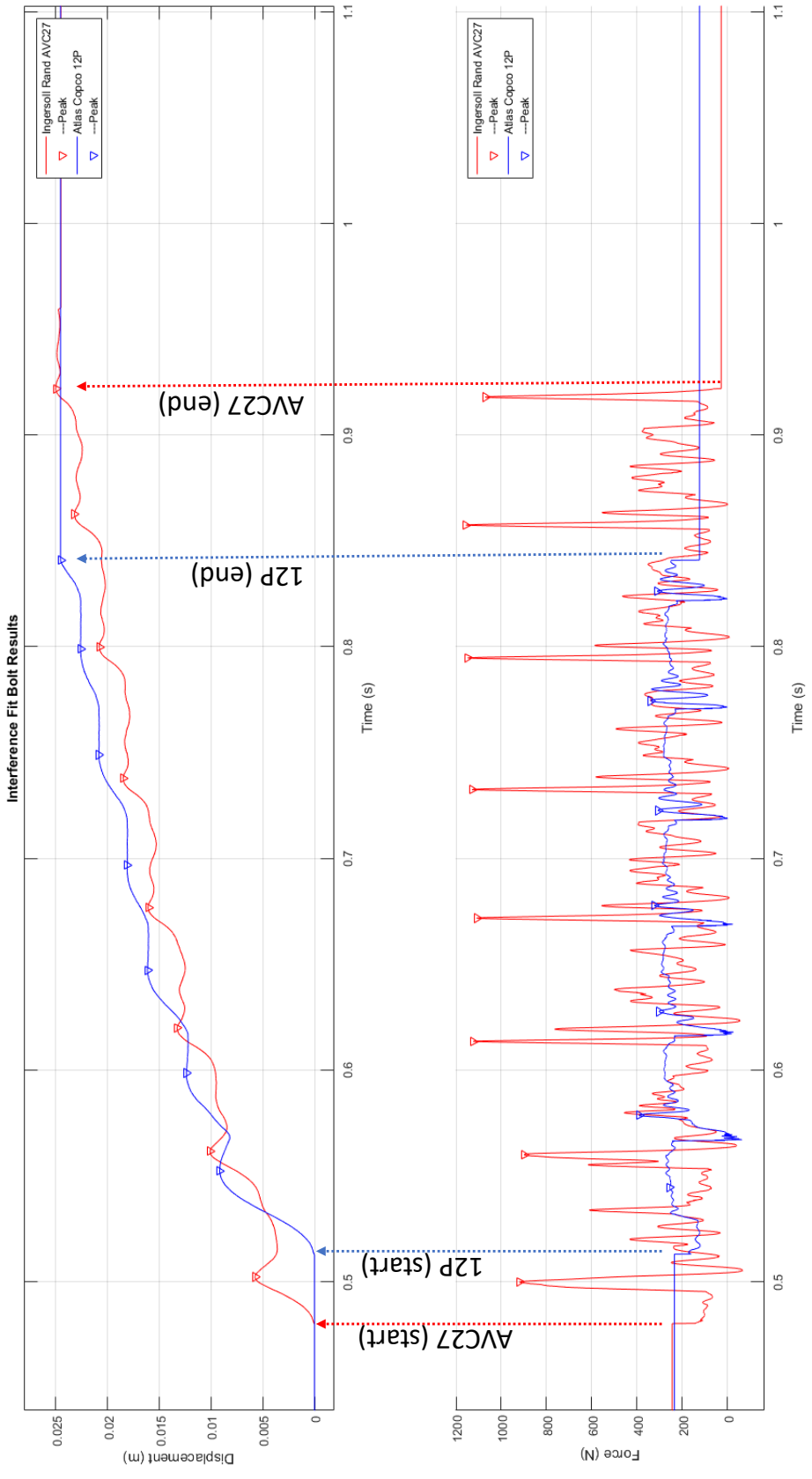
Figure 6.1: Displays an example of the processed laser displacement data (top), and load cell data (bottom) for both the AVC27 and 12P. The peaks on the laser displacement plot, marked by a del, ▽, indicate the displacement of the bolt with respect to a single strike, while the troughs represent the recoil of the pneumatic hammer. The del, ▽, on the load cell plots indicate the peak forces associated with the displacement, as both are plotted on the same time-scale.

$$Impulse\ (J) = \int_{t_0}^{T} F_R\ dt$$

$$where \begin{cases} t_0 = time\ corresponding\ to\ first\ peak\ (s) \\ T = time\ corresponding\ to\ final\ peak\ (s) \end{cases} \tag{6.1}$$

Another approach to reviewing the findings was by correlating the displacement per strike to the respective peak forces, providing a general understanding of the work performance of each pneumatic hammer. Fig. 6.2 displays both the AVC27 and 12P approaching the $\approx 24.5\ mm$ end mark, however on different tracks. The results indicated the 12P completed the same task as the AVC27 while applying less force on the load cell.

While the 12P had shorter exposure duration, t_f, and, F_T, than the AVC27, the 12P was found to produce a higher acoustic pressure. On average, the 12P produced $32.95\ Pa$ with each strike, while the AVC27 produced $20.01\ Pa$. These values were converted to $124\ dB$ and $120\ dB$ for the 12P and AVC27, respectively, using Eq. 6.2. The raw and processed sound pressure level results are listed in Appendix A.1 and A.2. Note, recall that the microphone is fixed at $\approx 0.07\ m$ from the head of the pneumatic hammer, and the actual pressures reaching the ears of a mechanic is less when taking into account the additional distance.

$$Ł_p(dB) = 20log\frac{p_0}{P_m}$$

$$p_0 = 20\text{e}{-}6\ Pa\ (air) \tag{6.2}$$

The 12P was also found to experience a larger change in pressure during the first strike of every test, compared to the AVC27. The AVC27 had a mean pressure drop, or change, of $72.49\ kPa$, while the 12P consumed on average, $98.76\ kPa$ for the first strike. The pressure change for the remaining strikes for both pneumatic hammers did not significantly differ, averaging $47.01\ kPa$. The larger air consumption of the 12P was due to the air damper recoiless feature. The results confirmed both pneumatic hammers received the same starting air pressure, of $\approx 790\ kPa$, for all eight tests. Table 6.2 summarizes the results. The complete charts for the Ingersoll Rand AVC27 are found in Appendix A.1 and A.2. The charts for the Atlas Copco 12P are found in Appendix A.3 and A.4.

Averaged Reaction Force per Sequential n_R Strike
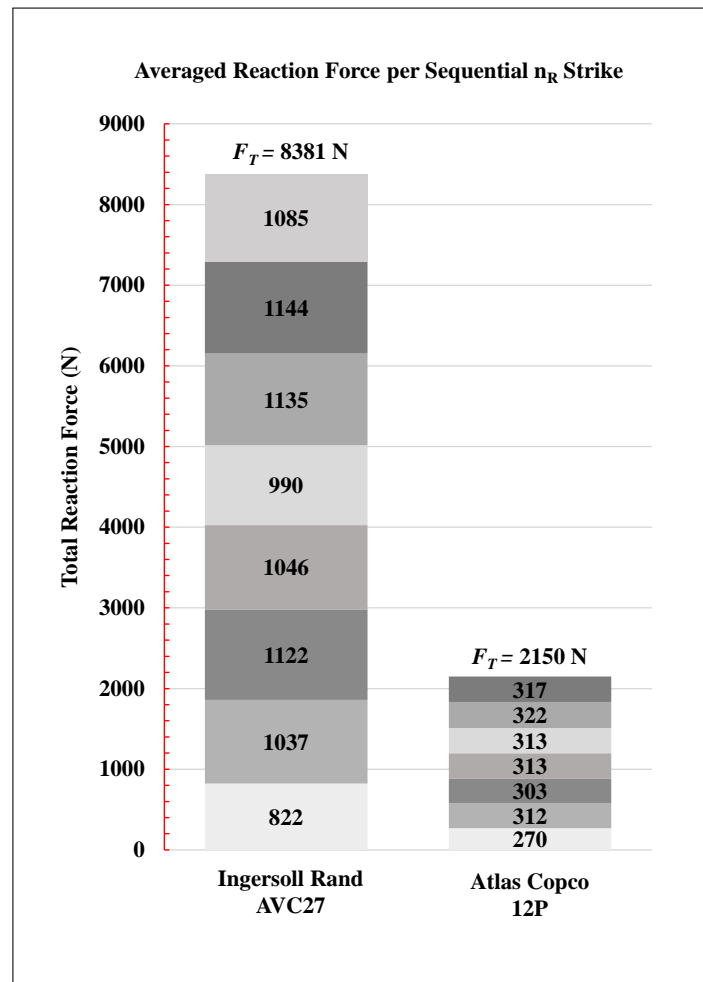
Table 6.1: Display the averaged peak reaction force for each of the 8 strikes, represented by 8 stacked bar boxes for the AVC27, and 7 strikes for the 12P. These values are stacked to illustrate the total magnitude of cyclic loads, F_T, associated with each pneumatic hammer. The summed peak forces of the AVC27 was ≈ 3.9 times that of the 12P.
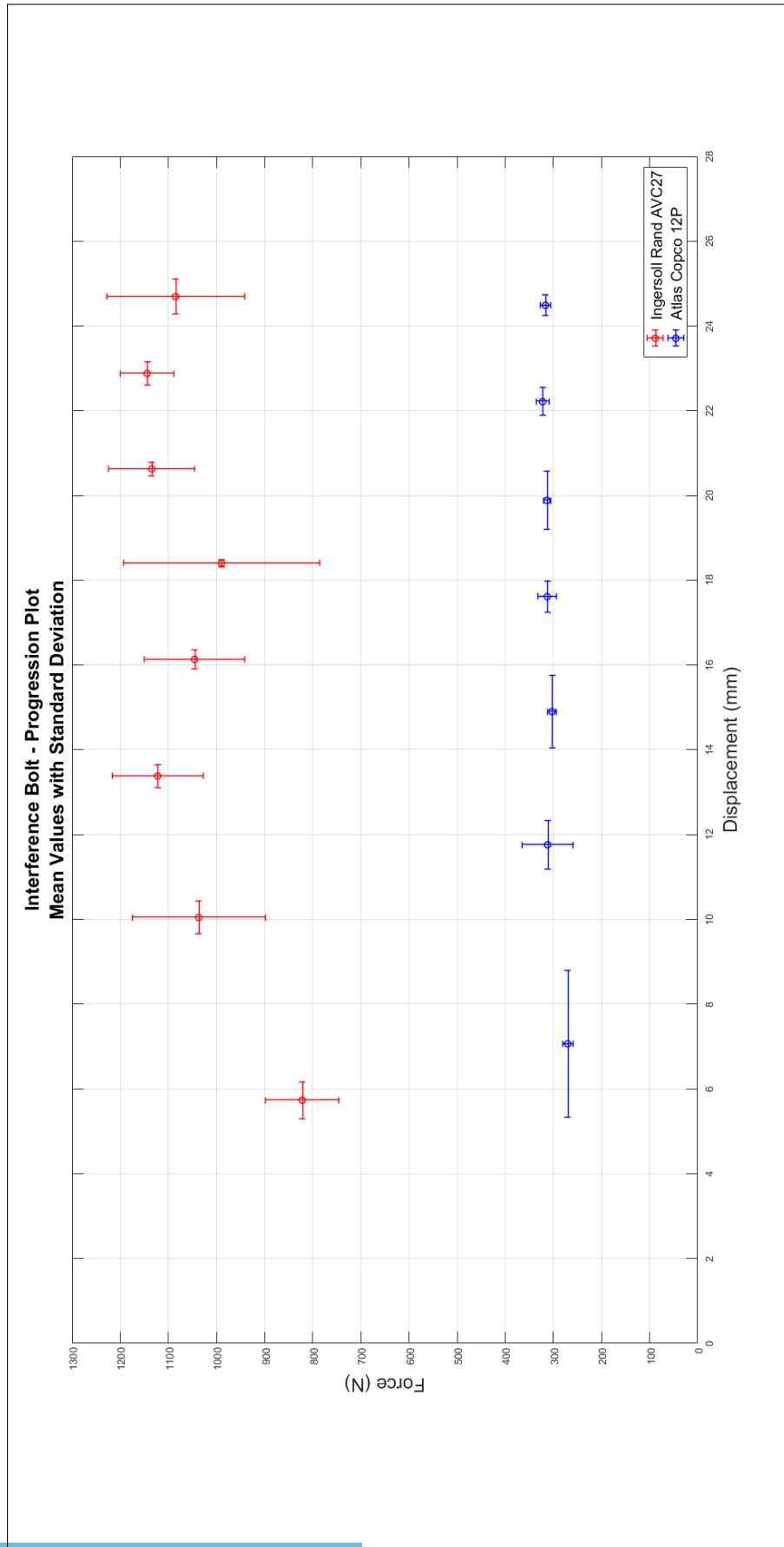
Figure 6.2: Presents the averaged reaction forces and averaged displacements with respect to each strike. The Ingersoll Rand AVC27 has eight points, and the Atlas Copco 12P has seven points, representing the number of strikes. The standard deviation is calculated for each strike and illustrated by the error bars, vertical for the error range of forces, and horizontal for the displacement. The larger error for the first strike on the 12P along the displacement axis is due to the inconsistent starting position of the slug.

Parameter	Ingersoll Rand AVC27	Atlas Copco 12P
Displacement, X_R (per strike)	3.07-mm	3.51-mm
Mean Reaction Force, F_R	1048-N	307-N
Derived Acceleration, a_R	Max: 114-m/s^2, Mean: 26-m/s^2	Max: 25-m/s^2, Mean: 14-m/s^2
Total Impulse, J	131.30-Ns	64.50-Ns
Noise Level, P_m	120-dB	124-dB
Air Consumption, ΔP	First: 72-kPa, Mean: 47-kPa	First: 99-kPa, Mean: 47-kPa
Exposure Duration, t_f	0.43-s	0.31-s
Total Strikes, n_R	8	7

Table 6.2: Summarizes the results of the interference-fit bolt experiment.

Following the index scheme found in Eq. 3.1, the 12P averaged a PI-score = 287, and the AVC27 had a PI-score = 704. Appendix A.3 displays the trends of all eight runs, with the final value for each plot representing the PI-score. At this time, the likelihood of injury cannot be inferred from these PI-scores such as doubling the score does not correlate with injury to occur twice as likely. Defining a safe perimeter of operation will require further testing beyond the scope of this thesis.

6.2 Percussive Riveting Results

For this experiment, the tungsten bucking bar formed a larger button diameter within the same given duration and number of strikes, $n_R = 56$, as the steel bucking bar. Over the course of four runs each ($n = 4$), the tungsten produced a button diameter of 10.732 mm and height of 5.175 mm. The steel bucking bar formed an average diameter of 10.370 mm and height of 5.588 mm. The tungsten came within 87% of the minimum require diameter, while the steel reached 76%. Additionally, the average button height for the tungsten bar was within 96%, while the steel bar was 87% of the height range. Table 6.3 summarizes the results of the button diameters and heights.
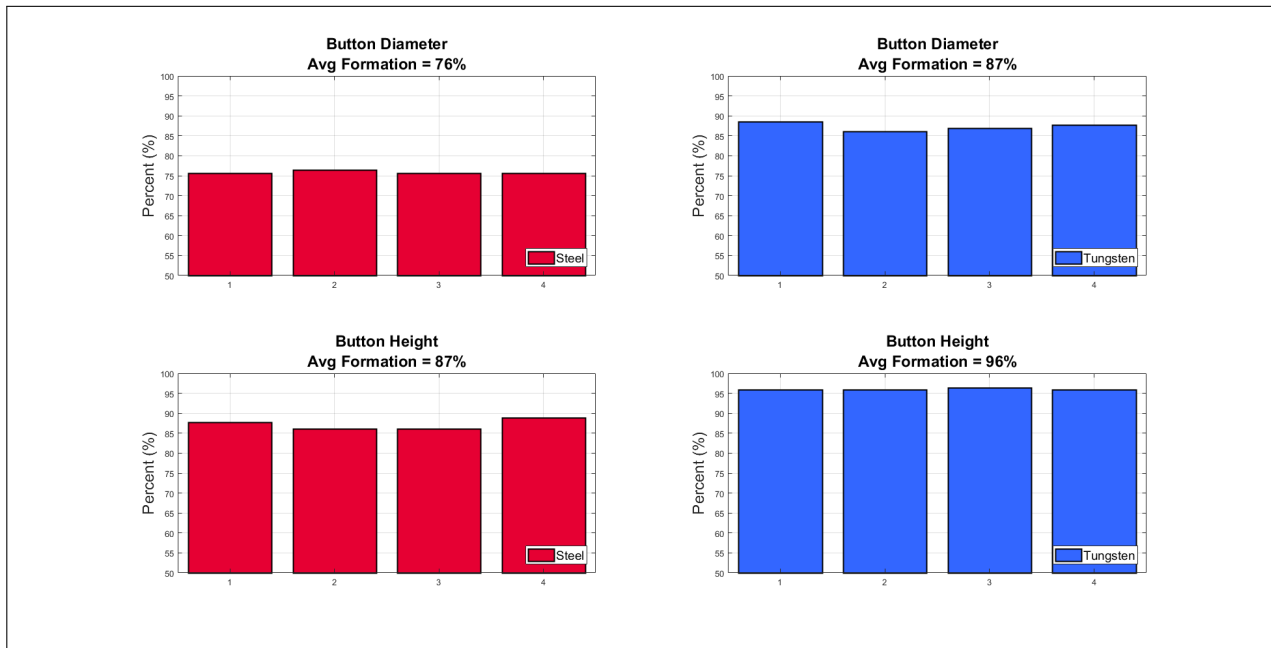
Table 6.3: Summarizes the button diameters and heights for each rivet run with respect to the selected bucking bar. The tungsten bar was found to produce 11% more button formation and 9% more button height than the steel bar. These values were calculated using Eq. 6.3 and Eq. 6.4.

$$Button\ Diameter\ Formation\ \% = \frac{\o_B - \o_{start}}{\o_{goal} - \o_{start}} \times 100$$

$$given \begin{cases} \o_{start} &= 8.000\ mm \\ \o_{goal} &= 11.125\ mm \end{cases} \tag{6.3}$$

$$Button\ Height\ Formation\ \% = \frac{h_{start} - h_B}{h_{start} - h_{goal}} \times 100$$

$$given \begin{cases} h_{start} &= 9.690\ mm \\ h_{goal} &= 5.080\ mm \end{cases} \tag{6.4}$$

The difference in button height for the two bucking bars was also seen in the laser displacement. The tungsten achieved 8% more displacement than the steel bar. The discrepancy

Parameter	Steel Bucking Bar	Tungsten Bucking Bar
Recoil, X_D (per strike)	1.77-mm	1.43-mm
Mean Reaction Force, F_B	1456-N	1195-N
Derived Acceleration, a_R	Max: 149-m/s^2, Mean: 41-m/s^2	Max: 114-m/s^2, Mean: 31-m/s^2
Total Impulse, J	1059-Ns	1056-Ns
Button Diameter	10.370-mm	10.732-mm
Button Height	5.588-mm	5.175-mm
Mean Reaction Force, F_R	837-N	801-N
(Total Strikes, n_R)	56	56
(Noise Level, P_m)	120-dB	120-dB
(Air Consumption, ΔP)	First: 73-kPa, Mean: 47-kPa	First: 72-kPa, Mean: 46-kPa

Table 6.4: Summarizes the results of the 8 mm rivet experiment. The bottom three parameters with parenthesis pertain to pneumatic hammer used, indicating both tests were executed under equivalent conditions.

between this 8% and the physically measured button height of 9% previously stated may be accounted for by the deflection of the test bench and coupon. Based on the laser data, the tungsten bar was also found to experience 15% less recoil than the steel bar. For this test, bucking bar recoil was defined as the difference between the peak displacement and the trough that followed. Fig. 6.3 displays the trend of the tungsten and steel bars, along with the calculated recoil. Note, the final displacement peak does not directly correlate with the total travel (displacement), as clarified in Appendix B.1.

The average load cell measurements, or F_R, on the back of the tungsten and steel bars were 1195 N and 1456 N respectively, indicating an 18% reduction in peak magnitudes for tungsten. The average total impulse for the tungsten was 1056 Ns, and 1059 Ns for steel, using Eq. 6.1, which was a $< 0.5\%$ difference. The mean reaction force on the rivet gun when tested with the tungsten was found to be 4% lower, than when paired with the steel bar. The static and differential pressure measurements to the AVC27 for both tested registered within $0.8 \pm 1.0\%$ for all eight runs, indicating both bars were tested under equivalent conditions.
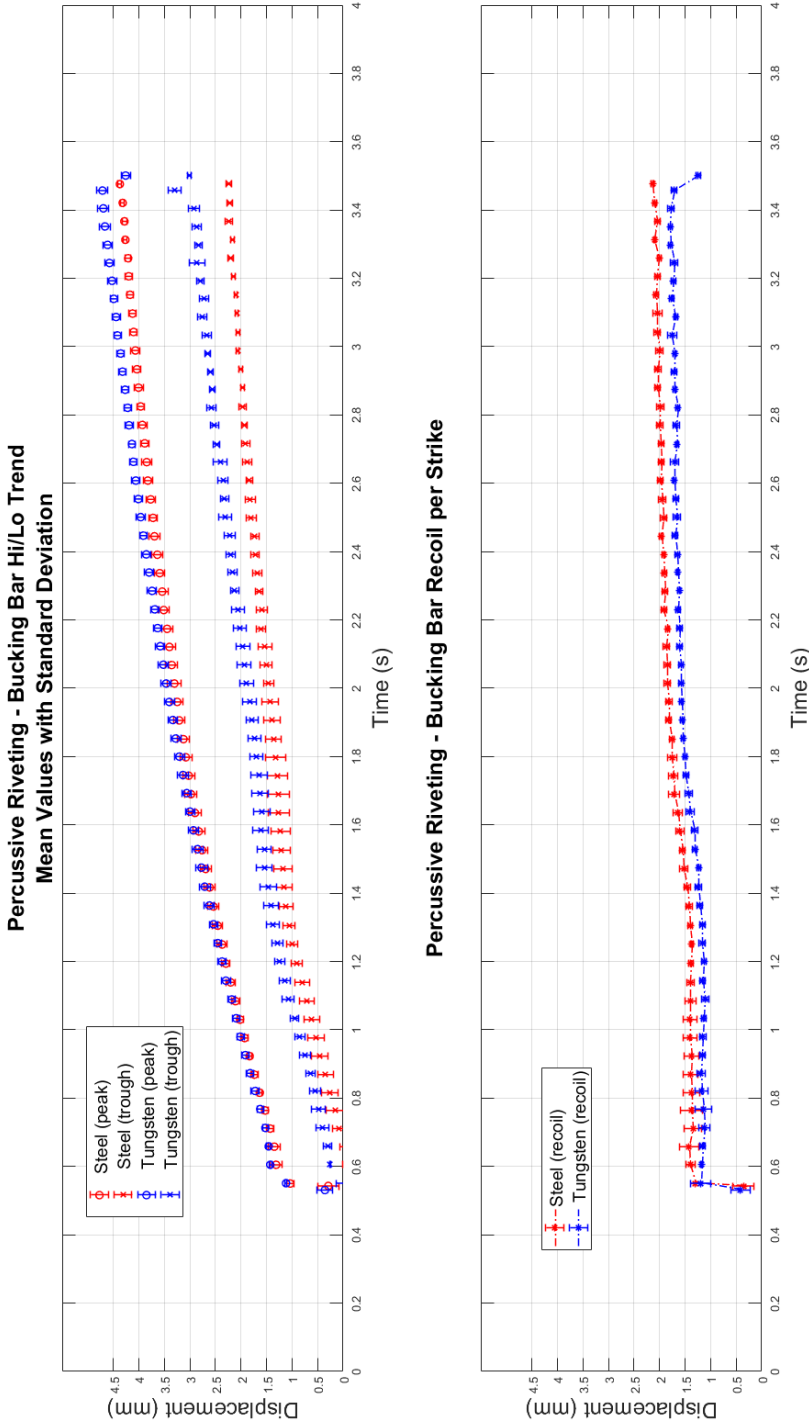
Figure 6.3: Presents the averaged peak and trough displacement values for the two bucking bars (top), along with their standard deviation. The peak values for tungsten extended beyond the steel, inferring that a larger button diameter and shorter button height were achieved, compared to the steel. The averaged recoil values (bottom) shows the tungsten bar trending at a lower magnitude, and after the 10th strike right before the 1 s mark, both plots part ways by more than one standard deviation for the remainder of the run.

While the tungsten bar did not produce a difference in the overall impulse, as seen between the two pneumatic hammers in the previous experiment. The tungsten bar achieved more rivet deformation, which inferred a shorter work duration over the steel bucking bar if the test duration was extended. Fig. 6.4 displays the tungsten bar as producing more displacement with less force.

The Percussive Index defined by Eq. 3.1, was also applied to this experiment to further develop its use. The tungsten bucking bar averaged a PI-score $= 7,541$, while the steel averaged $21,472$. The AVC27 pneumatic hammer used with the tungsten bucking bar averaged a PI-score $= 23,658$, and then $26,070$ when paired with the steel bar. Compared to the interference-fit results, the PI-score for the AVC27 pneumatic hammer was significantly higher when applying a higher clamping force and additional number of strikes (going from $n_R = 8$, to $n_R = 56$). The plots for the PI-scores are found in Appendix. B.4 and B.5.

The results indicated the tungsten bucking bar was capable of forming rivets in a shorter amount of time, while reducing the overall forces both the riveter and bucker are exposed to in this process, additionally the bucker experiences less recoil in exchange for carrying a heavier tool.
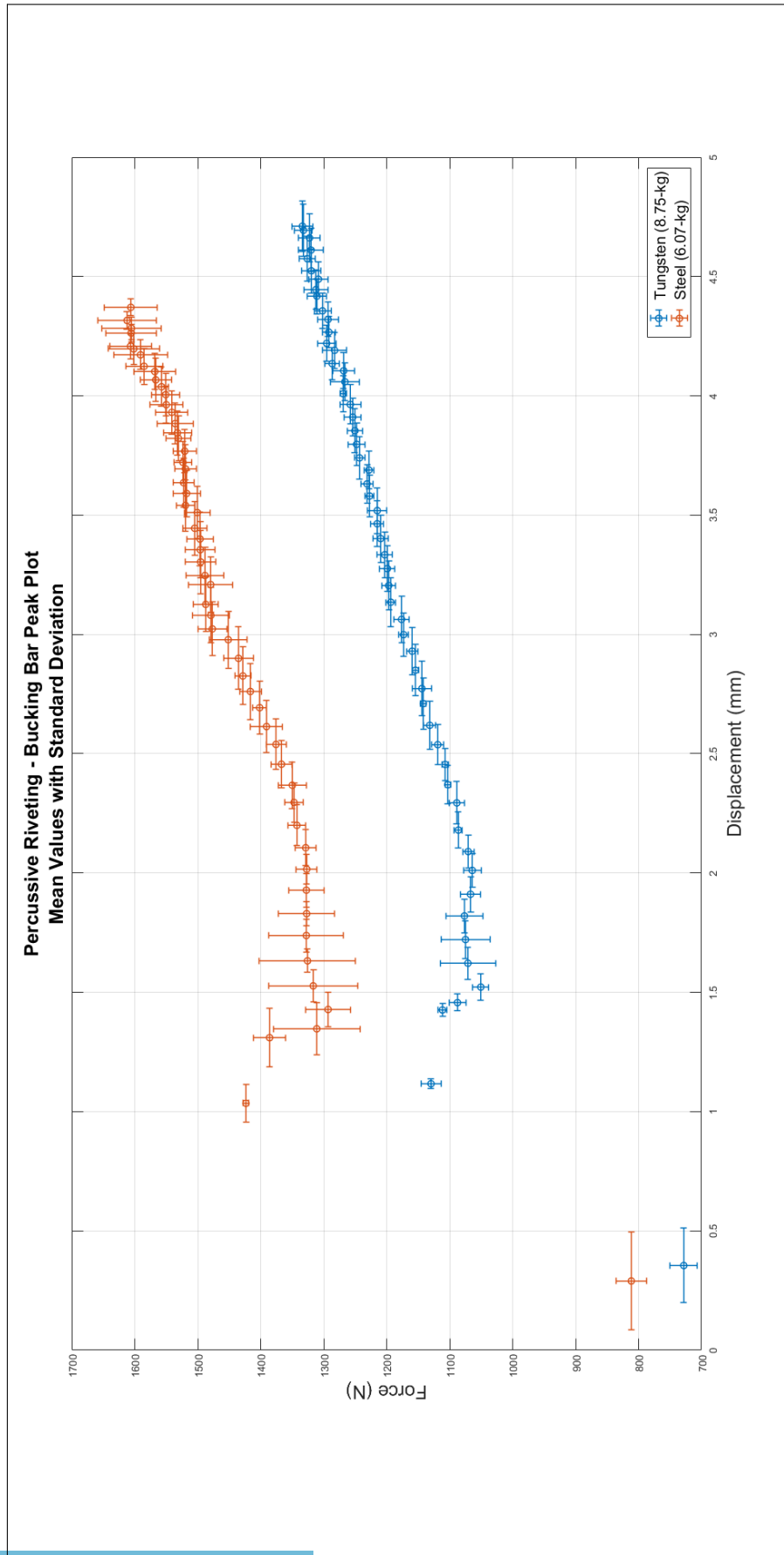
Figure 6.4: Plots the peak reaction forces with respect to the peak displacements for the tungsten and steel bucking bars. The mean values and standard deviation were applied to each point. The mean final peak displacement for tungsten and steel were 4.71 *mm* and 4.37 *mm*.

Chapter 7

CONCLUSION

In this thesis, we proposed designing an automated test bench to conduct ergonomic evaluations, which was validated with dynamic system modeling and by the data it produced. By modeling the test bench to represent a human mechanic installing percussive fasteners, and the use of actual fasteners and materials, we were able to correlate tool performance to human-stress factors. Automating this process achieved test repeatibility and granted the use of a previously established index, defined as a $f(F_R, t_f, m_T)$.

The test bench determined the Atlas Copco 12P completed bolt installations in 72% of the time the Ingersoll Rand AVC27 required, and generated 52% less total impulse on the load cell. This indicated the optimal pneumatic hammer for installing 12.675 mm interference-fit bolts was the Atlas Copco 12P (with the built-in recoiless feature). With regards to the bucking bar experiment on 8 mm wing rivets, the test bench determined the tungsten bar provided 11% more rivet formation in the same amount of time as the steel bar, while also reducing the recoil and peak load cell forces by 15% and 18%, respectively. The test bench quantitatively concluded a heavier bucking bar, if able to be wielded by a mechanic, improves tool performance.

Future improvements to this study involve:

- Further investigating the applications of an index to compare and grade percussive tools.

- Develop a second generation dynamic system model to include materials representing the soft tissue of the hand and wrist joint, and mass of the human body.

- Normalize the starting position of the slug in pneumatic hammers, improving consistency of the first strike for each test and across all tools.

- Determine the significance of applying a ramp input to vary the clamping force while hammering, to simulate a mechanic pushing harder as the rivet becomes more difficult to form following each strike.

- Incorporate finite element analysis to model the vibrations generated by the cyclic loading, as seen in Fig. 7.1.
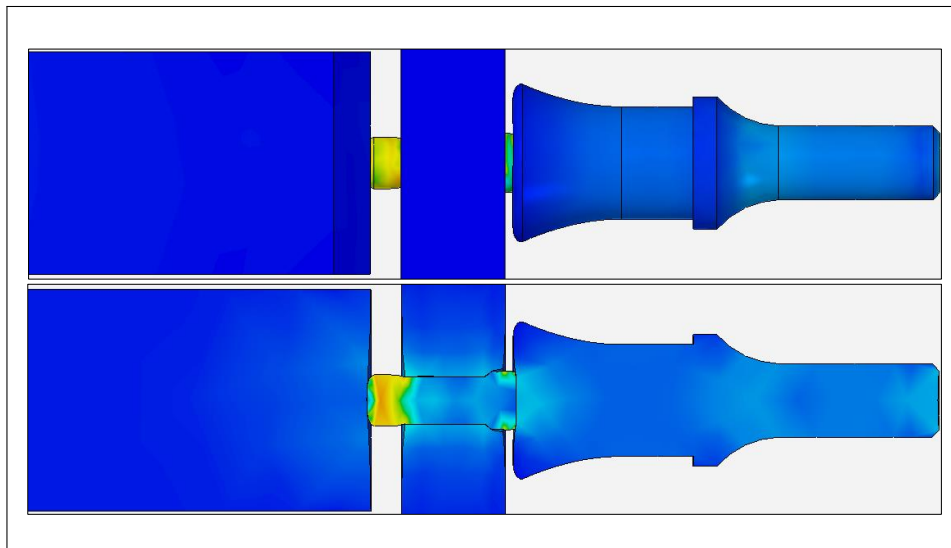
Figure 7.1: Displays finite element model of percussive tools forming an 8 mm rivet from the exterior view (top), and lengthwise cross-sectional view (bottom). A pneumatic hammer dye from the Ingersoll Rand AVC27, and flat steel bucking bar is used in simulating the first strike.

BIBLIOGRAPHY

[1] Thomas Baum, Melanie Kutscher, Dirk Muller, Christop Rath, and Felix Lochmuller. Cortical and trabecular bone structure analysis at the distal radius-prediction of biomechanical strength by DXA and MRI. *Journal of Bone and Mineral Metabolism*, 31(2):212–221, 2013.

[2] John G. Cherng, Mahmut Eksioglu, and Kemal Kizilaslan. Vibration reduction of pneumatic percussive rivet tools: Mechanical and ergonomic re-design approaches. *Applied Ergonomics*, 40(2):256–266, 2009.

[3] Charles E Clauser, John T McConville, and J W Young. Weight, Volume, and Center of Mass of Segments of the Human Body. *National Technical Information Service*, pages 1–112, 1969.

[4] Brian D. Curry, James L W Bain, Ji Geng Yan, Lin Ling Zhang, Mark Yamaguchi, Hani S. Matloub, and Danny A. Riley. Vibration injury damages arterial endothelial cells. *Muscle and Nerve*, 25(4):527–534, 2002.

[5] Brian D. Curry, Sandya R. Govindaraju, James L W Bain, Lin Ling Zhang, Ji Geng Yan, Hani S. Matloub, and Danny A. Riley. Evidence for frequency-dependent arterial damage in vibrated rat tails. *Anatomical Record - Part A Discoveries in Molecular, Cellular, and Evolutionary Biology*, 284(2):511–521, 2005.

[6] R. G. Dong, A. W. Schopper, T. W. McDowell, D. E. Welcome, J. Z. Wu, W. P. Smutz, C. Warren, and S. Rakheja. Vibration energy absorption (VEA) in human fingers-hand-arm system. *Medical Engineering and Physics*, 26(6):483–492, 2004.

[7] Ren G. Dong, Erik W. Sinsel, Daniel E. Welcome, Christopher Warren, Xueyan S. Xu, Thomas W. McDowell, and John Z. Wu. Review and evaluation of hand-arm coordinate systems for measuring vibration exposure, biodynamic responses, and hand forces. *Safety and Health at Work*, 6(3):159–173, 2015.

[8] Rolf Eppinger, Emily Sun, Faris Bandak, Mark Haffner, Nopporn Khaewpong, Matt Maltese, Shashi Kuppa, Thuvan Nguyen, Erik Takhounts, Rabih Tannous, Anna Zhang, and Roger Saul. Development of Improved Injury Criteria for the Assessment of Advanced Automotive Restraint Systems - II By. Technical Report November, 1999.

[9] M Färkkilä, I Pyykkö, O Korhonen, and J Starck. Hand grip forces during chain saw operation and vibration white finger in lumberjacks. *British journal of industrial medicine*, 36(4):336–341, 1979.

[10] Shuai Guo, Song Liang Nie, Feng Feng Xi, and Tao Song. Modeling and simulation of percussive impact for robotic riveting system. *Advances in Manufacturing*, 2(4):344–352, 2014.

[11] Joe Haley. Anthropometry and mass distribution for human analogues. volume 1. military male aviators. *Aerospace Medical Research Lab Wright-Patterson*, (88):33–38, 1988.

[12] Hans Wolfgang Henn. Crash Tests and the Head Injury Criterion. *Teaching Mathematics and its Applications*, 17(4):162–170, 1998.

[13] Harpur Hill, Paul Pitts, and Paul Pitts. Hand-arm vibration emission of chainsaws comparison with vibration exposure. Technical report, Health and Safety Laboratory, Derbyshire, 2004.

[14] Thomas W. McDowell, Christopher Warren, Xueyan S. Xu, Daniel E. Welcome, and Ren G. Dong. Laboratory and workplace assessments of rivet bucking bar vibration emissions. *Annals of Occupational Hygiene*, 59(3):382–397, 2015.

[15] Becky Mueller, Anna MacAlister, Joe Nolan, and David Zuby. Comparison of HIC and BrIC Head Injury Risk in IIHS Frontal Crash Tests to Real-world Head Injuries. *Enhanced Safety Vehicle (ESV)*, pages 1–18, 2015.

[16] K T Palmer, M J Griffin, H E Syddall, B Pannett, C Cooper, and D Coggon. Raynaud's phenomenon, vibration induced white finger, and difficulties in hearing. *Occupational and environmental medicine*, 59:640–642, 2002.

[17] Sandya Govinda Raju, Olaf Rogness, Magnus Persson, James Bain, and Danny Riley. Vibration from a riveting hammer causes severe nerve damage in the rat tail model. *Muscle and Nerve*, 44(5):795–804, 2011.

[18] Calvin Rans, Paul V. Straznicky, and René Alderliesten. Riveting Process Induced Residual Stresses Around Solid Rivets in Mechanical Joints. *Journal of Aircraft*, 44(1):323–329, 2007.

[19] Jae Rho, Richard Ashmen, and Charles Turner. Young's modulus of trabecular and cortical bone material: Ultrasonic and microtensile measurements. *Journal of Biomechanics*, 26(2):111–119, 1993.

[20] Danny A Riley and Cell Biology. Understanding and Lowering the Risk of Hand-Arm Vibration Syndrome (HAVS) 2014 Indiana Safety & Health Conference & Expo Neuromuscular cell biologist examining how tissues respond to the environmental stresses of gravity and vibration. pages 1–18, 2014.

[21] Erin Witalison, Paul Thompson, and Lorne Hofseth. Frequency-dependent Effects of Vibration on Physiological Systems: Experiments with Animals and other Human Surrogates. *Industrial*, 50(5):343–353, 2015.

[22] Ye Xiong, Asim Mahmood, and Michael Chopp. Animal models of traumatic brain injury. *Nature Reviews Neuroscience*, 14(2):128–142, 2014.

Appendix A

INTERFERENCE BOLT RESULTS
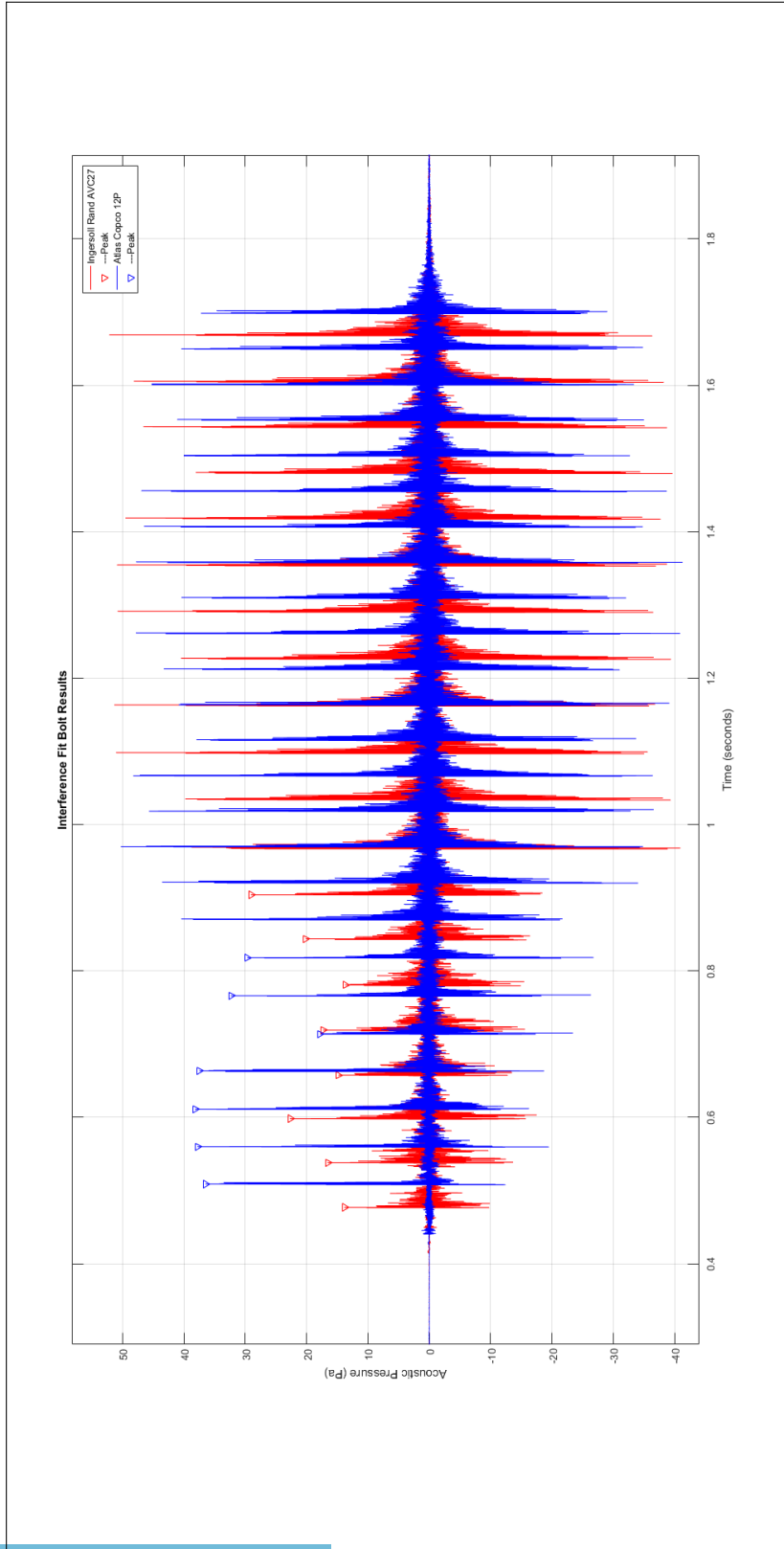
Figure A.1: An example of the acoustic pressure profile for the AVC27 (red), and 12P (blue). The del, ∇, indicate the peaks of interest that correlate for the first strike to the final strike that fully seats the bolt from Fig. 6.1. Additionally, the magnitude of the acoustic pressure is seen to increase when the bolt can no longer be displaced, which is equivalent to striking a hardstop or rigid plate.
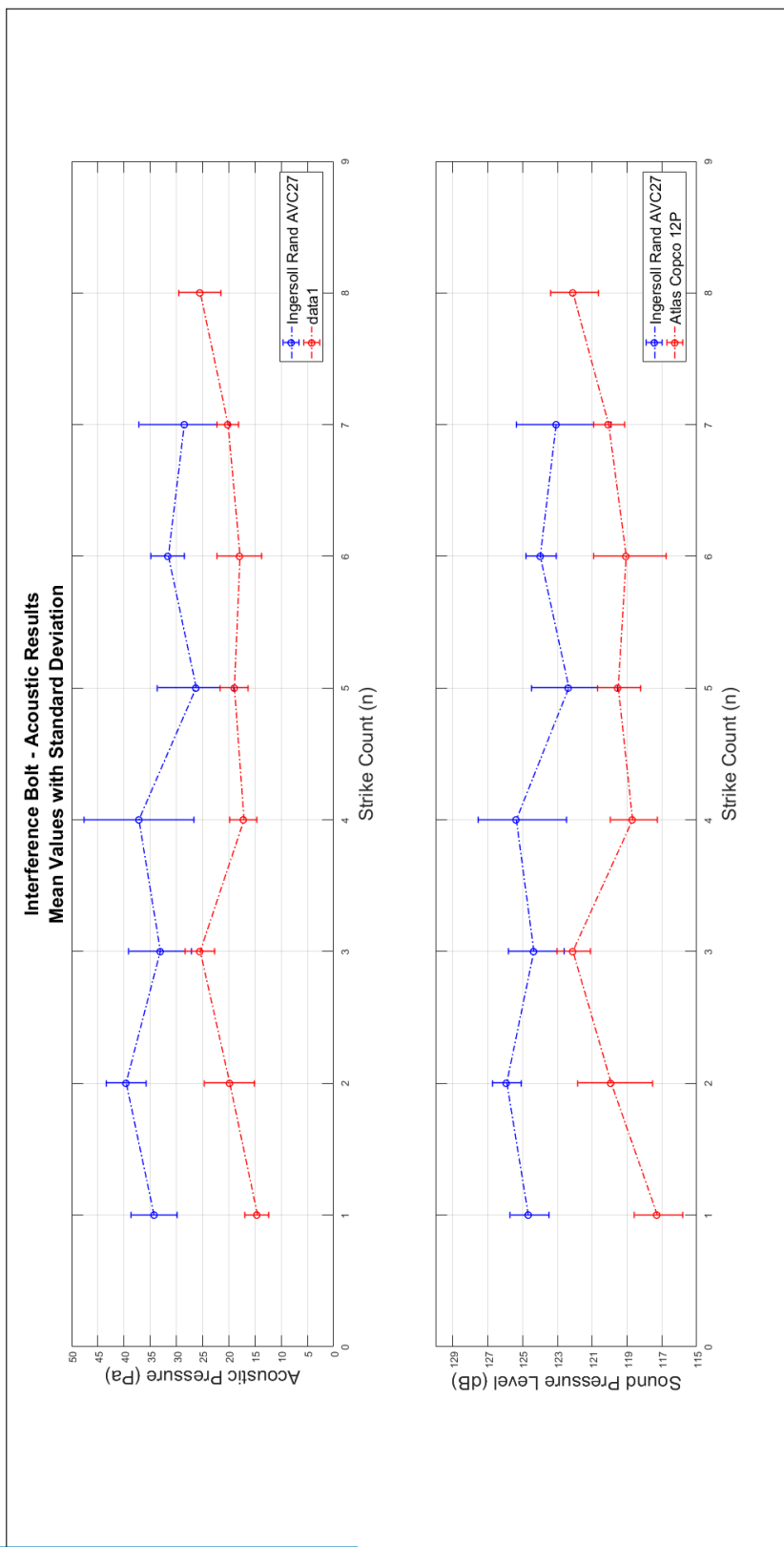
Figure A.2: Displays the marked peak acoustic pressure values from Appendix A.1 for both pneumatic hammers (top), and the converted plot to decibels (bottom), for $n = 4$. The average noise exposure duration for the AVC27 was 0.43 s, and 0.31 s for the 12P. Based on OSHA guidelines, the daily exposure limit for 124 dB is 3 s, and for 120 dB is 9 s, without any noise reduction rating (NRR) hearing protection. The dashed-lines do not indicate the actual magnitude taking place between strikes, but is in place to provide visual guidance on the sequence of strikes.
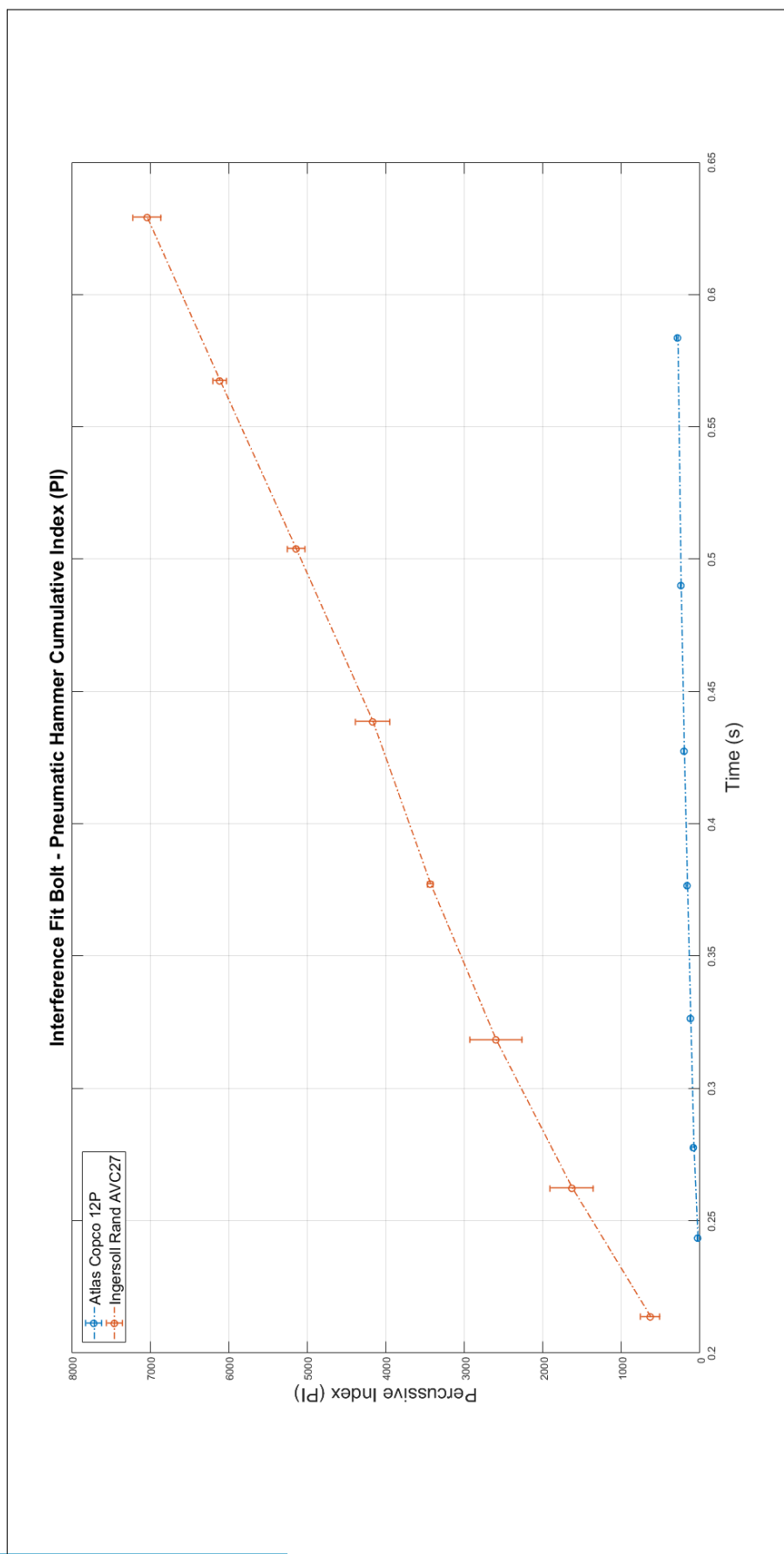
Figure A.3: Plots the averaged index points for the Atlas Copco 12P (dashed-line) against the Ingersoll Rand AVC27 (solid-line) with respect to time for $n = 4$.
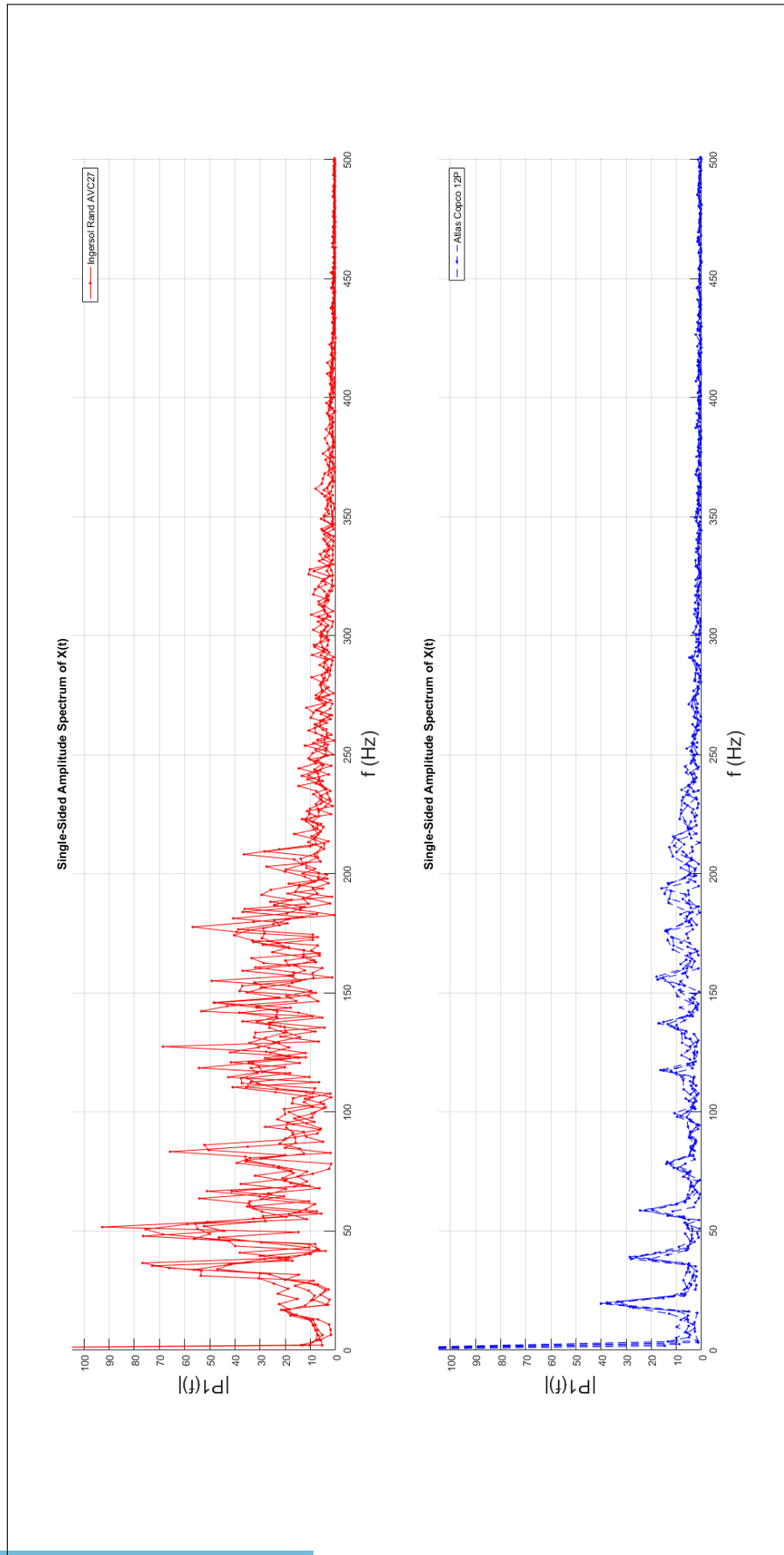
Figure A.4: Displays the single-sided amplitude spectrum of the Ingersoll Rand AVC27 (top) and the Atlas Copco 12P (bottom) based on their respective reaction force, F_R, for $n = 4$. Note, the driving frequency for the 12P is $\approx 20\ Hz$, and is followed by the harmonic resonances at $f + 20\ Hz$

52

Interference-Fit Bolt Results - Ingersoll Rand AVC 27

Run 1

n_R	x (mm)	x_R (mm)	x Time (s)	F_R (N)	F_R Time (s)	P_m (Pa)	P_m Time (s)	P_1 (kPa)	P_2 (kPa)	ΔP (kPa)
1	5.99	5.99	0.49	820.40	0.49	12.59	0.46	792.30	714.01	78.28
2	10.30	4.31	0.54	1152.51	0.54	15.30	0.52	747.66	698.26	49.40
3	13.45	3.14	0.60	1238.16	0.60	24.01	0.58	734.40	688.04	46.36
4	16.22	2.77	0.66	964.82	0.66	15.57	0.65	730.68	685.28	45.40
5	18.45	2.24	0.72	870.88	0.72	16.53	0.71	725.15	682.52	42.63
6	20.64	2.19	0.79	1186.64	0.79	15.05	0.78	723.10	680.49	42.61
7	22.91	2.27	0.86	1117.48	0.85	17.36	0.84	722.33	677.80	44.52
8	24.56	1.64	0.91	999.70	0.91	25.58	0.90	720.43	678.02	42.41
$\bar{x}_R$ (mm)		Duration (s)		$\bar{F}_R$ (N)	Impulse (N·s)	$\bar{P}_m$ (Pa)	$Interval_1$ (Hz)	$\bar{P}_1$ (kPa)	$\bar{P}_2$ (kPa)	$\Delta\bar{P}$ (kPa)
3.07		0.45		1043.82	138.49	17.75	16.11	737.00	688.05	48.95

Run 2

n_R	x (mm)	x_R (mm)	x Time (s)	F_R (N)	F_R Time (s)	P_m (Pa)	P_m Time (s)	P_1 (kPa)	P_2 (kPa)	ΔP (kPa)
1	6.08	6.08	0.54	733.57	0.54	14.24	0.52	791.80	728.56	63.24
2	10.30	4.23	0.59	1159.85	0.59	25.59	0.57	759.81	709.17	50.64
3	13.72	3.42	0.65	1120.44	0.65	26.34	0.63	742.54	695.19	47.35
4	16.37	2.65	0.71	950.12	0.71	20.66	0.69	733.64	689.28	44.36
5	18.38	2.01	0.77	766.93	0.77	19.61	0.75	728.81	685.35	43.46
6	20.42	2.05	0.84	1004.26	0.84	22.43	0.83	726.11	682.38	43.74
7	22.52	2.10	0.90	1087.13	0.90	21.26	0.89	724.96	680.75	44.21
8	24.17	1.65	0.96	978.16	0.96	19.91	0.95	723.36	679.92	43.44
$\bar{x}_R$ (mm)		Duration (s)		$\bar{F}_R$ (N)	Impulse (N·s)	$\bar{P}_m$ (Pa)	$Interval_2$ (Hz)	$\bar{P}_1$ (kPa)	$\bar{P}_2$ (kPa)	$\Delta\bar{P}$ (kPa)
3.02		0.44		975.06	136.79	21.25	16.28	741.38	693.83	47.55

Table A.1: Displays the summary data sheet for the first and second run of the Ingersoll Rand AVC27. The parameters definitions are found in section 5.1.

Interference-Fit Bolt Results – Ingersoll Rand AVC 27

Run 3

n_R	x (mm)	x_R (mm)	x Time (s)	F_R (N)	F_R Time (s)	P_m (Pa)	P_m Time (s)	P_1 (kPa)	P_2 (kPa)	ΔP (kPa)
1	5.75	5.75	0.50	919.93	0.50	13.85	0.48	780.65	705.34	75.32
2	10.10	4.35	0.56	898.24	0.56	16.59	0.54	735.57	687.04	48.53
3	13.27	3.18	0.62	1123.81	0.61	22.71	0.60	723.44	679.05	44.39
4	16.08	2.80	0.68	1108.86	0.67	14.80	0.66	719.54	675.68	43.86
5	18.49	2.41	0.74	1129.63	0.73	17.31	0.72	715.15	671.37	43.77
6	20.81	2.32	0.80	1148.57	0.79	13.72	0.78	713.16	670.56	42.60
7	23.20	2.39	0.86	1156.81	0.86	20.13	0.84	711.70	668.01	43.68
8	25.01	1.81	0.92	1070.96	0.92	29.07	0.90	710.45	667.24	43.22

	$\bar{x}_R$ (mm)		Duration (s)	$\bar{F}_R$ (N)	Impulse (N-s)	$\bar{P}_m$ (Pa)	Interval$_2$ (Hz)	$\bar{P}_1$ (kPa)	$\bar{P}_2$ (kPa)	$\Delta\bar{P}$ (kPa)
	3.13		0.44	1069.60	115.65	18.52	16.67	726.21	678.04	48.17

Run 4

n_R	x (mm)	x_R (mm)	x Time (s)	F_R (N)	F_R Time (s)	P_m (Pa)	P_m Time (s)	P_1 (kPa)	P_2 (kPa)	ΔP (kPa)
1	5.12	5.12	0.51	814.21	0.51	17.98	0.49	787.68	714.57	73.11
2	9.48	4.37	0.57	937.78	0.57	22.02	0.54	744.39	695.11	49.28
3	13.09	3.60	0.63	1007.38	0.62	29.18	0.60	733.18	686.49	46.69
4	15.86	2.77	0.68	1158.99	0.68	17.94	0.66	727.67	683.90	43.77
5	18.31	2.45	0.74	1191.39	0.74	22.49	0.72	723.92	679.74	44.18
6	20.65	2.34	0.80	1198.86	0.80	20.72	0.79	721.68	677.43	44.25
7	22.89	2.24	0.87	1215.60	0.86	22.12	0.85	720.63	676.42	44.22
8	25.03	2.14	0.93	1291.99	0.93	27.60	0.91	719.48	675.82	43.66

	$\bar{x}_R$ (mm)		Duration (s)	$\bar{F}_R$ (N)	Impulse (N-s)	$\bar{P}_m$ (Pa)	Interval$_1$ (Hz)	$\bar{P}_1$ (kPa)	$\bar{P}_2$ (kPa)	$\Delta\bar{P}$ (kPa)
	3.12		0.44	1102.02	134.26	22.51	16.39	734.83	686.18	48.64

Table A.2: Displays the summary data sheet for the third and fourth run of the Ingersoll Rand AVC27. The parameters definitions are found in section 5.1

Interference-Fit Bolt Results - Atlas Copco 12P

Run 1

n_R	x (mm)	x_R (mm)	x Time (s)	F_R (N)	F_R Time (s)	P_m (Pa)	P_m Time (s)	P_1 (kPa)	P_2 (kPa)	ΔP (kPa)
1	9.16	9.16	0.55	255.76	0.54	36.48	0.51	789.63	684.50	105.13
2	12.37	3.21	0.60	391.25	0.58	37.78	0.56	707.80	672.57	35.23
3	16.14	3.77	0.65	302.40	0.63	38.18	0.61	706.80	662.98	43.82
4	18.10	1.96	0.70	322.37	0.68	37.47	0.66	697.60	657.29	40.31
5	20.85	2.75	0.75	307.54	0.72	17.78	0.71	689.13	652.89	36.25
6	22.62	1.77	0.80	339.07	0.77	32.35	0.77	684.11	649.27	34.84
7	24.54	1.93	0.84	310.74	0.83	29.65	0.82	679.97	644.70	35.27

$\bar{x}_R$ (mm)	Duration (s)	$\bar{F}_R$ (N)	Impulse (N-s)	$\bar{P}_m$ (Pa)	$Interval_1$ (Hz)	$\bar{P}_1$ (kPa)	$\bar{P}_2$ (kPa)	$\Delta\bar{P}$ (kPa)
3.51	0.33	316.42	67.38	32.81	19.40	707.86	660.60	47.26

Run 2

n_R	x (mm)	x_R (mm)	x Time (s)	F_R (N)	F_R Time (s)	P_m (Pa)	P_m Time (s)	P_1 (kPa)	P_2 (kPa)	ΔP (kPa)
1	5.21	5.21	0.50	282.41	0.47	31.72	0.46	786.30	690.27	96.03
2	11.18	5.97	0.55	288.09	0.55	37.62	0.51	711.62	674.04	37.58
3	14.30	3.12	0.60	314.40	0.57	24.47	0.56	678.00	664.19	13.81
4	17.20	2.90	0.65	321.10	0.62	40.08	0.61	698.45	656.19	42.26
5	19.49	2.29	0.70	318.72	0.68	35.50	0.66	689.49	651.58	37.91
6	21.99	2.50	0.77	312.04	0.73	35.67	0.72	682.80	647.66	35.15
7	24.72	2.73	0.81	326.93	0.78	27.74	0.77	678.17	643.64	34.53

$\bar{x}_R$ (mm)	Duration (s)	$\bar{F}_R$ (N)	Impulse (N-s)	$\bar{P}_m$ (Pa)	$Interval_2$ (Hz)	$\bar{P}_1$ (kPa)	$\bar{P}_2$ (kPa)	$\Delta\bar{P}$ (kPa)
3.53	0.31	318.64	64.62	33.26	19.64	703.55	661.08	42.47

Table A.3: Displays the summary data sheet for the first and second run of the Atlas Copco 12P. The parameters definitions are found in section 5.1

Interference-Fit Bolt Results - Atlas Copco 12P

Run 3

n_R	x (mm)	x_R (mm)	x Time (s)	F_R (N)	F_R Time (s)	P_m (Pa)	P_m Time (s)	P_1 (kPa)	P_2 (kPa)	ΔP (kPa)
1	7.70	7.70	0.50	270.52	0.50	39.24	0.46	790.01	693.23	96.78
2	12.11	4.40	0.55	287.84	0.55	45.35	0.51	703.41	678.11	25.30
3	14.38	2.27	0.60	301.11	0.58	35.86	0.57	715.94	671.10	44.84
4	17.58	3.20	0.65	283.60	0.65	48.23	0.62	702.02	662.03	39.98
5	19.29	1.71	0.70	306.90	0.68	24.90	0.67	695.04	659.31	35.73
6	21.91	2.62	0.75	311.91	0.73	28.07	0.72	688.22	653.81	34.41
7	24.13	2.22	0.80	304.60	0.79	38.85	0.77	684.24	650.68	33.56

	$\bar{x}_R$ (mm)		Duration (s)	$\bar{F}_R$ (N)	Impulse (N·s)	$\bar{P}_m$ (Pa)	Interval$_2$ (Hz)	$\bar{P}_1$ (kPa)	$\bar{P}_2$ (kPa)	$\Delta\bar{P}$ (kPa)
	3.45		0.31	301.62	64.40	37.21	19.40	711.27	666.90	44.37

Run 4

n_R	x (mm)	x_R (mm)	x Time (s)	F_R (N)	F_R Time (s)	P_m (Pa)	P_m Time (s)	P_1 (kPa)	P_2 (kPa)	ΔP (kPa)
1	6.19	6.19	0.50	272.63	0.48	29.70	0.46	786.86	689.75	97.12
2	11.38	5.18	0.55	280.50	0.53	37.79	0.51	720.77	674.38	46.39
3	14.79	3.42	0.60	293.52	0.58	33.90	0.56	710.85	664.13	46.72
4	17.58	2.79	0.65	324.49	0.63	22.91	0.62	698.23	656.44	41.78
5	19.91	2.33	0.70	320.03	0.68	27.12	0.67	689.62	651.29	38.33
6	22.34	2.43	0.75	326.65	0.73	30.54	0.72	683.66	647.16	36.50
7	24.56	2.22	0.80	323.96	0.79	17.76	0.77	677.74	643.71	34.03

	$\bar{x}_R$ (mm)		Duration (s)	$\bar{F}_R$ (N)	Impulse (N·s)	$\bar{P}_m$ (Pa)	Interval$_2$ (Hz)	$\bar{P}_1$ (kPa)	$\bar{P}_2$ (kPa)	$\Delta\bar{P}$ (kPa)
	3.51		0.30	317.73	61.58	28.53	19.64	709.68	660.98	48.70

Table A.4: Displays the summary data sheet for the third and fourth run of the Atlas Copco 12P. The parameters definitions are found in section 5.1

Appendix B

PERCUSSIVE RIVETING RESULTS
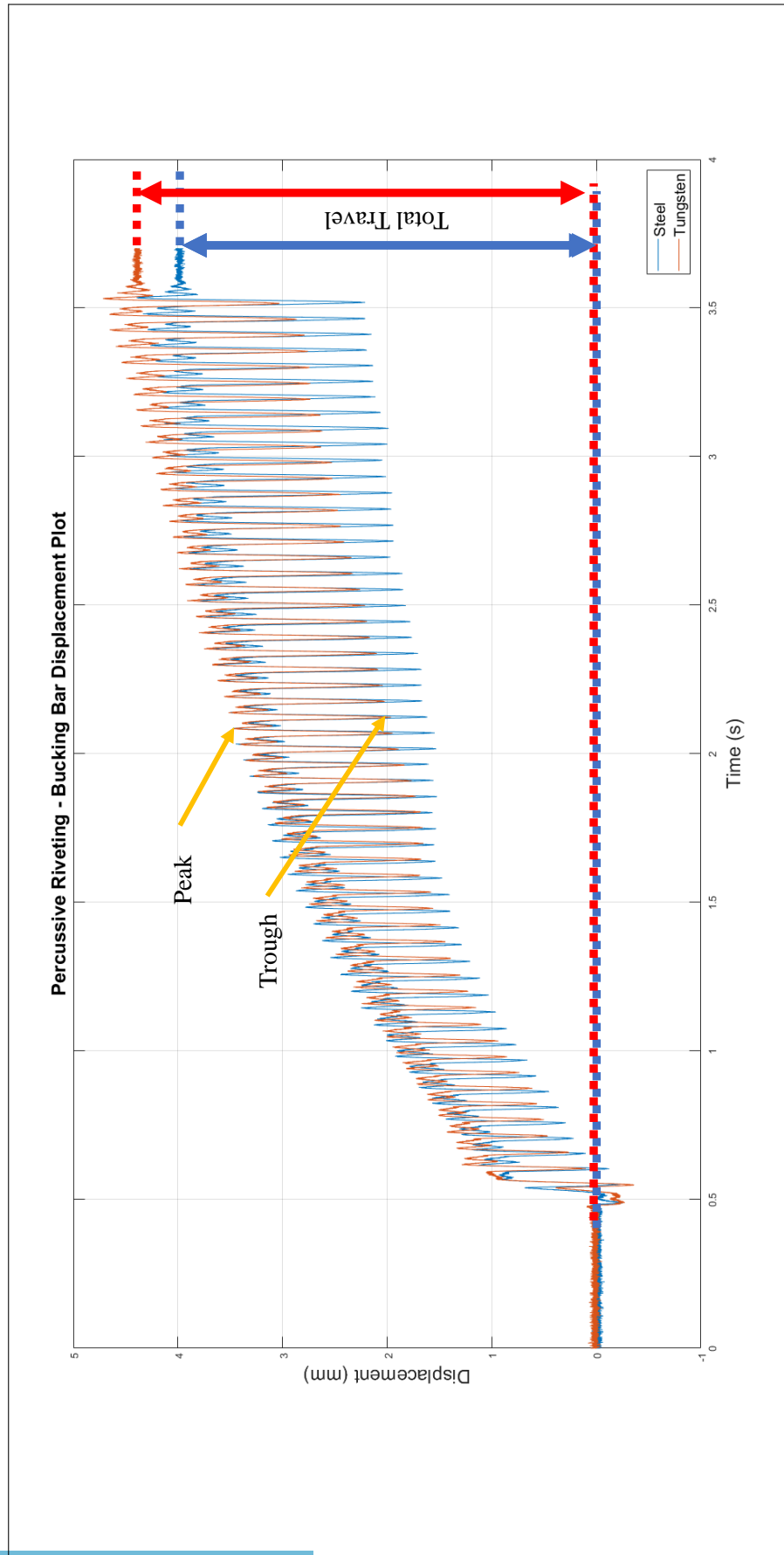
Figure B.1: Diagrams the method for determining peaks and troughs of the laser displacement data. Note the recoil is based on the difference between the peak and its paired trough. Additionally, the total travel distance may not directly equate to the final button height, as this value does not take into account deflection.
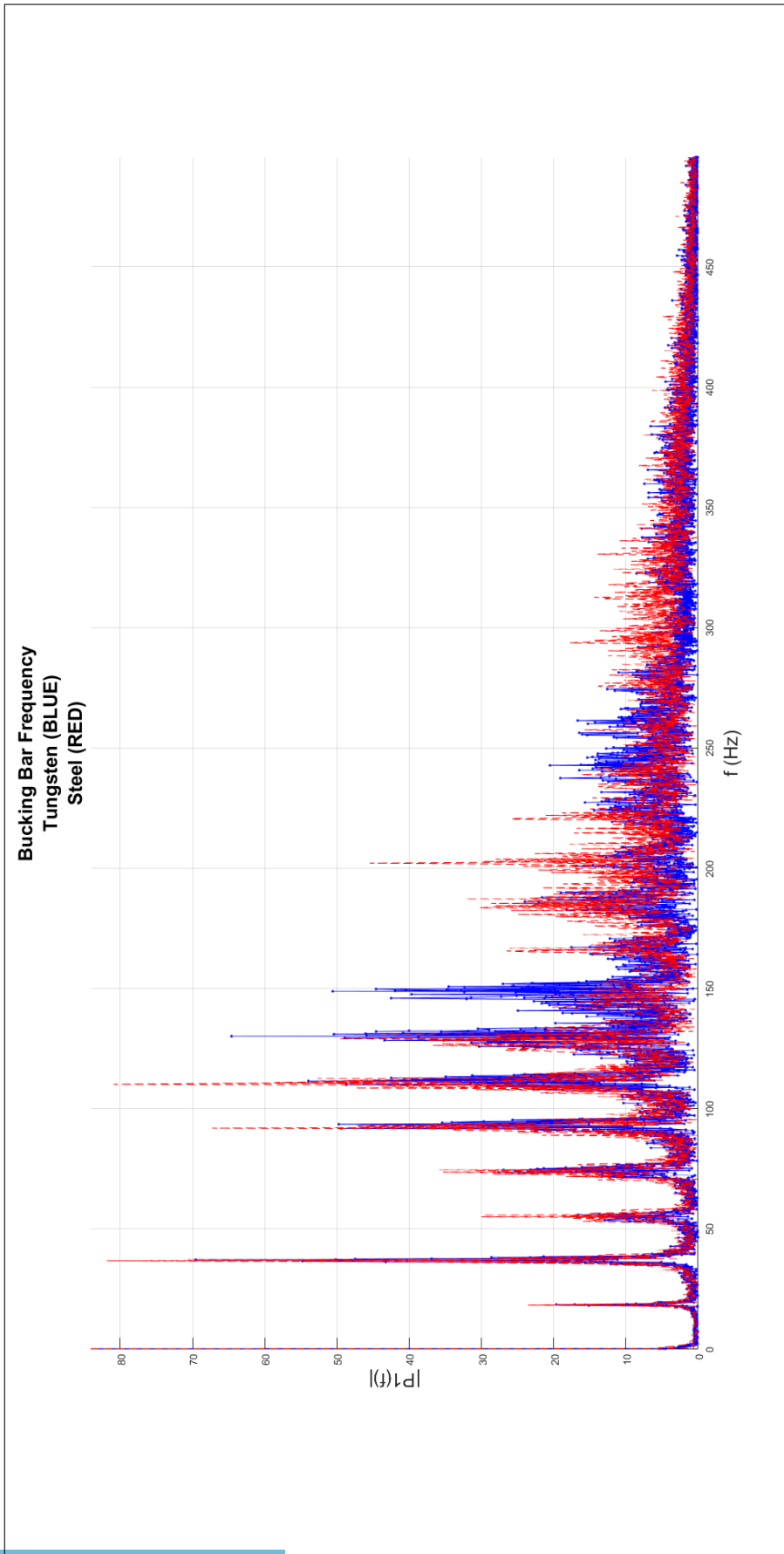
Figure B.2: Displays the single-sided amplitude spectrum of the tungsten bucking bar (blue) and steel bucking bar (red), each of $n = 4$.
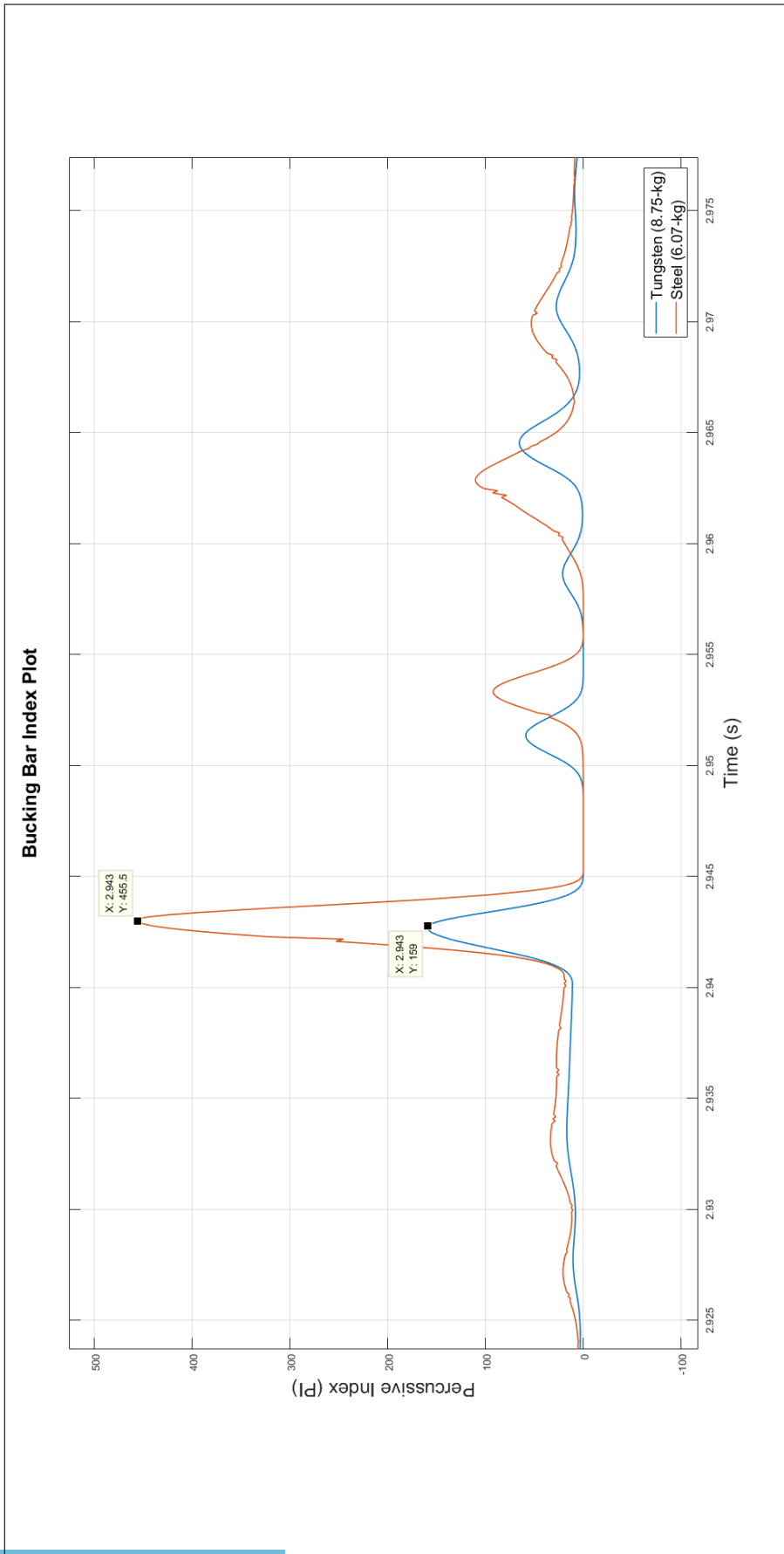
Figure B.3: Illustrates a single Percussive Index generated from applying Eq. 3.1 to the tungsten and steel bucking bar. Each peak value is plotted as a single point on Appendix. B.5.
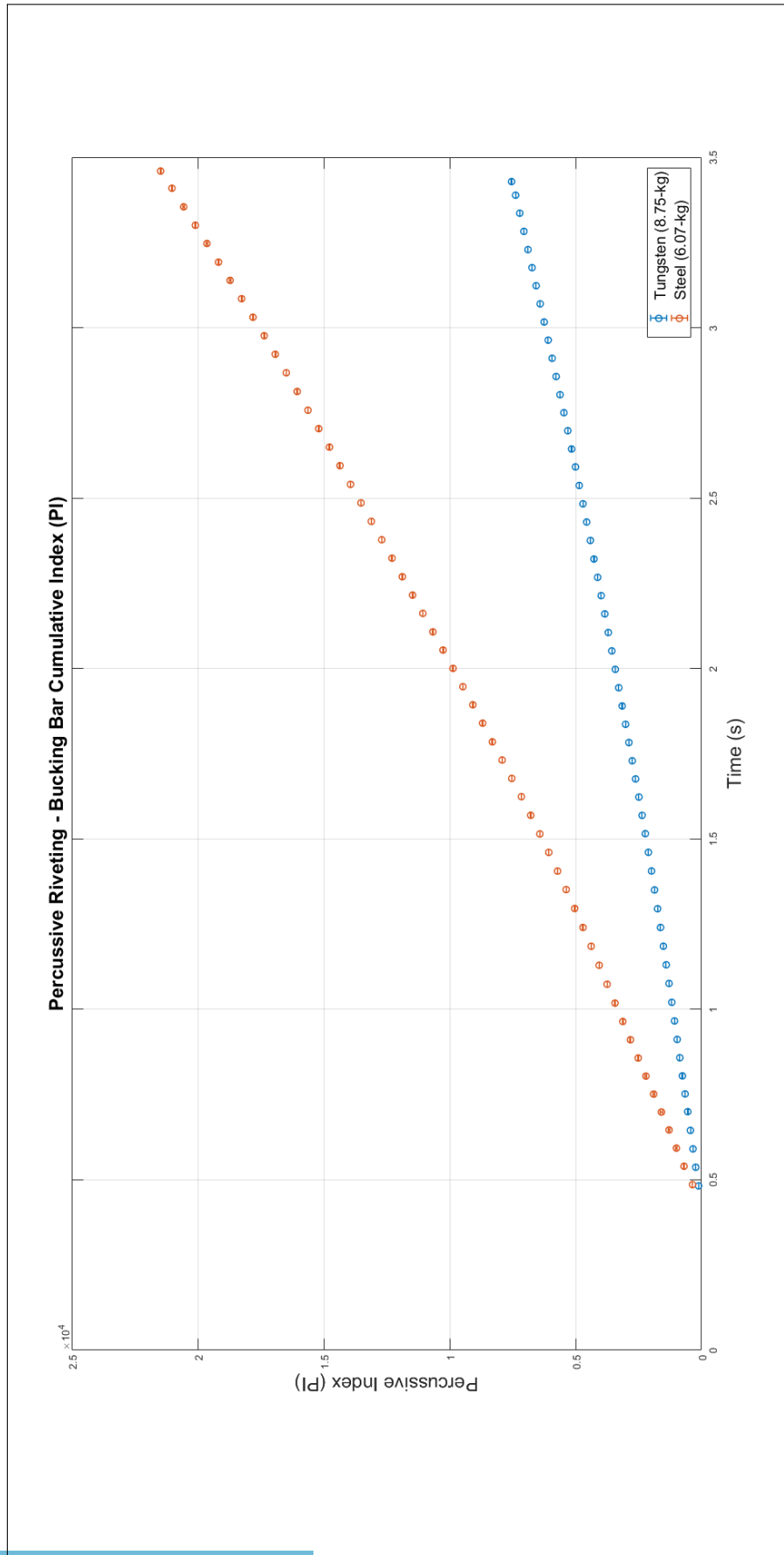
Figure B.4: Presents the plotted averaged index points for the percussive riveting experiment, comparing two bucking bars of different weights, each $n = 4$. The results indicated the tungsten bar at 8.75 kg scored better (lower) than the steel bar weighing in at 6.07 kg.
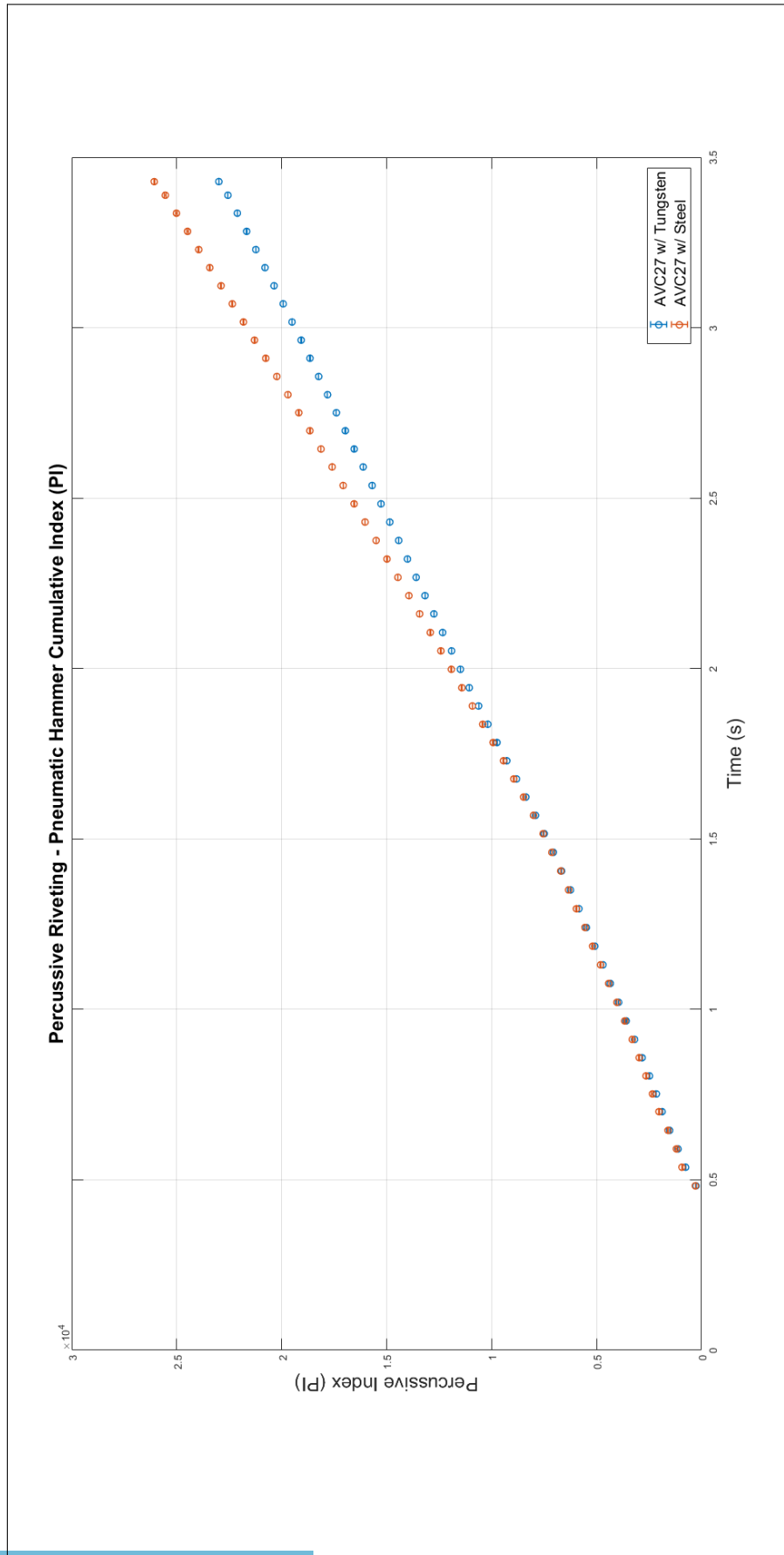
Figure B.5: Presents the plotted averaged index points for the Ingersoll Rand AVC27 used in both the steel and tungsten experiments. Both plots are comparable up to the 1.5 *s* mark and then proceed to diverge, indicating the change in mass on the bucking bar bears some effect on the riveter.

Steel Bucking Bar (6.07-kg)						
	n_R	x Time (s)	x_B (mm)	x_D (mm)	F_B (N)	P_m (Pa)	ΔP (kPa)
	1	0.56	0.28	0.30	784.16	286.75	72.15
	2	0.57	0.97	1.15	1426.88	171.41	33.00
	3	0.62	1.18	1.25	1342.66	184.75	36.57
	4	0.67	1.25	1.09	1218.55	284.25	38.36
	5	0.72	1.35	1.07	1242.24	234.82	36.91
	6	0.77	1.50	1.15	1290.21	258.98	39.13
	7	0.82	1.62	1.21	1294.24	257.59	39.68
	8	0.88	1.75	1.25	1310.00	222.25	38.96
	9	0.93	1.84	1.21	1321.54	217.68	38.36
	10	0.98	1.98	1.26	1324.32	278.87	40.11
	11	1.04	2.07	1.25	1335.44	238.03	40.44
	12	1.09	2.18	1.27	1338.25	279.14	40.79
	13	1.14	2.31	1.29	1363.68	252.27	41.23
	14	1.20	2.40	1.32	1369.37	299.05	41.89
	15	1.26	2.50	1.33	1387.14	249.27	43.08
	16	1.31	2.60	1.34	1387.16	291.63	41.89
	17	1.37	2.68	1.33	1397.89	296.86	41.85
	18	1.43	2.76	1.39	1432.02	278.39	40.69
	19	1.48	2.84	1.39	1417.99	286.54	40.86
	20	1.54	2.93	1.47	1445.38	240.04	40.38
	21	1.60	3.01	1.48	1445.42	271.16	39.71
	22	1.65	3.08	1.49	1473.56	271.58	40.66
	23	1.71	3.15	1.55	1502.56	283.42	40.08
	24	1.76	3.20	1.61	1512.40	278.60	39.28
	25	1.82	3.25	1.63	1529.23	256.98	40.23
	26	1.87	3.30	1.72	1515.75	257.46	40.79
Run 1	27	1.92	3.37	1.76	1539.07	246.39	40.39
	28	1.98	3.43	1.77	1540.25	240.49	40.98
	29	2.03	3.50	1.92	1534.38	281.81	41.10
	30	2.09	3.53	1.93	1533.80	244.19	41.12
	31	2.14	3.56	1.89	1521.95	239.16	40.41
	32	2.19	3.60	1.88	1527.85	241.74	39.85
	33	2.25	3.66	1.93	1519.61	262.27	40.38
	34	2.30	3.68	1.95	1531.17	260.13	41.24
	35	2.35	3.73	1.97	1530.73	296.38	40.81
	36	2.41	3.78	1.96	1529.84	315.15	41.75
	37	2.46	3.81	1.98	1546.39	313.39	39.38
	38	2.51	3.85	1.97	1525.44	279.34	39.34
	39	2.57	3.89	1.99	1538.65	323.90	39.35
	40	2.62	3.95	2.04	1553.27	253.14	42.08
	41	2.68	3.96	1.93	1557.67	256.96	40.50
	42	2.73	4.00	2.01	1549.61	296.43	40.66
	43	2.78	4.03	2.04	1571.09	276.53	40.67
	44	2.84	4.06	2.04	1556.44	269.25	41.14
	45	2.89	4.11	2.10	1562.47	306.12	40.65
	46	2.94	4.12	2.05	1563.15	250.75	40.26
	47	3.00	4.16	2.06	1579.59	248.94	40.50
	48	3.05	4.19	2.14	1593.74	264.71	40.34
	49	3.11	4.18	2.14	1628.76	266.49	39.09
	50	3.16	4.23	2.11	1656.76	289.96	40.49
	51	3.21	4.22	2.05	1655.44	308.53	41.28
	52	3.26	4.26	2.07	1651.60	294.38	40.04
	53	3.32	4.27	2.08	1660.65	253.21	39.84
	54	3.37	4.32	2.07	1663.93	276.07	38.68
	55	3.42	4.35	2.14	1674.32	298.03	40.07
	56	3.47	4.39	2.12	1666.51	264.10	40.41

Table B.1: Displays the parameter values for the first run of the steel bucking bar.

			Steel Bucking Bar (6.07-kg)			
	n_R	x Time (s)	x_B (mm)	x_D (mm)	F_B (N)	P_m (Pa)	ΔP (kPa)
	1	0.53	0.13	0.19	789.86	273.70	74.97
	2	0.54	1.02	1.31	1416.47	149.02	50.82
	3	0.60	1.28	1.47	1395.68	192.68	46.43
	4	0.65	1.33	1.51	1302.44	227.18	41.85
	5	0.70	1.46	1.52	1319.83	274.62	42.76
	6	0.76	1.59	1.72	1436.52	297.73	40.89
	7	0.81	1.66	1.63	1457.18	305.25	41.68
	8	0.86	1.78	1.62	1428.17	257.82	41.05
	9	0.91	1.85	1.58	1401.28	251.12	40.26
	10	0.96	1.94	1.63	1373.53	287.21	40.33
	11	1.02	2.02	1.62	1345.96	277.12	40.76
	12	1.07	2.08	1.56	1346.32	248.02	40.98
	13	1.13	2.16	1.48	1338.33	271.97	41.54
	14	1.18	2.25	1.41	1338.80	241.22	40.83
	15	1.24	2.30	1.38	1339.37	264.59	40.85
	16	1.30	2.40	1.40	1351.17	257.57	41.01
	17	1.35	2.47	1.42	1353.49	262.25	41.91
	18	1.41	2.55	1.39	1361.04	269.24	41.05
	19	1.46	2.65	1.54	1389.67	233.63	40.64
	20	1.52	2.72	1.56	1401.98	257.02	41.72
	21	1.57	2.76	1.62	1413.00	257.98	41.12
	22	1.63	2.84	1.72	1411.53	270.67	41.26
	23	1.68	2.92	1.82	1433.48	253.19	41.19
	24	1.74	2.97	1.84	1480.00	313.14	42.18
	25	1.79	3.02	1.87	1465.93	259.90	41.82
	26	1.84	3.08	1.83	1495.17	257.54	40.94
	27	1.90	3.16	1.90	1467.24	228.78	40.30
	28	1.95	3.19	1.90	1472.46	303.97	40.03
	29	2.01	3.26	1.90	1468.60	236.49	40.10
	30	2.06	3.30	1.89	1471.99	244.08	40.95
	31	2.12	3.35	1.95	1476.62	299.58	41.76
	32	2.17	3.37	1.79	1514.61	235.18	40.66
	33	2.22	3.47	1.99	1482.65	267.66	41.09
	34	2.28	3.47	1.83	1525.19	244.34	40.71
	35	2.33	3.57	1.93	1505.09	277.37	41.70
	36	2.38	3.58	1.89	1535.59	257.95	40.54
	37	2.44	3.67	2.00	1503.93	257.57	40.27
	38	2.49	3.70	1.96	1534.54	282.07	39.97
	39	2.55	3.77	2.03	1500.16	288.86	40.35
	40	2.60	3.78	2.02	1512.75	266.08	40.61
	41	2.66	3.83	2.03	1514.66	303.51	40.70
	42	2.71	3.87	2.04	1509.79	274.97	40.53
	43	2.77	3.92	2.05	1511.62	260.52	40.98
	44	2.82	3.97	2.08	1533.62	289.30	41.50
	45	2.88	3.96	2.00	1550.16	252.45	40.73
	46	2.93	4.04	2.08	1552.00	254.05	41.24
	47	2.99	4.05	2.03	1583.57	287.10	41.36
	48	3.04	4.09	2.05	1549.30	278.07	41.21
	49	3.10	4.12	1.99	1582.75	276.57	41.71
	50	3.15	4.16	2.03	1575.60	280.21	42.19
	51	3.20	4.18	1.98	1600.18	254.91	41.12
	52	3.26	4.22	2.01	1596.10	237.16	41.04
	53	3.31	4.28	2.11	1591.36	199.93	41.03
	54	3.37	4.26	1.96	1594.24	279.34	40.35
	55	3.42	4.31	2.06	1608.18	288.51	40.83
	56	3.47	4.38	2.11	1586.42	292.47	40.56

Run 2

Table B.2: Displays the parameter values for the second run of the steel bucking bar.

	n_R	x Time (s)	x_B (mm)	x_D (mm)	F_B (N)	P_m (Pa)	ΔP (kPa)
			Steel Bucking Bar (6.07-kg)				
	1	0.54	0.12	0.22	837.69	259.20	73.38
	2	0.54	0.98	1.32	1423.08	110.89	49.46
	3	0.60	1.26	1.45	1395.82	200.16	44.91
	4	0.65	1.28	1.50	1311.38	293.21	42.40
	5	0.71	1.37	1.34	1278.23	275.31	43.09
	6	0.76	1.43	1.32	1259.97	278.07	40.98
	7	0.82	1.56	1.37	1280.03	309.15	40.82
	8	0.87	1.62	1.38	1292.38	257.65	41.28
	9	0.92	1.75	1.41	1288.89	319.32	42.49
	10	0.98	1.81	1.39	1301.25	331.53	41.41
	11	1.03	1.92	1.37	1301.27	334.28	42.16
	12	1.09	1.99	1.35	1301.13	271.28	41.65
	13	1.14	2.09	1.40	1324.35	317.13	41.60
	14	1.20	2.19	1.39	1330.62	336.73	42.12
	15	1.26	2.25	1.35	1332.28	335.02	42.52
	16	1.31	2.33	1.39	1349.24	243.80	41.77
	17	1.37	2.41	1.45	1379.97	327.98	41.68
	18	1.42	2.48	1.54	1385.58	293.41	41.63
	19	1.48	2.54	1.59	1393.27	330.83	41.61
	20	1.53	2.60	1.62	1406.38	240.61	40.96
	21	1.58	2.68	1.69	1434.45	247.80	40.45
	22	1.64	2.73	1.69	1431.33	260.92	40.18
	23	1.69	2.83	1.77	1444.57	299.59	41.05
	24	1.75	2.89	1.79	1462.49	252.86	41.18
	25	1.80	2.94	1.79	1469.26	282.95	41.81
	26	1.85	2.98	1.80	1465.74	252.44	40.42
Run 3	27	1.91	3.05	1.83	1463.60	282.73	41.63
	28	1.96	3.10	1.84	1467.11	300.45	41.37
	29	2.02	3.13	1.78	1486.34	271.07	41.26
	30	2.07	3.21	1.84	1483.95	257.10	41.44
	31	2.12	3.26	1.87	1474.42	269.63	40.69
	32	2.18	3.31	1.84	1476.18	302.10	40.01
	33	2.23	3.36	1.86	1477.06	288.81	40.72
	34	2.29	3.40	1.88	1494.32	270.39	41.36
	35	2.34	3.45	1.90	1489.75	271.83	40.72
	36	2.40	3.51	1.91	1495.03	299.79	41.81
	37	2.45	3.55	1.91	1504.46	286.02	40.99
	38	2.51	3.60	1.93	1500.18	280.43	41.94
	39	2.56	3.64	1.93	1504.43	302.00	42.68
	40	2.62	3.69	1.90	1508.39	281.77	41.62
	41	2.67	3.71	1.90	1505.94	279.34	40.82
	42	2.72	3.76	1.93	1506.98	270.52	41.75
	43	2.78	3.79	1.91	1520.46	304.48	40.51
	44	2.83	3.85	1.93	1520.23	274.21	41.00
	45	2.89	3.88	1.97	1514.93	295.55	41.16
	46	2.94	3.91	1.93	1543.37	310.32	41.06
	47	3.00	3.93	1.87	1523.32	319.37	40.65
	48	3.05	3.99	1.98	1524.50	315.47	40.38
	49	3.10	4.00	1.93	1546.48	273.19	41.88
	50	3.16	4.08	2.02	1537.95	291.04	41.34
	51	3.21	4.10	2.01	1540.40	275.33	41.88
	52	3.27	4.12	1.99	1561.06	274.03	41.47
	53	3.32	4.20	2.09	1550.40	278.93	41.76
	54	3.38	4.22	2.11	1534.68	302.97	41.77
	55	3.44	4.26	2.13	1542.52	277.22	41.40
	56	3.49	4.31	2.18	1553.61	279.03	41.53

Table B.3: Displays the parameter values for the third run of the steel bucking bar.

Steel Bucking Bar (6.07-kg)						
n_R	*x Time (s)*	x_B *(mm)*	x_D *(mm)*	F_B *(N)*	P_m *(Pa)*	ΔP *(kPa)*
1	0.54	0.63	0.70	834.36	296.81	73.50
2	0.55	1.17	1.42	1427.15	155.47	48.77
3	0.60	1.51	1.44	1409.34	175.88	45.87
4	0.66	1.53	1.59	1411.36	225.14	43.75
5	0.71	1.53	1.46	1331.63	256.38	41.92
6	0.77	1.60	1.31	1279.42	299.30	41.62
7	0.82	1.69	1.27	1271.32	240.98	41.37
8	0.87	1.80	1.31	1279.53	327.43	41.84
9	0.93	1.88	1.28	1296.38	278.97	40.96
10	0.98	1.98	1.34	1310.77	280.35	41.07
11	1.03	2.07	1.38	1324.89	328.49	41.60
12	1.08	2.16	1.42	1328.34	270.08	39.98
13	1.14	2.25	1.42	1343.35	245.45	41.26
14	1.19	2.34	1.43	1349.39	239.88	40.17
15	1.25	2.42	1.41	1340.32	280.04	41.17
16	1.30	2.49	1.46	1380.45	217.79	41.96
17	1.35	2.60	1.49	1371.53	324.14	41.38
18	1.41	2.67	1.50	1384.40	252.47	41.78
19	1.46	2.74	1.57	1405.92	345.35	41.17
20	1.52	2.79	1.56	1411.62	215.22	41.80
21	1.57	2.85	1.62	1420.33	333.46	40.32
22	1.63	2.95	1.67	1424.52	248.60	40.43
23	1.68	3.01	1.72	1425.45	259.00	41.01
24	1.73	3.04	1.68	1452.55	322.34	41.48
25	1.79	3.11	1.73	1451.77	311.82	40.93
26	1.84	3.15	1.71	1472.21	316.56	41.06
27	1.89	3.25	1.79	1447.77	302.16	41.44
28	1.95	3.26	1.76	1473.71	327.50	40.49
29	2.00	3.32	1.78	1491.88	313.60	40.02
30	2.05	3.39	1.74	1494.16	309.94	40.67
31	2.11	3.43	1.76	1512.17	312.69	40.11
32	2.16	3.50	1.83	1500.64	313.58	40.70
33	2.21	3.56	1.89	1523.11	232.89	40.42
34	2.27	3.60	1.92	1526.97	280.86	40.96
35	2.32	3.61	1.85	1544.98	271.47	40.47
36	2.37	3.67	1.91	1528.84	271.45	39.72
37	2.43	3.75	1.97	1523.30	233.19	41.70
38	2.48	3.74	1.81	1533.27	258.13	40.98
39	2.54	3.78	1.85	1539.40	248.98	41.04
40	2.59	3.87	1.99	1547.76	267.04	41.03
41	2.65	3.89	2.00	1550.25	264.55	40.47
42	2.70	3.90	1.92	1576.81	237.20	40.99
43	2.75	3.98	1.99	1561.12	249.24	40.43
44	2.81	3.97	1.91	1589.16	296.83	40.26
45	2.86	4.06	2.07	1575.62	280.49	40.00
46	2.92	4.09	2.08	1571.37	291.61	40.19
47	2.97	4.13	2.05	1579.83	279.64	41.42
48	3.02	4.14	2.01	1604.86	293.31	40.60
49	3.08	4.19	2.11	1582.70	287.56	40.23
50	3.14	4.22	2.12	1592.76	282.05	39.67
51	3.19	4.29	2.13	1610.27	251.34	40.91
52	3.24	4.23	1.96	1617.60	285.70	40.86
53	3.30	4.30	2.12	1620.33	315.57	40.39
54	3.35	4.34	2.05	1627.99	310.49	40.08
55	3.41	4.35	2.06	1623.61	235.59	40.83
56	3.46	4.40	2.13	1618.12	227.51	39.68

Run 4 (row label spanning the left side of the table)

Table B.4: Displays the parameter values for the fourth run of the steel bucking bar.

	n_R	x Time (s)	x_B (mm)	x_D (mm)	F_B (N)	P_m (Pa)	ΔP (kPa)
			Tungsten Bucking Bar (8.75-kg)				
	1	0.54	0.50	0.57	693.86	235.96	74.83
	2	0.54	1.13	1.33	1101.73	164.26	48.10
	3	0.61	1.44	1.19	1099.78	166.82	44.17
	4	0.66	1.49	1.08	1066.55	262.28	42.90
	5	0.71	1.59	0.97	1033.27	237.74	42.09
	6	0.77	1.67	1.01	1072.64	216.56	41.03
	7	0.82	1.77	1.05	1059.03	252.13	41.48
	8	0.87	1.88	1.11	1064.97	284.33	41.03
	9	0.93	1.98	1.08	1049.88	297.01	40.23
	10	0.98	2.07	1.06	1047.23	233.56	40.52
	11	1.03	2.16	1.07	1060.72	265.42	40.17
	12	1.09	2.28	1.02	1091.13	292.28	41.51
	13	1.15	2.40	1.09	1108.71	276.52	40.58
	14	1.20	2.48	1.10	1104.53	268.64	40.21
	15	1.26	2.54	1.08	1101.79	284.67	39.83
	16	1.31	2.65	1.10	1135.06	285.34	40.31
	17	1.37	2.74	1.14	1147.33	265.20	40.42
	18	1.42	2.84	1.19	1149.60	274.79	41.05
	19	1.48	2.90	1.19	1166.60	244.66	40.19
	20	1.54	2.98	1.24	1159.54	254.15	40.34
	21	1.59	3.04	1.20	1166.59	296.75	40.77
	22	1.65	3.10	1.27	1171.85	306.29	42.01
	23	1.70	3.17	1.36	1185.98	297.84	40.74
	24	1.75	3.23	1.41	1191.04	241.10	40.57
	25	1.80	3.31	1.47	1200.24	293.10	39.73
	26	1.86	3.39	1.51	1207.01	297.29	40.15
Run 1	27	1.91	3.43	1.51	1214.11	245.17	39.58
	28	1.96	3.51	1.52	1211.55	258.90	40.33
	29	2.02	3.56	1.52	1210.39	291.86	41.01
	30	2.07	3.62	1.52	1218.22	284.48	40.34
	31	2.12	3.67	1.55	1222.11	257.51	40.30
	32	2.18	3.71	1.54	1227.35	276.95	40.19
	33	2.23	3.78	1.58	1231.21	248.43	39.77
	34	2.28	3.83	1.58	1242.78	245.68	40.60
	35	2.34	3.91	1.65	1248.57	244.04	40.62
	36	2.39	3.96	1.63	1251.14	249.33	40.94
	37	2.45	3.98	1.63	1258.65	250.29	41.24
	38	2.50	4.07	1.70	1257.51	247.86	40.77
	39	2.55	4.09	1.67	1265.70	257.26	40.19
	40	2.61	4.15	1.66	1272.88	261.07	39.61
	41	2.66	4.17	1.67	1272.18	270.11	40.69
	42	2.71	4.20	1.64	1292.47	242.13	39.84
	43	2.77	4.24	1.64	1294.63	249.42	40.88
	44	2.82	4.30	1.67	1304.75	271.98	40.37
	45	2.87	4.32	1.72	1298.47	277.15	40.24
	46	2.93	4.36	1.68	1305.94	265.74	39.31
	47	2.98	4.40	1.72	1307.07	258.16	40.65
	48	3.03	4.47	1.68	1334.01	270.21	40.31
	49	3.09	4.51	1.74	1326.27	237.55	41.28
	50	3.14	4.56	1.76	1318.32	280.43	40.33
	51	3.19	4.58	1.69	1331.40	258.26	40.44
	52	3.25	4.65	1.76	1333.38	252.60	40.40
	53	3.30	4.70	1.80	1336.79	241.55	39.63
	54	3.35	4.75	1.84	1329.69	249.98	40.23
	55	3.41	4.81	1.86	1332.53	278.42	40.88
	56	3.46	4.81	1.79	1347.04	289.04	41.40

Table B.5: Displays the parameter values for the first run of the tungsten bucking bar.

	Tungsten Bucking Bar (8.75-kg)					
n_R	**x Time (s)**	**x_B (mm)**	**x_D (mm)**	**F_B (N)**	**P_m (Pa)**	**ΔP (kPa)**
1	0.53	0.53	0.64	753.85	257.70	73.85
2	0.54	1.14	0.85	1136.94	187.52	49.53
3	0.59	1.46	1.20	1111.87	177.41	46.71
4	0.65	1.49	1.14	1089.72	228.21	42.99
5	0.70	1.56	1.26	1069.28	290.71	43.25
6	0.76	1.71	1.40	1139.55	307.79	43.18
7	0.81	1.82	1.38	1139.57	305.72	41.17
8	0.86	1.90	1.33	1126.82	283.41	40.58
9	0.92	1.99	1.23	1091.60	270.41	40.46
10	0.97	2.08	1.22	1085.40	261.70	41.50
11	1.03	2.14	1.19	1084.60	260.80	41.85
12	1.08	2.19	1.09	1093.13	236.86	40.91
13	1.14	2.32	1.20	1081.12	253.09	41.14
14	1.19	2.39	1.11	1099.61	273.75	41.26
15	1.25	2.48	1.16	1104.07	236.71	41.71
16	1.31	2.55	1.12	1111.93	249.69	41.27
17	1.36	2.65	1.17	1126.26	247.37	40.74
18	1.42	2.73	1.17	1141.00	293.66	41.52
19	1.48	2.82	1.21	1145.52	295.54	40.40
20	1.53	2.89	1.35	1152.24	264.94	40.84
21	1.59	2.95	1.37	1167.47	287.59	40.86
22	1.64	3.03	1.46	1161.81	266.96	41.03
23	1.69	3.10	1.45	1173.10	289.74	40.67
24	1.75	3.19	1.49	1205.89	256.47	40.99
25	1.80	3.24	1.52	1208.72	289.97	40.86
26	1.86	3.30	1.53	1178.50	284.28	41.72
27	1.91	3.37	1.53	1181.86	252.51	40.89
28	1.96	3.44	1.55	1188.80	238.87	41.27
29	2.02	3.51	1.55	1201.27	271.74	40.37
30	2.07	3.56	1.56	1192.04	241.44	40.78
31	2.13	3.62	1.57	1221.69	254.01	40.39
32	2.18	3.67	1.60	1223.67	309.22	40.86
33	2.24	3.73	1.61	1215.01	304.50	40.63
34	2.29	3.80	1.64	1229.56	289.83	41.54
35	2.35	3.84	1.61	1240.10	226.40	40.60
36	2.40	3.90	1.64	1238.96	285.44	41.79
37	2.46	3.95	1.66	1242.32	280.06	41.03
38	2.51	4.01	1.54	1250.46	231.92	42.08
39	2.57	4.06	1.68	1266.49	261.37	40.49
40	2.62	4.12	1.72	1245.42	253.56	40.59
41	2.68	4.17	1.59	1260.01	225.16	42.55
42	2.73	4.18	1.69	1274.53	313.31	40.25
43	2.78	4.27	1.66	1254.39	220.73	40.62
44	2.84	4.27	1.58	1279.85	251.67	39.68
45	2.89	4.33	1.70	1281.05	235.95	40.26
46	2.95	4.41	1.80	1275.38	292.62	40.51
47	3.00	4.45	1.74	1291.28	251.56	40.85
48	3.05	4.49	1.80	1303.82	282.70	41.15
49	3.11	4.53	1.64	1290.70	239.87	41.07
50	3.16	4.56	1.74	1288.47	301.78	41.11
51	3.22	4.64	1.79	1306.26	245.11	40.58
52	3.27	4.68	1.59	1315.82	249.90	41.55
53	3.32	4.70	1.80	1290.44	231.55	39.86
54	3.38	4.78	1.79	1299.71	300.33	39.90
55	3.43	4.80	1.72	1326.01	282.67	40.79
56	3.48	4.82	1.63	1316.83	225.23	37.24

Note: "Run 2" label appears vertically along the left side of the table.

Table B.6: Displays the parameter values for the second run of the tungsten bucking bar.

	n_R	x Time (s)	x_B (mm)	x_D (mm)	F_B (N)	P_m (Pa)	ΔP (kPa)
				Tungsten Bucking Bar (8.75-kg)			
	1	0.53	0.18	0.22	731.95	303.42	74.13
	2	0.56	1.12	1.25	1140.12	214.20	48.33
	3	0.61	1.41	1.17	1119.47	195.42	44.66
	4	0.66	1.43	1.20	1090.22	272.19	42.00
	5	0.72	1.47	1.13	1047.38	209.45	42.66
	6	0.77	1.56	1.13	1053.10	333.64	42.20
	7	0.83	1.62	1.16	1065.62	327.61	40.98
	8	0.88	1.72	1.18	1063.44	296.62	41.76
	9	0.93	1.81	1.21	1065.59	247.60	40.23
	10	0.99	1.90	1.16	1058.89	336.48	41.33
	11	1.04	1.99	1.14	1070.69	292.63	41.24
	12	1.09	2.06	1.08	1077.75	243.10	41.19
	13	1.15	2.15	1.11	1087.14	274.26	40.52
	14	1.21	2.25	1.10	1109.18	282.60	41.23
	15	1.26	2.35	1.18	1114.59	249.05	40.56
	16	1.31	2.41	1.20	1117.15	282.10	41.85
	17	1.37	2.46	1.26	1122.92	292.41	41.20
	18	1.42	2.54	1.31	1139.96	303.44	41.36
	19	1.48	2.59	1.29	1138.76	302.40	41.18
	20	1.53	2.68	1.32	1146.56	303.58	41.19
	21	1.59	2.77	1.37	1159.05	292.49	40.58
Run 3	22	1.64	2.85	1.48	1182.32	305.90	40.72
	23	1.70	2.90	1.55	1188.43	284.71	40.39
	24	1.75	2.96	1.58	1188.51	294.68	40.82
	25	1.80	3.03	1.56	1198.31	224.24	41.74
	26	1.86	3.13	1.59	1208.96	244.05	41.83
	27	1.91	3.18	1.58	1210.30	279.91	41.11
	28	1.96	3.24	1.61	1222.42	308.65	40.20
	29	2.02	3.31	1.63	1219.94	288.51	40.57
	30	2.07	3.36	1.62	1213.80	239.30	40.06
	31	2.13	3.44	1.67	1226.30	271.35	40.63
	32	2.18	3.50	1.68	1225.50	258.25	40.40
	33	2.23	3.56	1.70	1229.91	296.18	41.17
	34	2.29	3.60	1.58	1251.40	253.17	40.93
	35	2.34	3.66	1.62	1233.35	289.08	40.29
	36	2.39	3.71	1.62	1242.13	252.49	39.90
	37	2.45	3.78	1.71	1240.64	302.41	40.28
	38	2.50	3.85	1.73	1238.68	286.58	40.64
	39	2.55	3.89	1.63	1265.22	252.03	41.26
	40	2.61	3.95	1.73	1245.34	297.21	40.79
	41	2.66	3.98	1.73	1246.33	248.36	41.18
	42	2.71	4.03	1.64	1276.86	298.80	40.16
	43	2.77	4.07	1.62	1278.03	237.19	40.18
	44	2.82	4.11	1.64	1282.68	254.22	39.86
	45	2.87	4.17	1.67	1281.59	289.44	40.51
	46	2.92	4.22	1.69	1278.37	306.87	41.14
	47	2.97	4.26	1.70	1287.63	288.09	40.26
	48	3.03	4.30	1.67	1293.79	229.13	39.95
	49	3.08	4.33	1.65	1296.06	291.57	40.77
	50	3.13	4.39	1.72	1299.50	241.48	41.44
	51	3.18	4.40	1.68	1303.09	288.06	40.22
	52	3.24	4.46	1.76	1311.12	286.01	39.97
	53	3.29	4.48	1.72	1313.24	291.45	39.81
	54	3.34	4.54	1.74	1314.42	296.27	39.90
	55	3.39	4.56	1.71	1316.06	291.21	40.77
	56	3.44	4.58	1.70	1318.57	293.70	40.44

Table B.7: Displays the parameter values for the third run of the tungsten bucking bar.

	n_R	x Time (s)	x_B (mm)	x_D (mm)	F_B (N)	P_m (Pa)	ΔP (kPa)
Tungsten Bucking Bar (8.75-kg)							
	1	0.52	0.22	0.24	733.33	334.69	74.22
	2	0.56	1.08	1.32	1139.27	145.39	49.13
	3	0.61	1.39	1.14	1114.12	191.77	44.99
	4	0.66	1.42	1.21	1103.38	200.60	42.69
	5	0.72	1.47	1.13	1052.35	266.38	42.93
	6	0.77	1.55	1.01	1018.70	253.08	42.21
	7	0.82	1.67	1.10	1035.12	279.02	39.79
	8	0.87	1.78	1.13	1050.74	308.97	40.12
	9	0.93	1.87	1.13	1060.31	227.90	41.68
	10	0.98	1.99	1.20	1064.86	224.87	41.15
	11	1.03	2.07	1.15	1065.92	229.08	40.96
	12	1.09	2.19	1.23	1082.21	242.35	40.32
	13	1.14	2.30	1.21	1077.39	257.18	40.29
	14	1.20	2.36	1.20	1098.52	272.70	40.99
	15	1.25	2.46	1.24	1107.92	322.97	42.38
	16	1.30	2.54	1.23	1111.25	279.00	42.02
	17	1.36	2.62	1.26	1129.87	259.81	41.39
	18	1.41	2.73	1.31	1136.65	297.27	41.23
	19	1.46	2.78	1.24	1125.31	317.92	41.74
	20	1.52	2.85	1.33	1158.71	311.96	41.06
Run 4	21	1.57	2.96	1.32	1144.95	276.06	40.78
	22	1.63	3.02	1.42	1176.08	267.11	40.59
	23	1.68	3.08	1.39	1157.94	344.25	41.36
	24	1.74	3.15	1.46	1188.37	314.77	41.39
	25	1.79	3.23	1.47	1179.45	315.76	41.57
	26	1.84	3.28	1.55	1200.77	283.03	41.16
	27	1.90	3.36	1.58	1206.40	306.97	40.66
	28	1.95	3.41	1.60	1215.17	323.69	39.97
	29	2.00	3.48	1.59	1228.76	269.12	41.08
	30	2.06	3.53	1.62	1235.47	265.32	40.74
	31	2.11	3.59	1.66	1238.58	289.89	41.26
	32	2.17	3.63	1.62	1247.96	263.83	41.23
	33	2.22	3.68	1.65	1236.17	270.71	42.22
	34	2.28	3.73	1.66	1248.27	253.86	40.74
	35	2.33	3.78	1.66	1268.79	275.91	39.96
	36	2.38	3.85	1.72	1269.44	248.00	41.17
	37	2.44	3.93	1.77	1273.79	282.70	40.67
	38	2.49	3.92	1.65	1284.20	279.65	40.86
	39	2.54	4.01	1.78	1278.16	250.18	41.16
	40	2.60	4.03	1.72	1301.49	260.69	41.25
	41	2.65	4.10	1.82	1294.49	290.96	41.16
	42	2.71	4.13	1.67	1301.73	281.95	40.09
	43	2.76	4.18	1.77	1303.54	275.90	39.59
	44	2.81	4.20	1.67	1313.59	264.42	40.86
	45	2.86	4.25	1.73	1305.79	275.08	40.37
	46	2.92	4.29	1.69	1312.60	274.33	41.04
	47	2.97	4.31	1.66	1321.31	285.73	40.09
	48	3.02	4.41	1.87	1311.33	296.05	40.01
	49	3.07	4.41	1.71	1336.46	249.72	40.74
	50	3.12	4.45	1.83	1327.06	286.19	40.57
	51	3.18	4.47	1.76	1337.41	273.96	41.26
	52	3.23	4.50	1.76	1344.02	298.29	40.28
	53	3.28	4.56	1.82	1339.73	293.06	40.08
	54	3.34	4.59	1.82	1345.80	308.80	40.03
	55	3.39	4.61	1.83	1353.76	293.59	40.59
	56	3.44	4.63	1.74	1352.32	288.52	40.22

Table B.8: Displays the parameter values for the fourth run of the tungsten bucking bar.

n_R	Steel Bucking Bar (6.07-kg)				Tungsten Bucking Bar (8.75-kg)			
	1	*2*	*3*	*4*	*1*	*2*	*3*	*4*
1	430.21	476.66	680.00	731.59	392.79	583.29	335.48	351.64
2	878.51	921.50	902.61	888.46	779.84	922.14	894.08	831.96
3	551.17	676.95	677.86	618.84	714.82	729.69	716.91	725.83
4	691.52	767.53	745.50	738.35	702.81	744.46	733.53	750.76
5	688.07	761.64	706.29	764.23	595.22	747.41	733.19	703.31
6	661.36	842.01	738.97	687.28	645.74	808.42	676.93	668.53
7	652.06	823.46	721.14	684.45	697.89	841.49	757.67	670.07
8	673.87	816.76	730.83	685.79	716.83	835.18	753.19	685.25
9	668.13	808.01	720.00	698.88	706.56	821.61	745.41	693.09
10	678.03	816.24	720.71	708.91	699.12	795.91	723.12	748.16
11	675.16	809.09	724.30	713.31	675.08	769.94	692.74	691.74
12	640.03	780.76	726.54	723.02	616.39	766.78	671.99	742.12
13	664.28	744.61	733.42	724.73	615.31	740.74	664.77	678.04
14	653.32	732.60	729.75	723.42	635.06	753.16	661.77	727.65
15	644.72	737.49	730.30	724.22	632.35	701.49	674.23	740.86
16	646.44	740.55	739.28	739.06	637.10	736.55	710.13	697.63
17	642.22	738.29	748.68	727.26	662.98	695.94	760.32	744.81
18	637.78	744.42	758.84	728.93	682.16	692.53	779.11	771.21
19	645.54	750.19	780.37	753.29	703.60	706.70	765.06	733.37
20	627.37	759.01	801.48	755.14	724.51	721.36	761.48	781.98
21	643.49	784.04	835.22	784.74	719.01	824.38	763.24	764.55
22	668.26	819.26	846.21	794.23	743.08	837.53	834.75	791.64
23	685.67	885.34	848.79	793.03	775.17	858.87	851.48	789.34
24	752.90	912.59	854.63	814.90	790.59	856.26	853.03	814.90
25	780.56	919.75	873.37	824.23	798.57	858.11	852.86	820.52
26	818.18	912.92	868.25	827.10	799.09	859.89	859.25	834.48
27	811.94	917.27	867.32	816.37	804.35	863.24	857.41	841.56
28	821.49	924.13	878.68	837.37	805.61	863.62	859.94	852.39
29	906.16	918.02	875.94	845.09	801.44	866.11	861.23	836.82
30	908.21	916.92	880.91	836.84	810.27	867.93	860.24	836.57
31	897.71	933.71	880.09	846.81	805.41	865.16	861.00	842.90
32	888.89	896.22	879.04	861.46	808.92	862.75	862.60	835.12
33	906.79	933.79	887.51	869.40	808.72	867.87	866.66	853.78
34	915.19	909.36	890.94	880.72	809.76	863.04	866.25	842.86
35	911.05	932.88	887.78	884.01	808.30	863.58	859.64	836.60
36	909.36	924.09	888.82	889.31	809.51	860.38	862.17	832.99
37	925.19	938.40	891.22	887.26	809.64	860.74	857.04	838.48
38	912.87	929.14	895.29	874.17	808.91	870.02	855.36	833.96
39	925.55	932.70	894.07	900.23	808.99	859.75	868.01	837.06
40	931.66	943.23	897.69	905.37	810.88	858.33	855.99	837.84
41	891.99	940.29	896.06	908.38	812.59	865.93	857.01	833.20
42	916.78	942.27	905.00	907.93	820.80	869.49	868.79	841.71
43	936.50	942.44	900.80	915.52	820.93	857.73	869.48	833.85
44	929.10	949.04	904.77	909.97	818.05	867.01	872.08	841.00
45	940.46	946.09	905.75	913.90	814.35	863.97	862.90	837.33
46	924.11	949.30	907.39	910.14	821.28	855.09	862.95	838.43
47	925.06	943.80	899.31	924.60	818.58	863.67	865.14	841.62
48	944.52	947.77	908.20	923.98	835.54	875.92	866.79	836.28
49	952.68	943.17	904.15	926.65	828.66	865.83	870.76	849.41
50	952.33	948.92	919.06	929.32	829.60	874.98	868.41	837.29
51	947.42	946.58	922.54	934.13	839.63	865.12	874.95	842.74
52	949.83	948.55	918.58	929.92	834.44	874.27	874.09	839.65
53	956.35	960.28	921.35	936.87	831.20	869.72	873.54	840.19
54	952.76	936.42	927.20	929.61	829.92	865.35	879.13	844.50
55	958.30	957.68	923.24	935.98	832.14	883.40	882.48	845.51
56	959.59	961.77	937.69	942.90	839.52	878.32	885.31	848.75

Table B.9: Displays the peak reaction forces registered on the load cell for the Ingersoll Rand AVC27, for both the steel and tungsten runs.

Appendix C

NUMERICAL ANALYSIS

Figure C.1: Contains the five MATLAB scripts relevant to this thesis:

Dynamic System Response Model: Displays the code used to general the bode responses of the ideal and implementation models.

Modeling Equivalent Forearm Stiffness: Lists the input parameters for determining the stiffness of the radius bone, which is the larger of the two forearm bones (ulna & radius).

Experimental Results Processing: Includes a generic format to determine the peak values and associated time values for each DAQ sensor.

Percussive Index Plot Generator: Defines the percussive index calculation and returns a plot of the index with respect to exposure time.

Diagnostic Program Code: The code used to design the graphics user interface (GUI) for a diagnostic program. This code utilizes the same data processing/filtering approaches used to determine the experimental results in thesis. The code includes a browser feature to select the desired microphone data file, and a set of buttons and a scroll bar to set the run number and appropriate cutoff threshold to determine the peak points. Appendix C.2 displays the GUI and layout of the program.

Contents

Dynamic System Response Model

```
%% Parameters
Area = 0.003199994; %m
m = 2.9 + 2.64; %kg. mass of arm and rivet gun
rho = 1.225; %kg/m^3
g = 9.81; %m/s^2
Vol = 0.00028447943; % m^3
B = 101000; %N/m^2 (Pa)
Cap = Vol/B
tau = .150/2.3; %s, 0.150 = 2.3*tau
Res = tau/Cap

%% Ideal Model
dem = [m 0];
Ideal_TF = tf(1,dem)

%% Loaded Model
A = [0 Area/m; -Area/Cap -1/(Res*Cap)];
B = [1/m; 0];
C = [1 0];
sys = ss(A,B,C,0);
Loaded_TF = tf(sys)
% dem2 = [1 7.143 0.01326];
% m_TF = tf(1,dem2)

%% Bode Plots
optn = bodeoptions;
optn.FreqUnits = 'Hz';
optn.Title.FontSize = 18;
optn.YLabel.FontSize = 18;
optn.XLabel.FontSize = 18;
optn.TickLabel.FontSize = 12;
bode(Ideal_TF, Loaded_TF, optn)
h_legend=legend('T1(s)','T2(s)');
set(h_legend,'FontSize',14);
grid on
```

```
% [n,d] = ss2tf(A,B,C,0)
% mySys_tf = tf(n,d)

% h=gcf;
% set(h,'PaperOrientation','landscape');
% set(h,'PaperUnits','normalized');
% set(h,'PaperPosition', [0 0 1 1]);
% print(gcf, '-dpdf', 'Bode_Model.pdf');
```

Modeling Equivalent Forearm Stiffness

```
% Formula to determine stiffness and natural frequency model
% of a dynamic riveting carriage.

cArea_outer = (1157 + 163)/(1000^2);
r_outer = sqrt(cArea_outer/pi);
dsp =['Outer Bone Radius: ',num2str(r_outer),' m'];
disp(dsp)

r_inner = r_outer/1.24; %ratio literature (m)
cArea_inner = (r_inner^2)*pi;
dsp =['Inner Bone Radius: ',num2str(r_inner),' m'];
disp(dsp)

cArea_cortical = cArea_outer - cArea_inner;
dsp =['Cross-Sectional Area (Bone): ',num2str(cArea_cortical),' m^2'];
disp(dsp)

L = .2626; %mm men's radii bone length literature
dsp = ['Radius Length: ',num2str(L) ,' m'];
disp(dsp)
disp(' ')

E = 18.6*10^9; %N/m^2 modulus elasticity cortical bone literature
dsp =['E. Modulus (Cortical Bone): ',num2str(E),' N/m^2'];
disp(dsp)

k_bone = E*cArea_cortical/L; % N/m stiffness of one radii
k_N_m = k_bone;
dsp =['Spring Constant: ',num2str(k_bone),' N/m'];
disp(dsp)
disp(' ')

%%
mass = 2.9; %kg
dsp = ['Forearm Mass: ' , num2str(mass),' kg'];
disp(dsp)

wn = sqrt(k_N_m/mass);
dsp =['Radian Natural Frequency (w_n): ',num2str(wn),' rads/s'];
```

```matlab
disp(dsp)

fn = (1/(2*pi))*sqrt(k_N_m/mass);
dsp =['Natural Frequency (f): ',num2str(fn),' Hz'];
disp(dsp)

disp(' ')
%%

E_delrin_psi = 350000; %psi convert to Pa
E_delrin = E_delrin_psi/0.00014503773773; %N/m, from 350,000 psi
dsp = ['E. Modulus (Delrin): ',num2str(E_delrin),' N/m'];
disp(dsp)

Diameter_delrin = 1.25; %in, must convert to m

Area_Delrin = pi*(Diameter_delrin/2*0.0254)^2;
dsp = ['Cross-Sectional Area (Delrin): ',num2str(Area_Delrin),' m^2'];
disp(dsp)

Length_Delrin = E_delrin * Area_Delrin / k_bone;
dsp = ['Length Required (Delrin): ',num2str(Length_Delrin),' m'];
disp(dsp)

disp(' ')
disp('---(STANDARD UNITS Converted for Reference)')
dsp = ['---(Selected E. Modulus (Delrin): ',num2str(E_delrin_psi),' psi)'];
disp(dsp)
dsp = ['---(Selected Diameter (Delrin): ',num2str(Diameter_delrin),' in)'];
disp(dsp)
Length_in_Delrin = Length_Delrin * 39.3700787402; % m to in conversion
dsp = ['---(Length Required (Delrin): ',num2str(Length_in_Delrin),' in)'];
disp(dsp)
```

Experimental Results Processing

```matlab
load(['C:\Users\Jonathan Ahn\...\RivetData.mat']);
for n = 1:4
format long

%% PARAMETERS
y1 = Bucking_Laser_in(:,n); %Datum Laser for Interference Bolt Test
y2 = Rivet_Laser_in(:,n);
dt2 = 0.0002;
time2 = linspace(0,length(y2)*dt2,length(y2));

y3 = -Rivet_Load_Cell_lbf(:,n)*4.44822; %convert lbf to N
dt3 = 0.0001;
time3 = linspace(0,length(y3)*dt3,length(y3));

y4 = Microphone_pa(:,n);
dt4 = 0.00004;
time4 = linspace(0,length(y4)*dt4,length(y4));
```

```matlab
%% LASER DISPLACEMENT (mm)
figure(1);
y2 = smooth(y2);
y2 = -y2 + mean(y2(1:1000));
y2cut = min(y2(end-7000:end));

for m = 1:length(y2);
if y2(m) < 3*10^(-3);
    y2(m) = 0; %starting rest values normalized to zero
end
for m = 4800:length(y2);
if y2(m)> y2cut;
    y2(m) = y2cut; %values beyond cutoff are normalized to end distance
end
end
end
for m = 1:length(y2);
    if y2(m) >0
        start_time(1)=time2(m-1);
        break
    end
end

y2 = smooth(y2);
y2 = y2*.0254; %convert inches to mm
ax1=subplot(211)
[pks,locs] = findpeaks(y2,time2,'MinPeakDistance',.05);

%% PLOTTING PEAK VALUES
X = time2;
count = 1;
for m = [locs]
    index = find(X==m);
    X_point(count) = X(index);
    count = count+1;
end
count = 1;
for m = [X_point]
    index = find(time2==m);
    Lpks(count) = y2(index);
    count = count +1;
end

for c = 1:length(Lpks)
    Data(c,1) = Lpks(c);
    Data(c,3) = X_point(c);
end
h1=plot(time2,y2,'r')
grid on, hold on
plot(X_point,Lpks,'rv')
title('Interference Fit Bolt Results')
ylabel('Displacement (m)')

LD_diff = diff(Lpks);
for c = 1:length(LD_diff)
```

```matlab
    Data(c+1,2) = LD_diff(c);
    Data(1,2) = Data(1,1);
end

Data(c+3,1) = Lpks(end)-y2(1); %Total Displacement
Data(c+3,3) = X_point(end)-start_time; %Duration

%% LOAD CELL (N)
[LHi,LLo]=envelope(y3,1,'peak');
my3 = mean(y3(1:1000));
for m = 1:length(y3);
    if time3(m)<start_time;
        y3(m) = my3;
        LHi(m) = my3;
    end

    if time3(m)>locs(end);
        y3(m) = mean(y3(end-1000:end));
        LHi(m) = mean(y3(end-1000:end));
    end
end

ax2=subplot(212);
ys3 = y3.^4; %Scaled values to distinguish time position of peaks
mys3 = my3.^4;
hold on, grid on
[pks2,locs2]=findpeaks(ys3,time3,'MinPeakDistance',.04,'MinPeakHeight',(3*mys
3/2));
X = time3;
Y = y3;
count = 1;
for m = [locs2]
    index = find(X==m);
    X_point(count) = X(index);
    count = count+1;
end
count = 1;
for m = [X_point] %Applied to non-scaled Load Cell data
    index = find(time3==m);
    Lpks(count) = y3(index);
    count = count +1;
end
for c = 1:length(Lpks)
    Data(c,4) = Lpks(c);
    Data(c,5) = X_point(c);
end

Data(c+2,5) = 1/(mean(diff(locs2))); %Driving Frequency
h1=plot(time3,[y3],'r')
grid on, hold on
plot(X_point,Lpks,'rv')
ylabel('Force (N)')
xlabel('Time (s)')
legend('Ingersoll Rand AVC27','---Peak','Atlas Copco 12P','---Peak')

%% MICROPHONE (Pa)
```

```matlab
x = time4;
x = x';
y = Microphone_pa(:,n);
y = y.^1;

Mic0 = Microphone_pa(:,n);
Mic2 = Microphone_pa(:,n);
Mmax = max(y);
Msort = sort(y,'descend');
Mlength = length(y);
thr = .1;
Mtop = Msort(1:Mlength*thr);
Mcutoff = mean(Mtop);
Mic0(Mic0<Mcutoff) = 0;
index4 = find(time4>X_point(end));
y1 = Mic0;
y1(index4:end) = 0;
x = time4;

[pks,locs] = findpeaks(y1,x,'MinPeakDistance',.035);
X = time4;
Y = y4;
count = 1;
for m = [locs]
    index = find(X==m);
    X_point(count) = X(index);
    count = count+1;
end
count = 1;
for m = [X_point]
    index = find(time4==m);
    Lpks(count) = y4(index);
    count = count +1;
end
for c = 1:length(Lpks)
    Data(c,6) = Lpks(c);
    Data(c,7) = X_point(c);
end

Data(c+2,7) = 1/(mean(diff(locs))); %interval
plot(x,y,'r')
grid on, hold on
plot(X_point,Lpks,'rv')
ylabel('Acoustic Pressure (Pa)')
xlabel('Time (seconds)')
end

%% STATIC PRESSURE (Pa)
y7 = Static_Pressure_psi(:,n);
dt7 = 0.0001
time7 = linspace(0,length(y7)*dt7,length(y7));

y8 = Diff_Pressure_psi(:,n);
dt8 = 0.0001
time8 = linspace(0,length(y8)*dt8,length(y8));
```

```
y9 = Temperature_f(:,n);
dt9 = 0.2
time9 = linspace(0,length(y9)*dt9,length(y9));

m = mean(y9(1:5))
figure(1);
findpeaks(y7,time7,'MinPeakDistance',.035);
[pks1,locs1] = findpeaks(y7,time7,'MinPeakDistance',.035);
locs1 = locs1';

figure (2);
findpeaks(-y7,time7,'MinPeakDistance',.035);
[pks2,locs2] = findpeaks(-y7,time7,'MinPeakDistance',.035);
locs2 = locs2';

a1=subplot(311)
plot(time7,y7)
a2=subplot(312)
plot(time8,y8)
a3=subplot(313)
plot(time2,-y2)
linkaxes([a1 a2 a3],'x')
```

Percussive Index Plot Generator

```
load(['C:\Users\Jonathan Ahn\...\RivetData.mat']);
for n = 1:4

tf = ##;
t1 = ##;
threshold = ##;

for tau = [.0025]
t2 = t1+tau;
count = 1;

for k = 0:0.0001:(tf-t1)
ta1= t1+k;
ta2 = t2+k;

dt = 0.0001;
m1 = (ta1/dt);
m2 = (ta2/dt);

y3 = -Rivet_Load_Cell_lbf(m1:m2,n)*4.44822; %convert lbf to N
y3 = (y3/(2.85+2.9)); % Force/mass_gun

time3 = linspace(0,length(y3)*dt,length(y3));
Q = trapz(time3,y3);
Qa = (Q/tau)^2.5;
HIC(count) = Qa*tau;
```

```
count= count +1;
x = 1:1:count-1;
end

x = linspace(0,length(HIC)*dt,length(HIC));
ax1=subplot(211)
plot(x,HIC,'linewidth',1.2)
hold on
end

HIC = real(HIC)
findpeaks(HIC,x,'MinPeakDistance',.05,'MinPeakHeight',threshold);
[pks,locs]=findpeaks(HIC,x,'MinPeakDistance',.05,'MinPeakHeight',threshold);
ANSWER(:,2)= pks';
ANSWER(:,1)=locs;
```

Diagnostic Program Code

```
%%Code revised on 6/26/16 JA
%Includes browse feature to locate parent folder

function varargout = FAUB_Mic(varargin)
gui_Singleton = 1;
gui_State = struct('gui_Name',        mfilename, ...
                   'gui_Singleton',  gui_Singleton, ...
                   'gui_OpeningFcn', @FAUB_Mic_OpeningFcn, ...
                   'gui_OutputFcn',  @FAUB_Mic_OutputFcn, ...
                   'gui_LayoutFcn',  [] , ...
                   'gui_Callback',   []);
if nargin && ischar(varargin{1})
    gui_State.gui_Callback = str2func(varargin{1});
end
if nargout
    [varargout{1:nargout}] = gui_mainfcn(gui_State, varargin{:});
else
    gui_mainfcn(gui_State, varargin{:});
end
function FAUB_Mic_OpeningFcn(hObject, eventdata, handles, varargin)
handles.output = hObject;
% Update handles structure
guidata(hObject, handles);
if strcmp(get(hObject,'Visible'),'off')
    plot(rand(1));
end
function varargout = FAUB_Mic_OutputFcn(hObject, eventdata, handles)
varargout{1} = handles.output;
function pushbutton3_Callback(hObject, eventdata, handles)
function pushbutton1_Callback(hObject, eventdata, handles)
%axes(handles.axes1);
cla;
% popup_sel_index = get(handles.popupmenu1, 'Value');
% StrVal = get(handles.text18,'String');
% load([StrVal]);
```

```matlab
% Microphone_pa = Microphone_pa';    %code for transposing labview if needed
        Run = get(handles.edit2,'String');
        %Hole = get(handles.edit3,'String');
        SetRun = get(handles.text53,'String');
        SenSel = get(handles.popupmenu2,'String');

        %load(['C:\Users\Jonathan\Documents\BARC\',num2str(Run),'\Hole
',num2str(Hole),'.mat']); %select directory pathway
        %load([SetRun,'\',num2str(Run),'\Hole ',num2str(Hole),'.mat']);
        load(['C:\Users\Jonathan
Ahn\Desktop\Riveting\Thrubolt_AVC27_AC12P\RivetData801.mat']);
guidata(hObject,handles);
rows = size(Microphone_pa,2)
n = 1;
        time = dt_Microphone_pa(:,n)*(length(Microphone_pa(:,n))-1);
        x = 0:dt_Microphone_pa(:,n):time;
        %x = x';
        y = Microphone_pa(:,n);

        Mic0 = Microphone_pa(:,n);
        Mic2 = Microphone_pa(:,n);
        plot(x,y)
        hold on
        Mmax = max(y);
        Msort = sort(y,'descend');
        Mlength = length(y);

        %Percent = get(handles.edit2,'String');
        threshold = get(handles.text54,'String');
        thr = str2double(threshold);
        Mtop = Msort(1:(Mlength*thr),1); %top 3% of data input
        Mcutoff = mean(Mtop);
        Mic0(Mic0<Mcutoff) = 0;
        y1 = Mic0;
        findpeaks(y1,x,'MinPeakDistance',.025);
        [pks,locs] = findpeaks(y1,x,'MinPeakDistance',.025);
        count = length(pks);
        duration = (max(locs)-min(locs));
        interval = 1/(mean(diff(locs)));
        set(handles.text1, 'String',[num2str(count)]);
        set(handles.text2, 'String',[num2str(duration)]);
        set(handles.text3, 'String',[num2str(interval)]);
        y2 = abs(y);
        Mmax = max(y2);
        Msort = sort(y2,'descend');
        Mlength = length(y2);

        %Percent = get(handles.edit2,'String');
        Mtop = Msort(1:(Mlength*thr),1); %top 3% of data input
        Mcutoff = mean(Mtop);
            Mic2(Mic2<Mcutoff) = 0;
        y3 = Mic2;
        [pks2,locs] = findpeaks(y3,x,'MinPeakDistance',.025);

        Mmin1 = floor(min(pks));
        Mmin2 = floor(min(pks2));
```

```matlab
        if Mmin1 > Mmin2;
            Mmin = Mmin2;
        else Mmin = Mmin1;
        end

        Mmax = ceil(max(y2));
        Mmean = floor(mean(pks2));

        set(handles.text32, 'String',[num2str(Mmax)]);
        set(handles.text34, 'String',[num2str(Mmean)]);
        set(handles.text33, 'String',[num2str(Mmin)]);

% -----------------------------------------------------------------
function FileMenu_Callback(hObject, eventdata, handles)
function OpenMenuItem_Callback(hObject, eventdata, handles)
file = uigetfile('*.fig');
if ~isequal(file, 0)
    open(file);
end

function PrintMenuItem_Callback(hObject, eventdata, handles)
printdlg(handles.figure1)
function CloseMenuItem_Callback(hObject, eventdata, handles)
selection = questdlg(['Close ' get(handles.figure1,'Name') '?'],...
                     ['Close ' get(handles.figure1,'Name') '...'],...
                     'Yes','No','Yes');
    if strcmp(selection,'No')
        return
    end

delete(handles.figure1)

function popupmenu1_Callback(hObject, eventdata, handles)
function popupmenu1_CreateFcn(hObject, eventdata, handles)
if ispc && isequal(get(hObject,'BackgroundColor'),
get(0,'defaultUicontrolBackgroundColor'))
    set(hObject,'BackgroundColor','white');
end
global rows;

for i = 1:rows;
set(hObject, 'String', {'Rivet Signal' i});
end

function pushbutton2_Callback(hObject, eventdata, handles)

grid on
function checkbox3_Callback(hObject, eventdata, handles)
a = get(hObject,'Value');
if a == 1;
    grid on
else
    grid off
end
```

```
function slider1_CreateFcn(hObject, eventdata, handles)
if isequal(get(hObject,'BackgroundColor'),
get(0,'defaultUicontrolBackgroundColor'))
    set(hObject,'BackgroundColor',[.9 .9 .9]);
end

function text1_CreateFcn(hObject, eventdata, handles)
function axes1_CreateFcn(hObject, eventdata, handles)
[x,map]=imread('C:\Users\Jonathan\Documents\MATLAB\myfunctions\Barclogo.jpeg'
);
xs = 70;
ys = 270;
I2=imresize(x, [xs ys]);
h=uicontrol('style','pushbutton',...
            'units','pixels',...
            'position',[150 680 ys+10 xs+10],...
            'cdata',I2)

[x,map]=imread('C:\Users\Jonathan\Documents\MATLAB\myfunctions\UWlogo.jpg');
xs = 50;
ys = 300;
I2=imresize(x, [xs ys]);
h=uicontrol('style','pushbutton',...
            'units','pixels',...
            'position',[990 690 ys+10 xs+10],...
            'cdata',I2)

function text27_CreateFcn(hObject, eventdata, handles)
function text32_CreateFcn(hObject, eventdata, handles)
function text34_CreateFcn(hObject, eventdata, handles)
function text33_CreateFcn(hObject, eventdata, handles)

function edit1_Callback(hObject, eventdata, handles)

function edit2_Callback(hObject, eventdata, handles)
function edit2_CreateFcn(hObject, eventdata, handles)
if ispc && isequal(get(hObject,'BackgroundColor'),
get(0,'defaultUicontrolBackgroundColor'))
    set(hObject,'BackgroundColor','white');
end

function edit3_Callback(hObject, eventdata, handles)
function edit3_CreateFcn(hObject, eventdata, handles)
if ispc && isequal(get(hObject,'BackgroundColor'),
get(0,'defaultUicontrolBackgroundColor'))
    set(hObject,'BackgroundColor','white');
end

function edit4_Callback(hObject, eventdata, handles)
function edit4_CreateFcn(hObject, eventdata, handles)
if ispc && isequal(get(hObject,'BackgroundColor'),
get(0,'defaultUicontrolBackgroundColor'))
    set(hObject,'BackgroundColor','white');
end
```

```matlab
function slider2_Callback(hObject, eventdata, handles)

function slider2_CreateFcn(hObject, eventdata, handles)

if isequal(get(hObject,'BackgroundColor'),
get(0,'defaultUicontrolBackgroundColor'))
    set(hObject,'BackgroundColor',[.9 .9 .9]);
end

function pushbutton5_Callback(hObject, eventdata, handles)
[file path] = uiputfile('*.png');
print([path file], '-dpng');

function pushbutton6_Callback(hObject, eventdata, handles)
foldername = uigetdir;
fullpathname = strcat(foldername);
set(handles.text53, 'String', fullpathname)
SetRun = get(handles.text53,'String');

function text53_CreateFcn(hObject, eventdata, handles)

function slider3_Callback(hObject, eventdata, handles)
slider_value = get(hObject,'Value');
set(handles.text54, 'String', slider_value);
function slider3_CreateFcn(hObject, eventdata, handles)
if isequal(get(hObject,'BackgroundColor'),
get(0,'defaultUicontrolBackgroundColor'))
    set(hObject,'BackgroundColor',[.9 .9 .9]);
end

function text54_CreateFcn(hObject, eventdata, handles)
function popupmenu2_Callback(hObject, eventdata, handles)
function popupmenu2_CreateFcn(hObject, eventdata, handles)
if ispc && isequal(get(hObject,'BackgroundColor'),
get(0,'defaultUicontrolBackgroundColor'))
    set(hObject,'BackgroundColor','white');
end
function text61_CreateFcn(hObject, eventdata, handles)
```
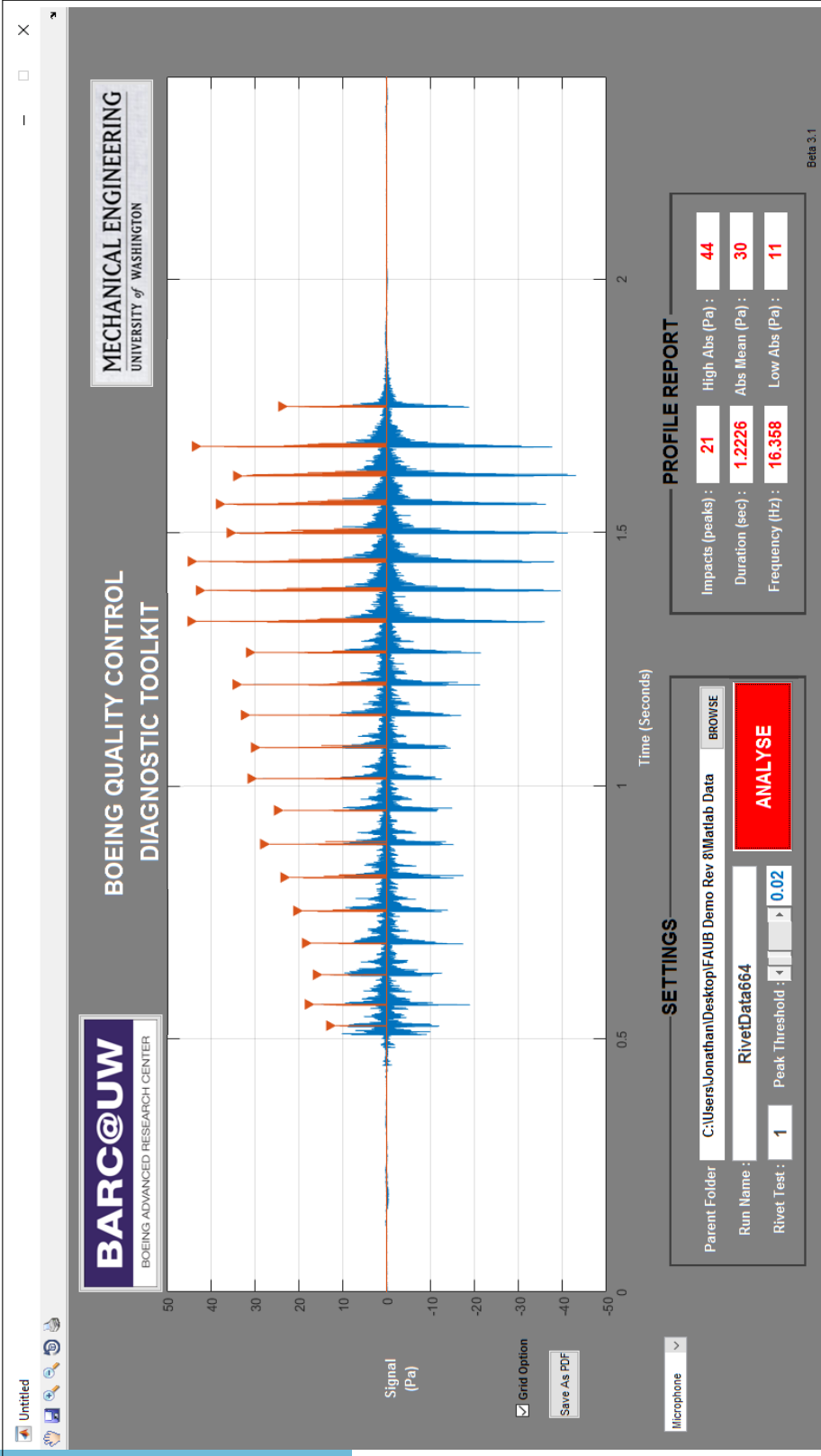
Figure C.2: Examples the user interface of the Diagnostic Program. This script was designed to process sound pressure data in an aircraft factory, and proposed as part of a portable diagnostic toolkit for Quality Control. The blue signal represents the raw data collected from overhearing percussive riveting. The red signal is the filtered data returned to the operator with the following information: total number of strikes, exposure duration, and sound level pressures.

VITA

Jonathan Young Ahn is a graduate research assistant for the Boeing Advanced Research Center (BARC) at the University of Washington. This work has been in partial fulfillment of a Master's of Science in Engineering (MSE), after which he plans to enter the aerospace industry.

Jonathan was born in Boston, Massachusetts, and previously graduated from the Worcester Polytechnic Institute where he completed a Bachelors of Science in Biomedical Engineering, specializing in biomechanics and system optimization.

He welcomes your comments to `jyahn326@uw.edu/gmail.com`.